UNIVERSITY OF CALIFORNIA,
IRVINE

Tripodal Phosphoryl Amide Frameworks: Investigating The Relationship Between High Valent Metal–Oxido And Metal–Hydroxido Complexes.

DISSERTATION

submitted in partial satisfaction of the requirements
for the degree of

DOCTOR OF PHILOSOPHY

in Chemistry

by

Victoria F. Oswald

Dissertation Committee:
Professor Andrew S. Borovik, Chair
Professor Alan F. Heyduk
Professor Michael T. Green

2018

DEDICATION

to my mom
for teaching me what true strength is; the meaning of honesty, integrity, and never giving up.

to my dad
for teaching me the importance of hard work and discipline.

to my advisor
for teaching me that context is everything.

Getting this far, crazy.
Stopping now, crazier.

//Serena Williams

TABLE OF CONTENTS

LIST OF FIGURES

Page

LIST OF TABLES

Page

LIST OF SCHEMES

Page

LIST OF EQUATIONS

Page

ACKNOWLEDGMENTS

Andy, where to begin? At a very early point in my graduate career, you gave me a tremendous amount of freedom, absolutely more than I deserved, and believed in my ideas. You have challenged me in ways I never expected, and you have always known how to push me when I needed it most. The reason this lab has been such an amazing place to grow as a scientist is because of the environment you've cultivated. Above all else, I want to thank you for always be willing to listen to me. I sometimes have far more opinions than I should. Okay, *maybe more than sometimes*, but never the less your door was always open to me. I have cherished our conversations both scientific and otherwise. You have been much more than a research advisor to me, and I appreciate our relationship far more than you know.

I would also like to thank my committee members: Professors Alan Heyduk and Michael Green for serving on my committee and their time. Alan, I have always appreciated our conversations. You have helped me set a standard for the type of critical thinker I wanted to be and for that I am forever grateful. MT, as elusive as you can sometimes be, whenever I did get my hands on you our conversations always taught me something new. I have enjoyed getting to know you over these few years.

I was taught that a metal ion does not exist in isolation (at least not on Earth, *maybe on Uranus*), but I have learned that neither does a graduate student. In that vein, I am forever indebted to those who came before me. Sarah, your work ethic and commitment to scientific integrity have always given me something to aspire to. Ethan, thank you for taking me under your wing, or perhaps it is more appropriate to say letting me force myself there. You were the one that really taught me the ins and outs of the lab and instilled in me to always think critically about my science. Jon and Sam thanks for always letting me be one of the "bros," even though I never was able to appropriately extend my middle-finger in greetings of brotherhood. You both made the office such an enjoyable place to spend the sometimes seemingly endless days and nights. Jason thank you for never being shy to be the first to try any new culinary creation I brought in. Knowing I could forever expect you and Sam to have some dramatic reaction over the last hand-pie always made me laugh. And I cannot forget Nate (AAA), who was always willing to spend an extraneous amount of time answering questions, especially if that question was "what color is the green leaf?" How much I enjoyed the time I spent with you all is immeasurable.

Although I did not overlap with Dr. Nathaniel Sickerman or Dr. David Lacy, I would be remise if I did not thank them. I still do not know exactly how the spark was ignited to enter the realms of phosphoryl amide base ligands, but I am so grateful it was. Without their initial development of H_3poat, none of the following work would have been conceivable.

The group has changed a great deal from when I first started, but to those you have come after me: Noam, Maisha, Justin (TMEDA), Lisa, Kelsey, Justin (j), Sunny, Dolores, Deb, Jared, Meghen, Ankita, and Francisco, it comes down to the people that make the Borovik lab such a tremendous place to be, and I have appreciated getting to know all of you. A *very unique*

shout out must go to TMEDA for always letting me give him a hard time. I know it must have been rough realizing you don't actually live in New York City. As the younger of you continue to pursue your goals over these next several years, remember no matter how many people come in and out of those green doors, one thing will never change: that the quality of your degree is a direct reflection of what *you* put into it. Don't get swept in what anyone else is or isn't doing. Remember, this is a marathon not a sprint, but above all else don't settle for mediocrity.

I would like to give a special thank you to two current Borovik members: Kelsey and j. First, to my cubby-mate: the infamous Kelsey Rose Miller. Are there really words? *Really?* Perhaps a lap around the peanut-table or a victory lunge would more accurately represent how much you mean to me. I will never forget the very late nights and even earlier mornings we would put in for the sake of "precious" or how to order your milk-tea. Thank you for always supporting me (*even sometimes against better judgment*) and being my number one hype-woman. Then there is j. Thank you for constantly pushing me to stay on top of the literature and always labelling your energy axes. Our 5 am helium runs are some of my favorite memories. As I leave, I know the EPR spectrometer is in good hands, and I cannot wait to see what more you will accomplish with the 2.0 version of her.

Beyond the Borovik Lab, I have to mention two fellow UCI chemists: Claudia and Alec. Claudia, we have gone through every major milestone of this rollercoaster ride together. I am so grateful for your friendship, even if we don't spend nearly as much time together as we use to; I value it more than you know. Alec, thank you for always picking up my phone calls. You are the only person that I can say 100% of the time if I "spoke" with you to Andy that it was actually on the phone not via a text message. I do not take for granted how much time you have committed to helping me with my chemistry. Name a better friendship building exercise than spending a straight 24 hours in the dark depths of the Raman room… I'll wait.

In addition to all of these great UCI chemists, I must thank our collaborators from the Hendrich Lab at Carnegie Melon University. Andrew has been an invaluable resource for me. His patience and willingness to teach me about the spectroscopic techniques used to analyze our compounds has been critical in my chemistry's progression. It was truly a great experience working with him.

Outside of the lab, I was fortunate to make some great friends. Thank you to the Be More Athletics community and my ladies of Cristophe Salon. The home I found in you all, I will cherish forever.

Of course, I am endlessly grateful for the love and support of my family. I am so lucky to have siblings that even from 3000 miles away always make me feel like I am with them. I have two lifelong friends who are so much more like family. Katie and Doreen, thank you for riding every wave of life with me. I am very fortunate to have parents that gave me everything they could to aid in my success. Mom, who I am today is a testament to your endless strength and encouragement. Dad, you are the first person I call whether the news

is good or bad. You always have a way of refocusing me and keeping my head on straight. I hope you both know how important you are to me.

Faben, having this experience bring us together means something to me that words could never understand. So much of my growth and success I attribute to you. Thank you for being my constant source of strength and motivation throughout this journey. I cannot wait to see what our next chapter holds.

*Finally, I must thank the **chelate effect**, without which, none of this chemistry would be possible.*

CURRICULUM VITAE

EDUCATION

Ph.D., Chemistry, December 2018
University of California, Irvine
Research Advisor: Andrew S. Borovik

B.A., ACS Chemistry, May 2013
Barnard College of Columbia University, Manhattan, NY

PUBLICATIONS

P. M. Cheung, K.T. Burns, Y. M. Kwon, M. Y. Deshaye, K. J. Aguayo, **V. F. Oswald,** T. Seda, L. N. Zakharov, T. Kowalczyk, and J. D. Gilbertson. "Hemilabile Proton Relays and Redox-Activity Lead to $\{FeNO\}^x$ and Significant Rate Enhancements in NO_2 Reduction. *J. Am. Chem. Soc.* **2018**, Article ASAP.

A. Weitz, E. A. Hill, **V. F. Oswald**, E. L. Bominaar, A. S. Borovik, M. P. Hendrich, and Y. Guo. "Probing hydrogen bonding interactions to iron-oxido/hydroxido units via 57Fe nuclear resonance vibrational spectroscopy," *Angewandte Chemie*, **2018**, *57*, 16010.

V. F. Oswald, A. C. Weitz, S. Biswas. J. W. Ziller, M. P. Hendrich, and A. S. Borovik. Manganese−Hydroxido Complexes Supported by a Urea/Phosphinic Amide Tripodal Ligand. **2018**, *20*, 54.

M. Keener, M. Peterson, R. H. Sánchez, **V. F. Oswald**, G. Wu, and G. Ménard. "Towards Catalytic Ammonia Oxidation to Dinitrogen: A Synthetic Cycle Using a Simple Manganese Complex," Chem. Eur. J., **2017**, *23*, 1.

C. P. Owens, F. E. H. Katz, C. H. Carter, **V. F. Oswald**, F. A. Tezcan. "Tyrosine-Coordinated P-Cluster in G. diazotrophicus Nitrogenase: Evidence for the Importance of O-Based Ligands in Conformationally Gated Electron Transfer," *J. Am. Chem. Soc.* **2016**, 138, 10124.

Q. Shi, S. Zhang, J. Zhang, **V. F. Oswald**, A. Amassian, S. R. Marder, S. B. Blakey. "KOtBu-Initiated Aryl C-H Iodination: A Powerful Tool for the Synthesis of High Electron Affinity Compounds," *J. Am. Chem. Soc.* **2016**, 138, 3946.

V. F. Oswald, W. Chen, P Harvilla, J. S. Magyar. "Overexpression, purification, and enthalpy of unfolding of ferricytochrome *c*552 from a psychrophilic microorganism," *J. Inorg. Biochem.* **2014**, *131*, 76.

PRESENTATIONS

V. F. Oswald, A. C. Weitz, M. P. Hendrich, M. T. Green, A. S. Borovik. A Non-heme Fe(IV)-oxido Complex and Lewis Acids. Abstracts of Papers, 25th ACS National Meeting & Exposition, New Orleans, LA, United States, March 18-22, 2018. Talk.

V. F. Oswald, A. C. Weitz, M. P. Hendrich, M. T. Green, A. S. Borovik. Incorporation of Phosphoryl Amide Moieties to Support High Valent Metal Oxido/Hydroxido Complexes. SoCal Bioinorganic Conference, Irvine, CA, December 7th, 2018.

V. F. Oswald, A. C. Weitz, K. Mittra, M. P. Hendrich, M. T. Green, A. S. Borovik. Incorporation of Phosphoryl Amide Moieties to Support High Valent Metal Oxido/Hydroxido Complexes. UCI Student Inorganic Seminar Series, Irvine, CA, October 26, 2017.

C, M. Kotyk, J. E. Henebry, C. Sun, J. L. Steele, Y. Chen, **V. F. Oswald,** J. W. Bacon, A. L. Rheingold, L. Doerrer, Linda. Abstracts of Papers, 253rd ACS National Meeting & Exposition, San Francisco, CA, United States, April 2-6, 2017. Poster.

V. F. Oswald, A. S. Borovik. Bioinorganic Gordon Research Seminar. "Ligand Design to Support High Valent Metal Oxido/Hydroxido Complexes." Ventura, CA, January 26-29, 2017. Talk.

V. F. Oswald, A. S. Borovik. Ligand Development to Support Monomeric High Valent Metal Hydroxide Complexes. 4th Penn State Bioinorganic Workshop, State College, PA, June 1-11, 2016. Talk and Poster.

V. F. Oswald, A. S. Borovik. Bioinspired heterometallic systems for the activation of small molecules. Abstracts of Papers, 251st ACS National Meeting & Exposition, San Diego, CA, United States, March 13-17, 2016. Poster.

V. F. Oswald, W. Chen, P. B. Harvilla, O. Sokolovskaya, J. S. Magyar. Energetics of cytochrome c from a psychrophilic hydrocarbonoclastic microbe. Abstracts of Papers, 245th ACS National Meeting & Exposition, New Orleans, LA, United States, April 7-11, 2013. Poster.

ABSTRACT OF THE DISSERTATION

Tripodal Phosphoryl Amide Frameworks: Investigating The Relationship Between High Valent Metal–Oxido And Metal–Hydroxido Complexes.

By

Victoria F. Oswald

Doctor of Philosophy in Chemistry

University of California, Irvine, 2018

Professor Andrew S. Borovik, Chair

Metal ion cofactors within active sites are essential components for many proteins and have been directly linked to function. Active sites contain either a single or multiple metal ion(s) participating in a mixture of covalent and non-covalent interactions that function cooperatively to perform efficient and selective chemical transformations. Non-covalent interactions are often found within the volume of space that surrounds the metallocofactors, denoted as the microenvironment, which influence key properties such as the transfer of protons and electrons. Non-covalent interactions are the major forces that influence the microenvironments within protein active sites with hydrogen bonds (H-bonds) being the most dominant. Using these architectural features as inspiration, the works of this dissertation describes the design, preparation, and characterization of Mn/Fe– oxido and hydroxido complexes supported by frameworks that incorporate phosphoryl amide moieties.

Chapter 2 introduces the development of new ligand frameworks containing phosphorus. The design premise behind the usage of phosphoryl amides was that the deprotonated phosphoryl amide nitrogen atom would produce a ligand field that stabilizes high valent complexes, and that the P=O units would serve as an H-bond acceptor, an

auxiliary metal binding site, and produce a negative polarized cavity to help stabilize high valent metal–hydroxido/oxido complexes.

Chapters 3 and 4 describe the development of Mn/Fe–OH complexes of the hybrid ligand $[H_2pout]^{3-}$ that installs a combination of two H-bond donors and one H-bond acceptor within the secondary coordination sphere. The $[H_2pout]^{3-}$ ligand was used to prepare the M^{II}–OH complexes, which had sufficiently low redox potentials to synthetically prepare its corresponding M^{n}–O(H) (n = III, IV) analogs.

In Chapter 5 of this dissertation a new high spin, Fe^{IV}–oxido complex supported by a symmetrical phosphinic amide tripod is discussed along with its reactivity with Lewis acids. A series of LA (LA = Mg^{2+}, Ca^{2+}, Sr^{2+}, Ba^{2+}, and H^{+}) were added to the Fe^{IV}–oxido complex and generated distinct Fe^{IV} species. The vibrational data shows a clear change in the Fe–O vibrations when Mg^{2+} or Ca^{2+} ions are added, corroborating that these ions affect the Fe^{IV}–oxido unit. Preliminary data with H^{+} suggests that protons interact with the Fe^{IV}–oxido complex, but not at the Fe^{IV}–oxido unit, suggesting that an Fe^{IV}–OH species is not produced.

Chapter 6 takes a different approach to generating an Fe^{IV}–OH species. The beginning of this chapter discussed the preparation and characterization of low valent Fe–aqua/hydroxide complexes within $[poat]^{3-}$ scaffold. The $Fe^{II/III}$–OH complexes have similar properties as previously developed frameworks; however, once oxidized beyond Fe^{III}–OH, the reactivity is different. The one-electron oxidized complex exhibits magnetic properties that are unprecedented to anything we have seen before and has been assigned as an S = 2 system containing a high spin Fe^{III} center antiferromagnetically coupled to a ligand radical.

CHAPTER 1

Introduction

For nearly half a century, understanding the structural factors necessary for enzymatic reactivity has captivated the research of metallobiochemistry.[1–3] From these studies what is certain is the crucial role that both the primary coordination environment (ligands covalently bound to the metal ion) and the local environment (the secondary coordination sphere made up of noncovalent interactions) about the metal center(s) play in determining the properties and functionalities of metallocofactors. The ligands that are bound directly to the metal center are important in defining properties such as the electronic structure of the metal ion, which is influential in stability and reactivity. It's been found that covalent interactions alone are not sufficient to promote catalytic reactivity.[4–7] Removal of a metallocofactor from its protein host has been shown to often greatly impede, if not halt, all activity.[8,9] The processes of making and breaking O–O bonds highlight the necessities of both coordination spheres: 1) their primary coordination spheres allow access to high valent metal–oxido/hydroxido intermediates and 2) a variety of noncovalent interactions within the secondary coordination sphere are suggested to be essential for the movement of protons and electrons in both reactions.[10–13]

One of the most well studied systems that participate in the activation of dioxygen are cytochrome P450s (P450s), which can hydroxylate hydrocarbons with exceptional selectivity.[14] The active sites of P450s are composed of a single heme center and a H-bonding network surrounding the dioxygen binding site. A common mechanistic proposal invokes an Fe^{IV}–oxido and an Fe^{IV}–hydroxido species in order to perform the oxidative transformation.[15,16] Work by Green and coworkers showed that the competent oxidant

responsible for cleavage of unactivated C–H bonds is an Fe^{IV}–oxido species with a radical delocalized through the porphyrin and thiolate–ligands (Scheme 1.1A, Compound I).[17] Activation of the C–H bond is followed by hydroxylation of the carbon radical during rebound, which is hypothesized to be performed by an Fe^{IV}–hydroxido species (Scheme 1.1A, Compound II).[18] High valent metal-oxidos are also pivotal for reactivity in non-heme systems. For example, taurine α-ketoglutarate dioxygenase (TauD), whose active site is made up of a single Fe metal bound to three amino acid residues of the protein manifold and an α-ketoglutarate cofactor is responsible for the hydroxylation of an unactivated C–H bond of taurine. Work by Bollinger and Krebs identified that the reaction pathway of TauD starts with dioxygen attack of the Fe^{II} metal ion to generate an Fe^{IV}–oxido species, which is responsible for initiating the oxidative chemistry of the substrate (Scheme 1.1B).[19]

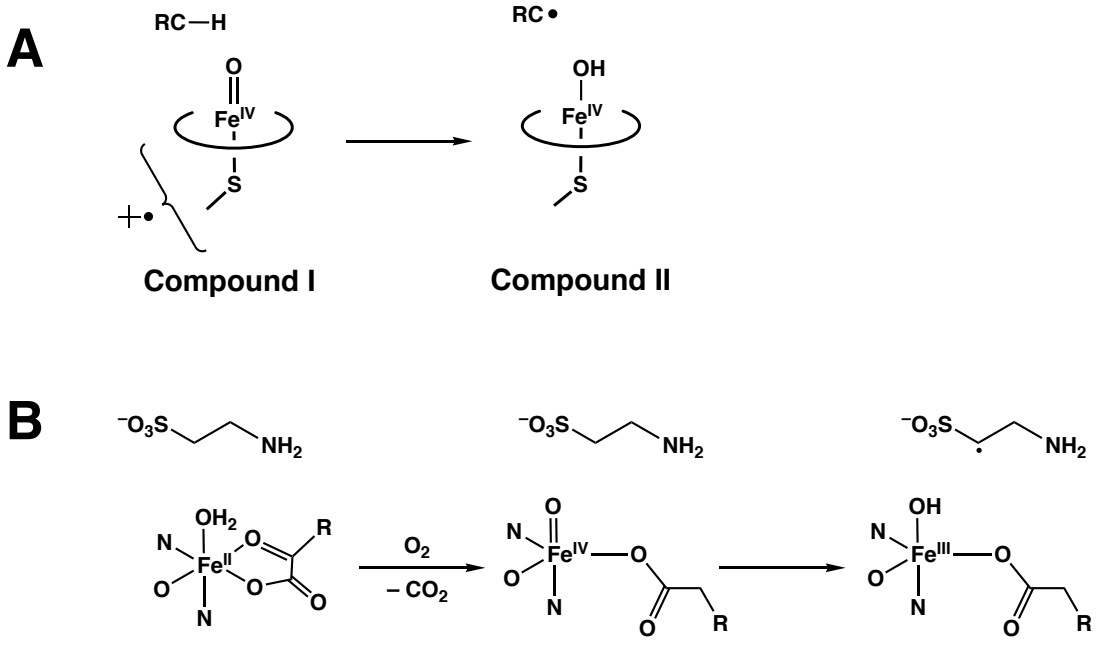

Scheme 1.1 The proposed mechanism for C–H bond cleavage by Compound 1 in P450s to generate Compound II and a carbon-based radical on the substrate (**A**). Partial mechanism for TauD highlighting the ferryl intermediate (**B**).

Metal-oxido/hydroxido moieties are also suggested to be instrumental in the formation of O–O bonds as illustrated in the oxygen-evolving complex (OEC) of photosystem II (PSII). The OEC contains a Mn_4CaO_5 cluster that is surrounded by an intricate arrangement of H-bonds, involving amino acid residues and structural water molecules that provide a pathway for proton and electron transfer (Figure 1.1).[20] In

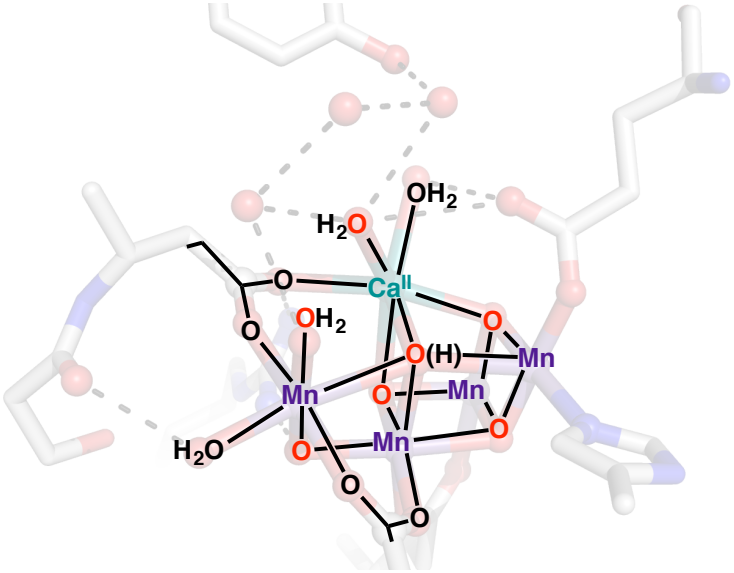

Figure 1.1 The active site in the OEC, illustrating the heterometallic (Mn_4CaO_5) cluster and H-bonding network (highlighted with black dashed lines). PDB: 3WU2

addition to the H-bonding network surrounding the OEC, a second unique aspect of the active site is the incorporation of both redox active (Mn) and redox inactive (Ca) metal ions that work cooperatively to oxidize water. While the exact role of the Ca^{2+} ion in the OEC is still not entirely understood, its incorporation within the cluster is known to be essential for function, where only a Sr^{2+} ion can replace the Ca^{2+} ion and maintain activity, albeit with lower efficiency.[21–25] Two mechanisms that involve the 2+ ion for water oxidation have been proposed: 1) nucleophilic attack by a Ca^{2+}–OH (or $–OH_2$) unit on either an electrophilic terminal Mn^{V}–oxido center or a bridging oxido ligand within the cluster[26–30];

thereby implicating a direct role for the Ca^{2+} ion in O–O bond formation (Figure 1.2A), and 2) coupling between an oxyl radical and another oxido ligand within the cluster[31–34] (Figure 1.2B). In the first mechanism, the 2+ ion is suggested to play a direct role in O–O bond formation by providing the substrate water molecule; whereas, in the latter case the 2+ ion is believed to play a role in attenuating the redox chemistry of the cluster. Both mechanisms support the premise that a redox–inactive metal ion is necessary for function.

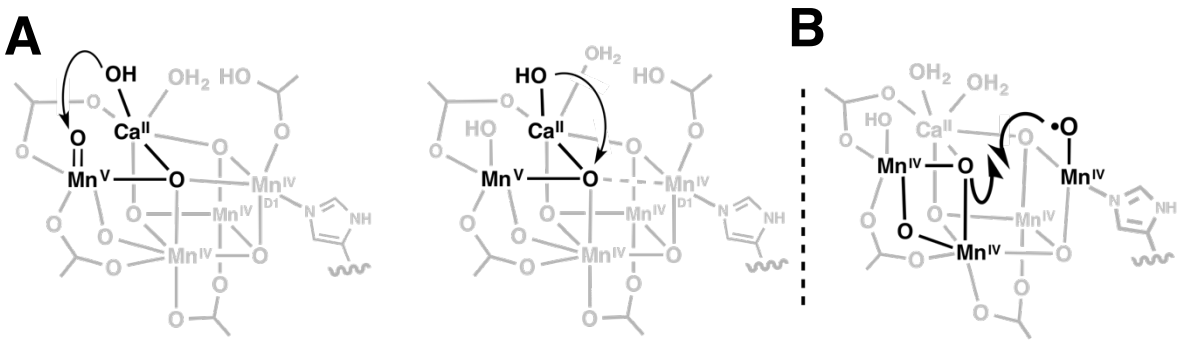

Figure 1.2 Proposed nucleophilic **(A)** and radical **(B)** mechanisms for O–O bond formation.

Synthetic Systems: High valent Metal-Oxido Species

The importance of high valent metal-oxido species in nature has prompted the synthetic community to prepare similar metal complexes in order to further interrogate their functionality. For example, early work generating synthetic Fe^{IV}–oxido species were supported by porphyrin frameworks and reported reactivity towards epoxidation of olefins.[35,36] Additionally, much work has been done preparing non-heme Fe^{IV}–oxido species that have reactivity with a wide range of substrates.[37–39] While generation of these complexes in different ligand environments has offered many new insights into their reactivity, nearly all of the prepared Fe^{IV}–oxido complexes have a S = 1 ground spin state. This is an important fact because one pivotal distinction between heme and non-heme

systems in biology is the spin state of the active intermediates: heme systems have an S = 1 ground state, while non-heme systems are in the S = 2 spin state. In order to analyze the role spin state has on reactivity, chemists have attempted to prepare synthetic compounds with similar magnetic properties to non-heme systems. The first fully characterized example of a non-heme synthetic high spin Fe^{IV}–oxido complex was prepared by the Que lab in 2010 (Figure 1.3A).[40,41] Shortly after, our lab also crystallographically characterized an S = 2 Fe^{IV}–oxido complex (Figure 1.3B).[42] To date, many groups have been influential in advancing the understanding of how these types of complexes react with substrates.[43–46]

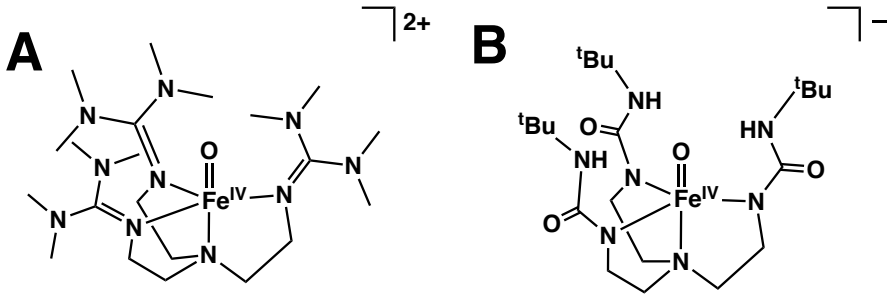

Figure 1.3 $[Fe^{IV}(O)(TMG_3tren)]^{2+}$ (**A**) and $[Fe^{IV}H_3buea(O)]^-$ (**B**).

Synthetic Systems: Developing the Secondary Coordination Sphere

In addition to developing ligand frameworks that can support similar species to those of high valent reactive intermediates in nature, synthetic systems also have been developed to try and replicate the secondary coordination sphere environments found in metalloprotein active sites to understand their mechanistic consequences; however, achieving the precise control and regulated microenvironment demonstrated by natural systems has proven challenging.

One of the first examples of a synthetic system incorporating H-bond groups was introduced by Collman. The work of Collman emulated the chemistry of myoglobin (Mb) and hemoglobin (Hb) through the development of a picket fence porphyrin. Mb and Hb are

respiratory proteins that transfer dioxygen via an Fe^{II}–porphyrin complex and utilize H-bonding interactions to stabilize the O_2 adduct (Figure 1.4). In the absence of a protein host, Fe^{II}–heme complexes dimerize (forming Fe^{III}–O–Fe^{III} aggregates); however, to circumvent this problem, Collman appended pivalamide moieties to increase the steric bulk

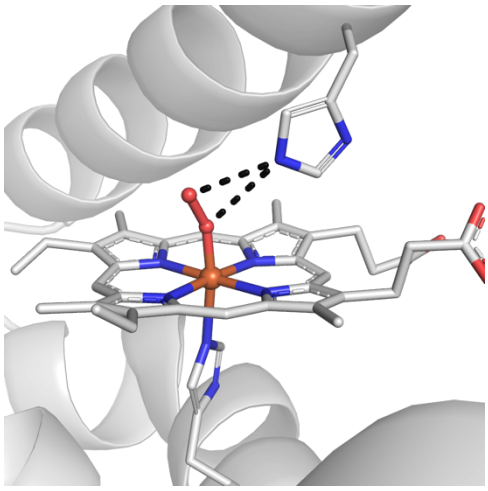

Figure 1.4 The active site in the oxymyoglobin, illustrating the microenvironment around the single heme center and H-bonding to the O_2 ligand (highlighted with black dashed lines). PDB: 1GZX

around the Fe–O_2 unit that blocked, or rather "fenced" off, one face of the porphyrin.[47,48] Combination of the steric bulk provided on one face of the porphyrin and the axially bound N-methylimidazole on the other limited the reactivity of the Fe^{II}–porphyrin species to only the binding of small molecules that could access the metal center within the cavity, e.g. dioxygen. The picket porphyrin design allowed for the isolation and crystallographic characterization of the first synthetic Fe–O_2 adduct (Figure 1.5A).[49,50]

Although, Collman's initial design allowed for replication of a similar primary coordination sphere found within the active sites of Mb and Hb, crystallographic data showed that the amide moieties were too far away (> 5 Å) from the Fe–O_2 unit to participate in H-bonding. In turn, further modifications were made to the picket fence framework to incorporate H-bonding moieties in closer proximity to probe their

interactions with the exogenous O_2 unit. One example introduced an appended phenyl urea substituent that was found to substantially increase the Fe complex's affinity for O_2 binding.[51] The increased affinity was attributed to the H-bonding interaction between the urea N–H and O_2 unit, but no structural data was ever reported (Figure 1.5B).

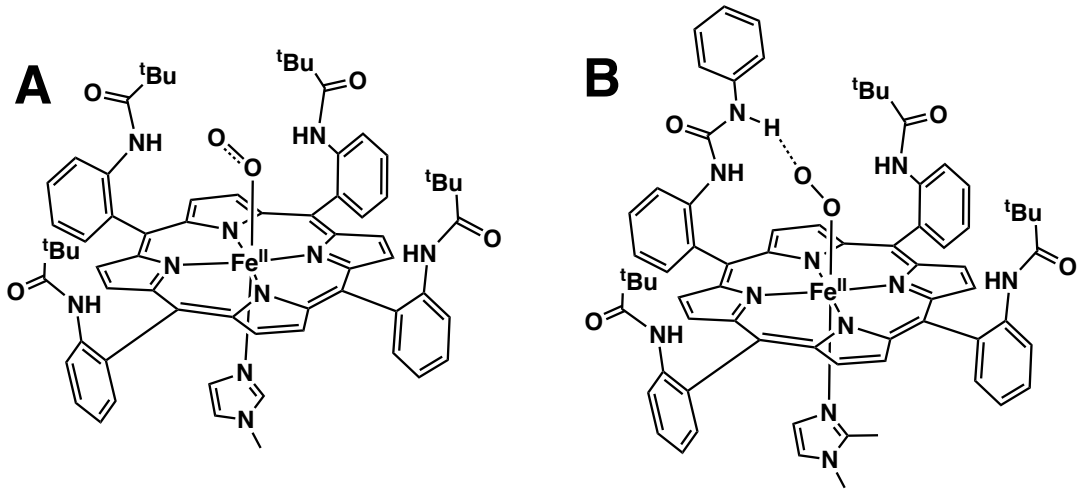

Figure 1.5 Structurally characterized picket fence porphyrin complex supporting an Fe–O_2 adduct (**A**). Modified picket fence porphyrin complex containing a urea group capable of H-bonding (**B**).

The concept of employing rigid organic frameworks to position functional moieties within the local environment of metal ions has developed into an ever-growing field. An array of systems has exemplified how interactions in the secondary coordination sphere can directly affect the reactivity and stability of metallic systems. For example, investigations of H_2 production, from the Du Bois lab, illustrated the dynamic role that the secondary coordination sphere plays in reactivity. Du Bois and coworkers developed nickel complexes housed in a diphosphine ligand scaffold with pendent amine groups positioned in the local environment, much like those found in hydrogenases (Figure 1.6A).[52,53] The outstanding reactivity of this system was attributed to the pendant amine groups that were suggested to act as a proton relay to the metal center. Two more recent examples are from

the labs of Szymczak and Fout. Szymczak and coworkers demonstrated the reversible capture and reduction of dioxygen within a tripodal Zn^{II} complex in which the H-bonding is suggested to play a central role in stabilizing the diatomic molecule (Figure 1.6B).[54] The Fout lab also showed the effects of the secondary coordination within a series of Fe^{II}–OH complexes. Examination of the $Fe^{II/III}$ redox couple was shown to span over a 400 mV range within the series and was attributed to either adding electron-withdrawing groups along the ligand backbone in the primary coordination sphere or changing the capping group in the secondary coordination sphere (Figure 1.6C). Fout and coworkers note structural evidence that supports changing the capping ligand from a cyclohexyl group to a phenyl ring allowed for the N–H moieties to act as stronger H-bond donors, which was reflected in a negative shift in the redox potentials.[55]

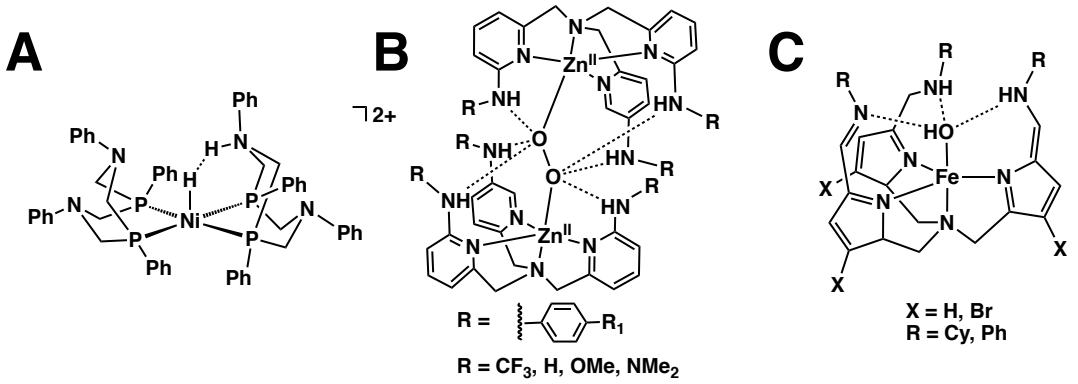

Figure 1.6 Suggested intermediate for H_2 production from Du Bois, highlighting the pendant amine groups that are proposed to shuttle protons (**A**). Dizinc peroxide complex isolated by the Szymczak lab (**B**). Fe^{II}–OH compounds demonstrating an asymmetric H-bonding cavity (**C**).

In addition to studying the implication of H-bonds in synthetic systems, the premise that an auxiliary metal ion affects the function of transition metal centers has also been demonstrated. Work by Agapie has examined the effects of Lewis acids on the properties of manganese-oxido clusters.[56,57] Complimentary work by Lau has shown that, in the presence

of Lewis acids, the rate of alkane oxidation by metal–oxido systems increases.[58] Moreover, Fukuzumi demonstrated that the rate of electron transfer in a Co–porphyrin system is correlated to the Lewis acidity of various redox inactive metal ions. Subsequent work from Fukuzumi and Nam reported that the rate of electron transfer involving an Fe^{IV}–oxido complex is dependent on redox–inactive ions.[59] The Goldberg lab also showed that the addition of Zn^{2+} ions or $B(C_6F_5)_3$ to their Mn^{V}–oxido corrolazine complex resulted in the formation of a Mn^{IV}–oxido/ligand radical system, corroborating suggestions that Lewis acids can have a direct effect on the redox properties of metal-oxido species.[60,61] While the noted examples, amongst others, have provided significant advances towards understanding the influence of redox inactive ions on the reactivity of transition metal ions[62–66], most are not structurally defined. The mononuclear systems described above are commonly a solution of metal complex in the presence of Lewis acids. To this end, the development of molecular systems that are capable of binding both one transition metal ion and a single redox inactive metal ion are limited.[56,67–69]

To highlight one structural example, the Gilbertson lab explored the utility of an asymmetric pyridinediimine ligand that allowed for incorporation of a secondary metal ion by encapsulation in a pendent crown ether (Figure 1.7A).[70] Although only modest shifts in the reduction potential of the Fe complex were observed upon encapsulation of Na^+ or Li^+ ions, it is a promising result that has provided structural evidence of how a Lewis acid can interact with a transition metal complex to influence its redox properties. More recently, work from the Yang group reported on the effect of cations on N–N bond formation for Mn–nitride complexes. Yang and coworkers found that upon addition of redox inactive metals

resulted in Mn^{VI}–nitride complexes that were not only more oxidizing, but also more stable to bimolecular coupling (Figure 1.7B).[71]

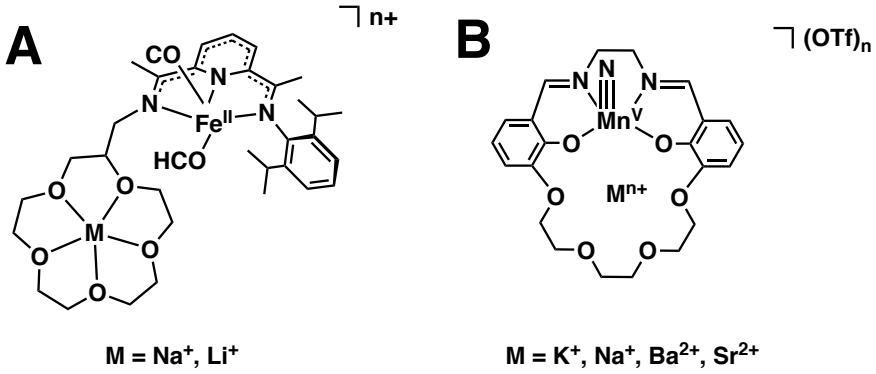

Figure 1.7 Synthetic Fe pyridinediimine complexes investigated by the Gilbertson group (**A**) and appended crown ether Mn–N complexes developed by the Yang group (**B**).

Previous Work in the Borovik Lab

Over two decades, the Borovik group has developed several different tripodal systems that incorporate intramolecular H-bonding interactions within the secondary coordination sphere of a single transition metal center.[72,73] The symmetrical urea ligand $[H_3buea]^{3-}$ (tris[(*N*'–*tert*–butylureaylato)–*N*–ethylene]aminato) provides a cavity with H-bond donors positioned to stabilize nucleophilic metal-oxido complexes. This framework has led to the successful isolation of several monomeric Mn, Co, and Fe complexes with terminal oxido and hydroxido ligands, including the first examples of crystallographically characterized Mn^{III}–oxido and Fe^{III}–oxido complexes, as well as the only reported high spin Mn^{V}–oxido species (Figure 1.8).[42,74,75]

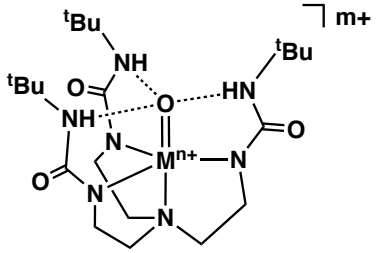

Figure 1.8 Generic metal-oxido complex with $[H_3buea]^{3-}$.

With the library of metal-oxido/hydroxido complexes in hand, the protonation of the well-characterized Fe^{IV}–oxido, $[Fe^{IV}H_3buea(O)]^-$, was examined.[76] Extensive studies showed that a new Fe^{IV} species was generated upon addition of acid to $[Fe^{IV}H_3buea(O)]^-$ at – 80 °C. The new $[Fe^{IV}H_3buea(O)(H)]$ complex was interrogated by UV-visible (UV-vis) and Mössbauer spectroscopies, which confirmed that an Fe^{IV} compound distinct from the initial Fe^{IV}–oxido that was generated. Upon analysis of the vibrational data, the Fe–O vibration was found to be identical to the starting Fe^{IV}–oxido, while the Fe–N vibrations were significantly altered. These data suggested that a major change in the coordination environment about the Fe center was happening upon protonation. Density functional theory (DFT) calculations supported the generation of a protonated Fe^{IV}–oxido complex, where the ligand carbonyl is protonated, leading to tautomerization of the ligand arm to an isourea, which can then participate in an intramolecular H-bond with the oxido ligand (Scheme 1.2).

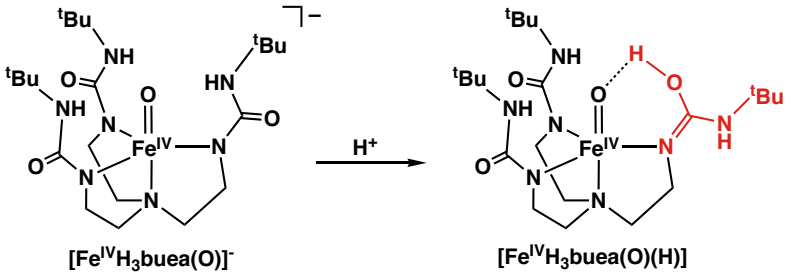

Scheme 1.2 Proposed mechanism of protonation of the $[Fe^{IV}H_3buea(O)]^-$, highlighting the tautomerization of the urea arm in red.

Another system designed to incorporate intramolecular H-bonding interactions is the ligand $[MST]^{3-}$ (*N,N',N"*–[2,2',2"–nitrilotris(ethane–2,1–diyl)]tris–(2,4,6–tri–methylbenzene–sulfonamido), which contains sulfonamide oxygen atoms that can accept H-bonds from an external ligand bound to the metal ion. These oxygen atoms also serve to

establish an auxiliary metal binding site that afforded the isolation of several heterobimetallic systems in high purity having the general form M^{II}–(μ–OH)–TM^{III} (M^{II} = Ca^{II}, Sr^{II}, or Ba^{II} and TM^{III} = Mn^{III} or Fe^{III}) with architectural features that are relevant to protein active sites containing more than one metal ion.[68,77] While investigations of the OEC have found that the presence of a redox–inactive metal ion directly affects the oxidation of water, our group found that the presence of a redox–inactive metal ion influences other redox processes as well; particularly O_2 activation. The effects of group II metal ions on the reactivity of $[MST]^{3-}$ complexes with Mn or Fe showed an increased rate of O_2 activation in the presence of a group II metal ion when compared to the analogous reaction in the absence of a secondary metal ion (Figure 1.9).[77]

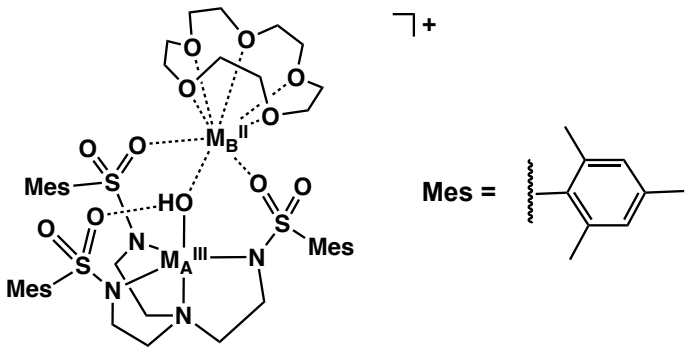

Figure 1.9 Generic heterobimetallic complex [15c5M_B^{II}–(μ-OH)–M_A^{III}MST]. M_B^{II} = Ca^{II}, Sr^{II}, or Ba^{II} and M_A^{III} = Mn^{III} or Fe^{III}

Overview of Remaining Chapters

The research described in this dissertation begins by exploring the chemistry of tripodal ligand systems that contain phosphoryl amide groups and the subsequent chemistry of Mn and Fe systems in an effort to understand how protons and Lewis acids affect high valent metal centers in biology.

Chapter 2. Expanding on the ligand design principles fundamental to the Borovik group, Chapter 2 details the addition of tripodal frameworks that incorporate phosphoryl oxide

(P=O) moieties to our ligand library. The P=O groups are positioned within the secondary coordination sphere of the metal unit and have been found to act as H-bond acceptors as well as binding sites for auxiliary metal ions. Although these features are similar to the previously reported $[MST]^{3-}$ frameworks, work with the symmetrical $[poat]^{3-}$ system or framework has shown that the primary coordination sphere is more conducive to stabilizing metal ions in higher oxidation states (4+), which is not possible with the sulfonamide systems. While several ligands have been designed, this dissertation focuses on chemistry utilizing the following ligands: $[H_2pout]^{3-}$, $[poat]^{3-}$, $[pop]^{3-}$ (Figure 1.10).

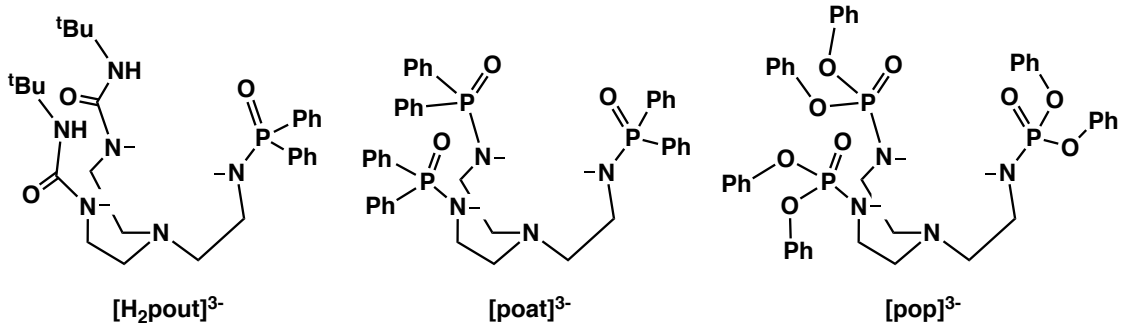

Figure 1.10 Structures of phosphorus containing tripodal ligands utilized in the following chapters.

Chapter 3. The research in this chapter details the development and characterization of a series of Mn–OH complexes in which the oxidation state of the metal center ranges from 2+ to 4+, within the hybrid tripodal ligand $[H_2pout]^{3-}$ that contains two monodeprotonated urea groups and one phosphinic amide. The framework is ideally developed to donate two

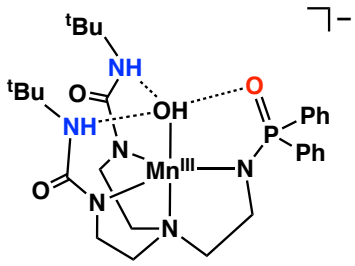

Figure 1.11 Mn–OH complex surrounded by $[H_2pout]^{3-}$ framework. Three intramolecular H-bonds are depicted with black dashed lines.

H-bonds to (the exogenous ligand or hydroxide ligand) and accept one H-bond from the hydroxido ligand (Figure 1.11).

Chapter 4. With the goal of accessing an Fe^{IV}–OH, chapter 4 extends the utility of $[H_2pout]^{3-}$ by detailing the Fe chemistry. The low valent Fe^{II}–OH and Fe^{III}–OH complexes have been fully characterized and methods were developed to access an Fe^{IV} species via the one-electron oxidation of the Fe^{III}–OH complex. The one-electron oxidized species was characterized with parallel-mode electron paramagnetic resonance (EPR), Mössbauer, and nuclear resonance vibrational (NRVS) spectroscopies. Initial results suggested that this complex was the elusive Fe^{IV}–OH species (Figure 1.11A), but preliminary vibration studies suggest an Fe^{IV}–oxido system, which led to preparation of $[Fe^{IV}H_2pout(O)]^-$ by a different route for comparison.

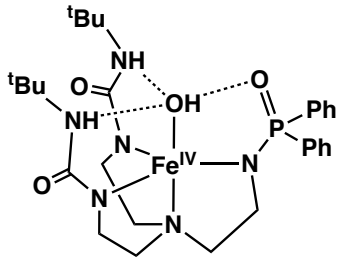

Figure 1.12 Possible Fe^{IV}–OH species of upon oxidation of $[Fe^{III}H_2pout(OH)]^-$.

Chapter 5. The published work with $[H_3buea]^{3-}$ and studies with $[H_2pout]^{3-}$ discussed in Chapters 3 and 4 suggested the need to move away from urea-containing ligands to probe the binding of Lewis acids to Fe–O(H) units. Taking advantage of the properties of $[poat]^{3-}$ described in Chapter 2, the work in chapter 5 reports the preparation and characterization of a new high-spin (S=2) Fe^{IV}–oxido complex and studies that investigate the complex's interactions with Lewis acids. Treating the complex with Lewis acids perturbs the symmetry, which can be followed by changes in key spectroscopic properties (Figure 1.13).

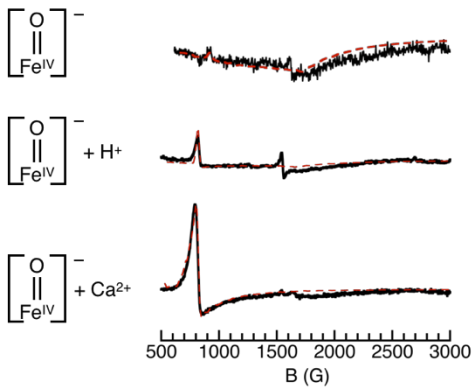

Figure 1.13 Parallel-mode EPR spectra of [Fe^{IV}poat(O)] in the presence and absence of Lewis acids.

Chapter 6. Employing the synthetic versatility of the [poat]$^{3-}$ framework, a series of Fe–hydroxido complexes were developed. Both the Fe^{II}–OH and Fe^{III}–OH complexes have been isolated and characterized. The one electron oxidation of [Fe^{III}poat(OH)]$^{-}$ was accomplished with a chemical oxidant and revealed unusual spectral properties. The oxidized species has a signal in the parallel-mode EPR spectrum that was found to be consistent with an S=2 system; however, the Mössbauer parameters of the complex support an Fe^{III} center. One possible scenario is illustrated in Figure 1.14, which invokes an intramolecular proton transfer followed by intramolecular coupling of a P=O unit to the metal-oxido and leading to O–O bond formation.

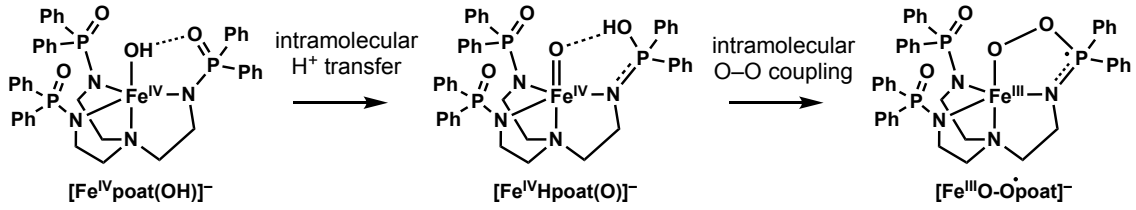

Figure 1.14 One possible mechanistic sequence to produce an Fe^{III}/ligand radical complex from the oxidation of [Fe^{III}poat(OH)]$^{-}$.

CHAPTER 2

Considering the Cavity: Incorporation of Phosphoryl Amides

A foundational tenet of coordination chemistry is the design of ligands to control the physical properties of the bound metal ion. Therefore, the consequence of ligand design is crucial for controlling the reactivity of metal complexes. For this reason, ligand development has been a critical component of the Borovik Group's research for the past twenty-five years.[7,72,73]

Ligands previously designed in our group have employed functional groups such as amidate, ureates, or sulfonamidos (Figure 2.1). These ligands produced a varied of hydrogen bonding (H-bonding) networks surrounding M–O(H) units. Early work focused on deprotonated amide scaffolds $[0^R]^{3-}$ (Figure 2.1A) and showed that changing the steric bulk of the alkyl group had direct consequences for binding of the exogenous ligands the metal complex.[78] The urea-based system $[H_3buea]^{3-}$ (Figure 2.1B) was thought to be able to provide similar primary coordination sphere effects as seen for the amide systems, while introducing secondary coordination sphere interactions: H-bond donation to an exogenous ligand from the urea N–H moieties. As mentioned in the previous chapter, the $[H_3buea]^{3-}$ framework allowed for the isolation of many prominent metal-oxido/hydroxido species.[42,74,79–82] Design concepts further extended to changing the polarity of the cavity

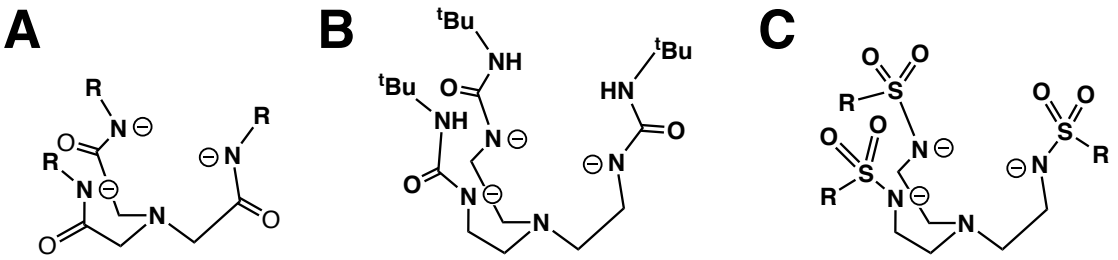

Figure 2.1 Ligands previously designed in the Borovik group: $[0^R]^{3-}$ (**A**), $[H_3buea]^{3-}$ (**B**), $[RST]^{3-}$ (**C**).

with incorporation of sulfonamido moieties that could serve as H-bond acceptors to an exogenous hydroxido or aqua ligand, as well as serve as an auxiliary binding site for a second metal ion. $[RST]^{3-}$ (Figure 2.1C) supported several of monomeric M–OH and $M–OH_2$ systems, as well as families of heterobimetallic complexes with both one transition metal ion and one redox inactive ion,[68,77,83] as well as with two transition metal ions.[84,85]

Even with all of these significant results, there were limitations with some of the designs, particularly ligands with the sulfonamido groups because the associated metal complexes could not access high valent species, those with oxidation state greater than +3. To circumvent these problems, the group was inspired by the works of the Stephan group,[86] and designed ligand systems containing phosphoryl amide groups to control the local environments around M–O(H) units.

With phosphoryl amide containing scaffold, the subsequent monomeric and heterobimetallic complexes should be able to support higher valent species with oxido, hydroxido, and aqua ligands than those previously seen with the $[RST]^{3-}$ framework. Incorporating phosphoryl amide containing donors was proposed to have two advantages: 1) the phosphoryl amido nitrogen atom is more electron–rich than the sulfonamido nitrogen atom, which should allow access to higher oxidation states of the corresponding metal complexes, and 2) the oxygen atoms of the P=O units will be more electron rich, which will make them better ligands to auxiliary metal ions.

The two symmetrical ligand precursors employed in this dissertation are illustrated in Figure 2.2. The synthesis of H_3poat and H_3pop are accomplished in a one-pot reaction

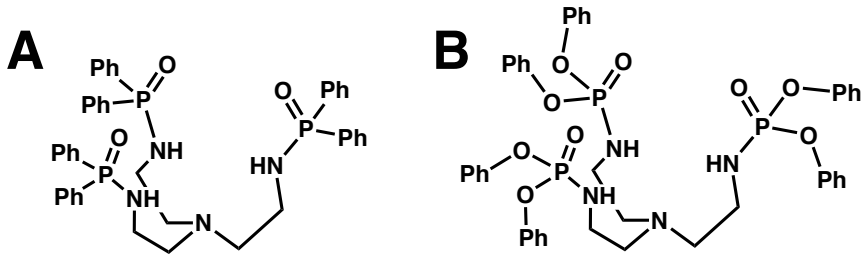

Figure 2.2 Symmetrical phosphoryl amide ligand precursors: H_3poat (**A**), H_3pop (**B**).

with tris(2-aminoethyl)amine and appropriate phosphoryl chloride (Scheme 2.1). Mn and Fe complexes have been prepared with both ligand frameworks ($[poat]^{3-}$ and $[pop]^{3-}$), and the P=O moieties have been shown to be capable of both serving as H-bond acceptors as well as ligands to bind a second metal ion.

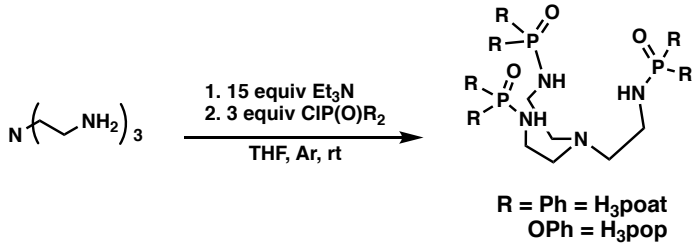

Scheme 2.1 General synthesis of symmetrical phosphoryl amide tripods.

With the straight forward synthesis of H_3poat and H_3pop, it is reasonable to expand the phosphorus ligand library utilizing commercially available reagents. Modifications such as changing the steric bulk off the P=O unit or trading the P=O with a P=S would be expected to alter the properties of the primary and secondary coordination spheres of subsequent metal complexes and could open doors to unexplored chemistry (Figure 2.3).

In addition to symmetrical frameworks, our group has designed several hybrid ligands: whereby a hybrid ligand is defined as having at least one unique arm. Adapting a protocol

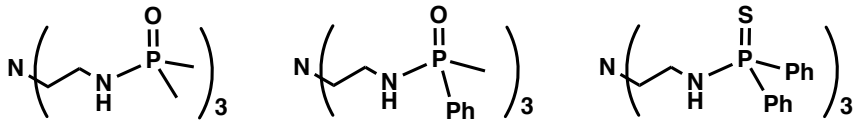

Figure 2.3 Proposed ligand precursors that could be synthesize in an analogous manner as H_3poat and H_3pop.

from a previous group member,[87] Dr. Jason Jones developed a methodology for synthesizing hybrid sulfonamide/urea tripods and analyzed how both the changes in primary and secondary coordination spheres affected a series of Co^{II}–OH complexes (Figure 2.4A).[88] With the desire to investigate high valent metal-hydroxido complexes, H_5pout (Figure 2.4B, Scheme 2.2) was synthesized in an analogous fashion to the

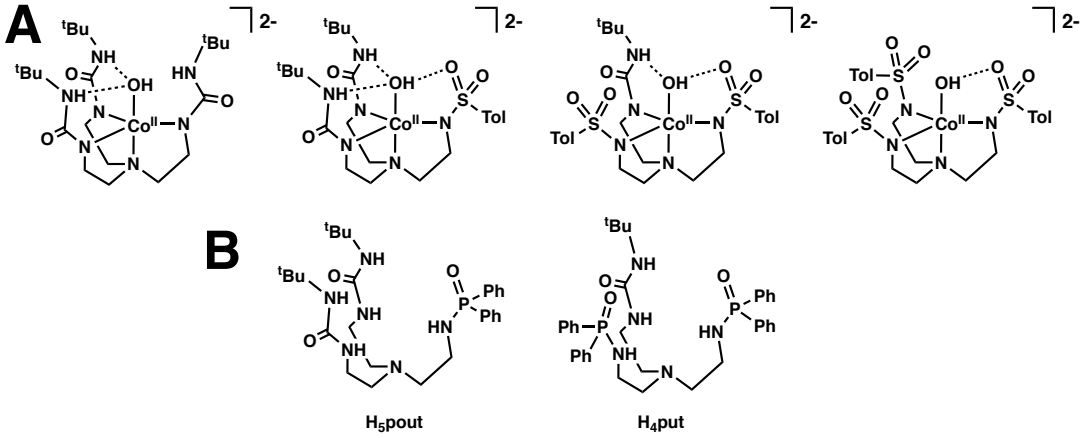

Figure 2.4 Co^{II}–OH series with varying H-bond networks (**A**), and analogous phosphinic amide hybrid ligand precursors (**B**).

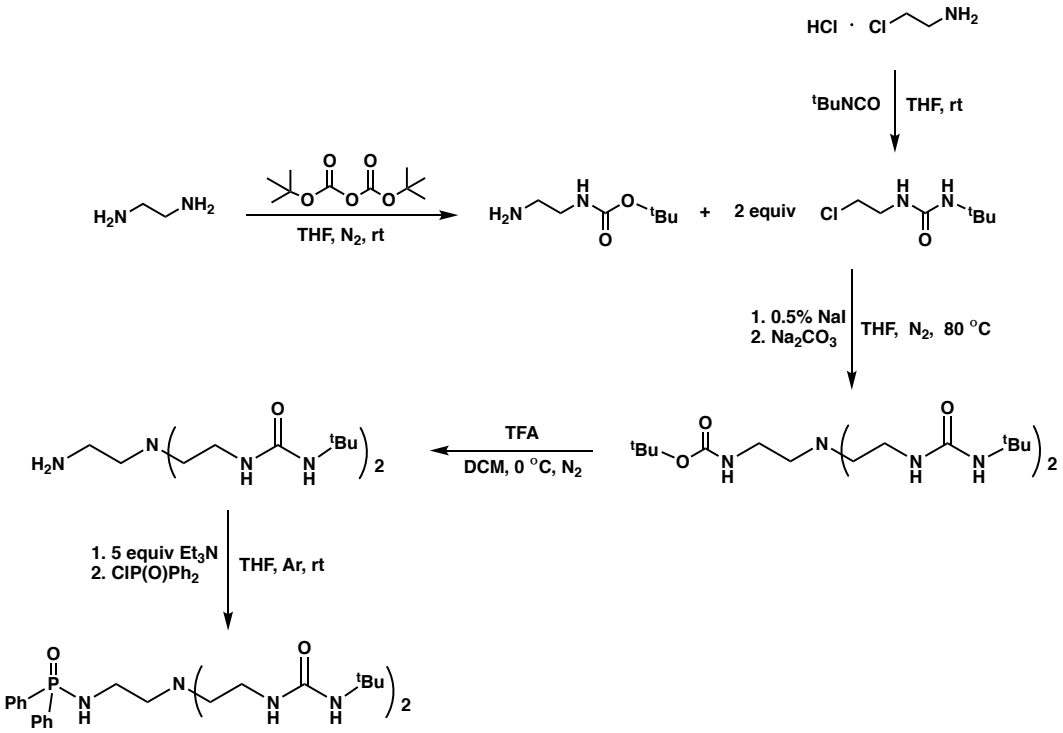

Scheme 2.2 Synthesis of H_5pout.

corresponding two urea/one sulfonamido hybrid ligand and employed to synthesize and probe series of M–OH (M = $Mn^{II/III/IV}$; $Fe^{II/II/IV}$) species. H_4put (Figure 2.4B) has yet to be prepared, but could be useful for future studies, especially in preparation of heterobimetallics. Data from both sulfonamido systems, as well as $[poat]^{3-}$ and $[pop]^{3-}$, suggest that the second metal binds to two O–atoms from the ligand framework and the O–atom from the exogenous ligand.

The ligand $[H_2bupa]^{3-}$ is another example of a hybrid ligand that incorporated one pivalamide, a moiety utilized prior by Masuda,[89] and was employed to synthesize a Mn^{III}–peroxido complex (Figure 2.5A).[90] Subsequent studies showed that the $[Mn^{III}H_3bupa(O_2)]^-$ complex was an intermediate in the conversion of dioxygen to water by $[Mn^{II}H_2bupa]^-$. To date, the $[Mn^{II}H_2bupa]^-$ system is the only example in our lab of a complex performing catalytic reactivity.[91] Taking a closer look at the system, the increased reactivity of a metal complex supported by $[H_2bupa]^-$ may not be too surprising, because it is the only scaffold that the pendant functional group has been found to be hemilabile to the metal center. Metal-ligand cooperation has shown to be influential in wide range of chemical transformations.[92–97]

Although this feature has not been directly identified as the cause of reactivity, the labile binding of the appended carboxyamido group in $[H_2bupa]^-$ clearly affects functionality of the coordinated metal ion, which is different from our other frameworks. Extending from the design of H_5bupa, replacement of the two urea arms with phosphinic amide arms would allow us to increase the complexity in the secondary coordination sphere of a metal complex. For example, the framework would now be expected to have the capacity of binding of a second metal ion, while still allowing ligand participation, which

could be critical for enhanced catalytic function. A proposed generic metal complex is shown in Figure 2.5B, which highlights the binding of a second metal ion as well as intramolecular hydrogen bonding.

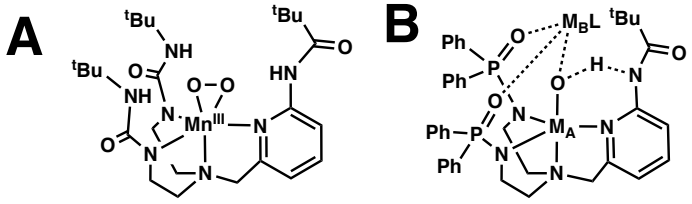

Figure 2.5 $[MnH_3bupa(O_2)]^-$ (**A**). Proposed heterobimetallic metal complex (**B**).

The following work in this dissertation begins the exploration into the rich chemistry that is possible from the utilization of tripodal ligand frameworks containing N–P=O moieties.

Experimental.

General Methods.

All reagents were purchased from commercial sources and used as received, unless otherwise noted. Solvents were sparged with argon and dried over columns containing Q-5 and molecular sieves. H_3poat and H_3pop was prepared under an Ar atmosphere using a protocol adapted from the synthesis of H_3PAT.[86]

Preparation of Ligands.

H_3poat. To a solution of tris(2-aminoethyl) amine (tren) (1.12 g, 7.60 mmol) and triethylamine (11.65 g, 115.1 mmol) in 80 mL tetrahydrofuran (THF), diphenyl phosphinic chloride (5.51 g, 23.3 mmol) in 20 mL THF was added dropwise while stirring. Once the addition was complete, 20 mL THF was added to rinse the addition funnel. After the addition funnel was removed, the round bottom was covered with a glass stopper and left

to stir overnight. After filtering the white precipitate (Et_3NHCl), the solvent was removed and the residue was dried under vacuum. Diethyl ether (Et_2O) (125 mL) was added to the resulting oil to give a white powder (82%), which was collected on a medium porosity glass-fritted funnel, then washed twice with ether (40 mL) and dried for several hours under vacuum. ^{1}H NMR (500 MHz, DMSO, ppm): 2.45 (*t*, 6H), 2.82 (*q*, 6H), 5.66 (*q*, 3H), 7.42 (*t*, 12H), 7.50 (*d*, 6H), 7.70 (*t*, 12H). ^{31}P NMR (162 MHz, $CDCl_3$, ppm): 21.6; FTIR (KBr, selected bands cm^{-1}): 3130, 3261; 2970, 2941, 2870, 2790, 2604, 2497, 1590, 1438, 1188, 1122, 724, 697, 517. HRMS (ES+, m/z): Exact mass calculated for $C_{42}H_{45}N_4O_3P_3$: 746.27, Found: 746.85 1H NMR (400 MHz, $CDCl_3$, ppm): 2.44 (6H, br *t*), 2.81 (6H, *q*, *J* = 6.6 Hz), 5.64 (3H, *q*, *J* = 10.1 Hz, NH), 7.43 (12H, *d*, *J* = 8.9 Hz, *o*-Ar), 7.51 (6H, *t*, J = 8.9 Hz, *p*-Ar), 7.68 (12H, *t*, *J* = 9.8, *m*-Ar)

H_3pop. To a 500 mL round bottom flask containing tris(2-aminoethyl) amine (tren) (2.12 g, 13.8 mmol) and triethylamine (20.02 g, 197.8 mmol) in 100 mL THF, diphenyl phosphoryl chloride (11.41 g, 42.47 mmol) in 50 mL THF was added dropwise while stirring. Once the addition was complete, 50 mL THF was added to rinse the addition funnel. After the addition funnel was removed, the round bottom was covered with a glass stopper and left to stir overnight. After filtering the white precipitate (Et_3NHCl), the solvent was removed and the residue was dried under vacuum. Et_2O (150 mL) was added to the resulting residue to give a white powder (88%), which was collected on a medium porosity glass-fritted funnel, then washed twice with ether (50 mL) and dried for several hours under vacuum. ^{1}H NMR (500 MHz, DMSO, ppm): 2.50 (*t*, 6H), 3.11 (*q*, 6H), 6.13 (*q*, 3H), 7.45 (*t*, 12H), 7.50 (*d*, 6H), 7.61 (*t*, 12H); ^{13}C NMR (125 MHz, DMSO, ppm): 151.0, 130.3, 125.2, 120.5, 56.5, 47.2; ^{31}P NMR (162 MHz, $CDCl_3$, ppm): 21.9; FTIR (KBr, selected bands cm^{-1}): 3304, 3237,

1589, 1487, 1377, 1241, 1192, 1111, 1076, 934, 919, 762, 690. HRMS (ES+, m/z): Exact mass calculated for $NaC_{42}H_{45}N_4O_9P_3$ [M + Na]: 865.23, Found: 865.2297

H_5pout. The preparative route for this compound followed the method previous report for H_2**2**^{Tol} in which only the last step was different.[88] A solution of 1,1′-(((2-aminoethyl)azanediyl)bis(ethane-2,1-diyl))bis(3-(*tert*-butyl)urea) (2.00 g, 4.47 mmol) and triethylamine (2.55 g, 25.2 mmol) in 100 mL anhydrous THF was treated dropwise with diphenyl phosphinic chloride dissolved in 100 mL THF (~1 drops/second) while stirring and a white precipitate formed immediately. Once the addition was complete, 100 mL THF was added to rinse the addition funnel. The addition funnel was removed, and the round bottom flask was covered with a glass stopper. After stirring overnight, the white precipitate, Et_3NHCl, was removed via filtration. The filtrate was dried under reduced pressure and the solid residue was further dried under vacuum. Diethyl ether (150 mL) was added to the residue to afford an off-white powder, which was collected on a medium porosity glass-fritted funnel, washed once with MeCN (50 mL), twice with Et_2O (50 mL), and dried for several hours under reduced pressure to give the desired white product (2.7 g, 85 %). ^{1}H NMR (500 MHz, $CDCl_3$, ppm): 1.33 (18H), 2.42 (6H), 2.94 (2H), 3.17 (4H), 7.48 (4H), 7.55 (2H), 7.86 (4H); ^{13}C NMR (125 MHz, $CDCl_3$, ppm): 29.7, 36.3, 45.7, 49.7, 128.9 (d), 130.8, 131.9, 132.0 (d), 132.4 (d), 158.5. ^{31}P NMR (162 MHz, $CDCl_3$, ppm): 28.6; HRMS (ES+, m/z): Exact mass calculated for $NaC_{28}H_{45}N_6O_3P$ [M + Na]: 567.3188, Found: 567.3186. FTIR (Nugol, cm^{-1}): 3400, 3341, 3231, 2954, 2922, 2853, 1678, 1657, 1546, 1451, 1378, 1287, 1264, 1221, 1120, 1047, 814, 723, 690.

CHAPTER 3

Mn-hydroxido Complexes Supported by Urea/Phosphinic Amide Tripod

To determine correlations between the structure and function of a metal complex, it is necessary to understand the relationships between the primary and secondary coordination spheres of the metal ion(s).[4,6,7,98] Control of the primary coordination sphere is often governed via relatively strong M–L covalent bonds, which chemists have utilized in a variety of ways. Rather than using covalent bonds, the secondary coordination spheres of metal ions are regulated through networks of weaker non-covalent interactions that are often difficult to manipulate within synthetic systems.[99,100] Hydrogen bonds (H-bonds) are the most versatile of these interactions and have been actively designed into a variety of ligand frameworks. The most common of these ligands incorporate either H-bond donors or acceptors to promote intramolecular H-bonds.[4,87,101–110] There are fewer examples that utilize a mixture of H-bond donors/acceptors to target a specific type of M–L unit.[88,111–113]

Our group has specialized in the development of ligand platforms that promote intramolecular H–bonding networks to investigate their influence on the secondary coordination sphere. One design uses the symmetrical urea ligand $[H_3buea]^{3-}$ (Figure 3.1A) that provides a cavity with three H-bond donors positioned to stabilize monomeric Mn, Fe, Co, and Ni complexes with terminal oxido/hydroxido ligands.[75,82,98,114–118] Previous researchers found that the strongly anionic ligand field provided by the mono-deprotonated urea groups also assists in stabilizing high valent species that includes Mn^{V}-oxido and Mn^{IV}–hydroxido complexes.[75,119,120] Previous studies also examined the chemistry of tripodal ligands such as $[RST]^{3-}$ (Figure 3.1B), which contains deprotonated sulfonamide units that also function as H-bond acceptors.[68,69,121,122] Recently, hybrid

tripods were introduced that contain both ureate and sulfonamido groups to vary the intramolecular H-bonding network that surrounds Co–OH units (Figure 3.1C).[88] These studies showed that deprotonated sulfonamido ligands are useful H-bond acceptors; however, they do not provide a sufficient primary coordination sphere to stabilize monomeric M–OH complexes with oxidation states greater than 3+.

To circumvent this problem, I have turned to ligands that contain deprotonated

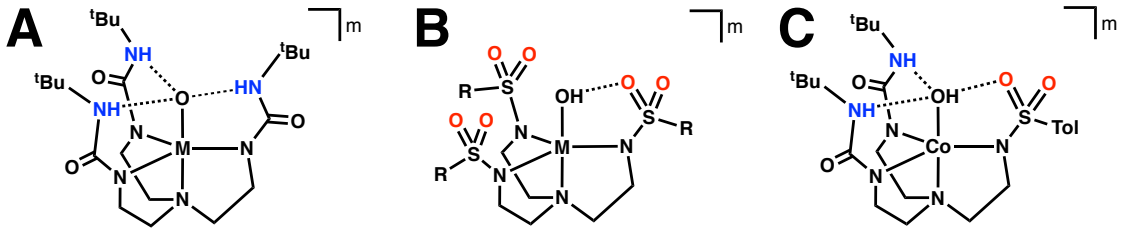

Figure 3.1 Metal complexes surrounded by ligand frameworks with various H-bond networks: (**A**) $[H_3buea]^{3-}$, (**B**) $[RST]^{3-}$, and (**C**) $[H_2 2^{tol}]^{3-}$. H-bond donating groups are shown in blue, while accepting moieties are highlighted in red. The H-bond interactions are illustrated with black dotted lines.

phosphinic amides in place of sulfonamido groups. Phosphinic amides would produce a stronger anionic ligand field to stabilize high valent species, while still providing H-bond acceptors through the P=O units. This chapter describes the development and Mn chemistry of the hybrid ligand $[H_2pout]^{3-}$ (Figure 3.2) that installs a combination of two H-bond donors and one H-bond acceptor within the secondary coordination sphere. The $[H_2pout]^{3-}$ ligand was used to prepare the Mn^{II}–OH complex $[Mn^{II}H_2pout(OH)]^{2-}$ (Figure 3.2), which had sufficiently low redox potentials to synthetically prepare its corresponding Mn^{n}–OH (n = III, IV) analogs.

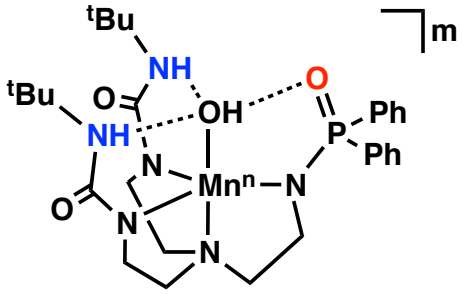

Figure 3.2 Metal complex within the $[H_2pout]^{3-}$ framework where n = 2+, m = 2-; n = 3+, m = 1-; n = 4+, m = 0.

Results and Discussion

Synthesis. The preparation of H_5pout was accomplished in a five-step convergent synthesis adapted from the methods developed for previously reported $H_5 2^{tol}$ ligand (Figure 3.1C).[88] Central to the syntheses is the diurea compound, 1,1′-((2-aminoethyl)azanediyl)bis (ethane-2,1-diyl))bis(3-(*tert*-butyl)urea, which is combined in the final step with diphenylphosphinic chloride in THF and excess Et_3N. Precipitation of the ammonium chloride salt was observed immediately, and H_5pout was isolated as a white solid in 85% yield after purification.

The Mn^{II}–OH complex, $[Mn^{II}H_2pout(OH)]^{2-}$, was synthesized following the procedure outlined in Scheme 3.1 in which the ligand was initially formed via deprotonation with KH. Metal ion coordination was achieved using $Mn^{II}(OAc)_2$ and the hydroxido ligand was derived from water; note that an extra equivalent of base was added to the reaction mixture, which is needed to produce the hydroxido ligand in $[Mn^{II}H_2pout(OH)]^{2-}$. One-

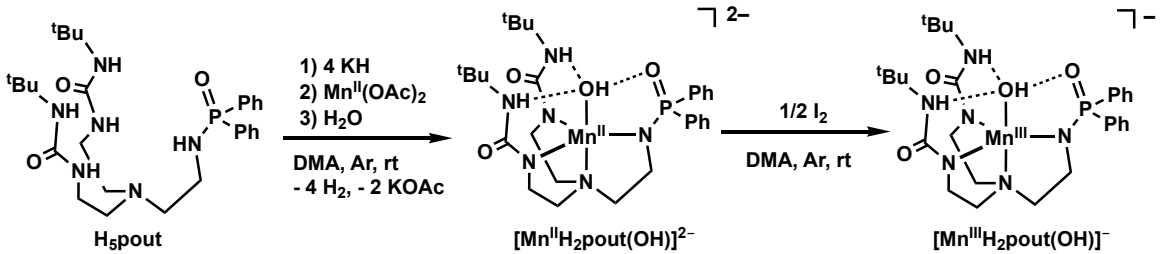

Scheme 3.1 Preparation of Mn–OH complexes.

electron oxidation of the Mn^{II}–OH complex with elemental iodine gave the corresponding Mn^{III}–OH species, $[Mn^{III}H_2pout(OH)]^-$ (Scheme 3.1).[123]

Structural Properties. The molecular structures of the $K_2[Mn^{II}H_2pout(OH)]$ and $K[Mn^{III}H_2pout(OH)]$ salts were characterized with X-ray diffraction methods (Figure 3.3, Tables 3.1 and 3.2). DFT calculations gave optimized structures for both that agreed with the molecular structures determined by XRD measurements (Table 3.2). The structures for both salts revealed that each Mn–OH anion is mononuclear with a distorted trigonal bipyramidal (tbp) coordination geometry. The primary coordination sphere around the Mn

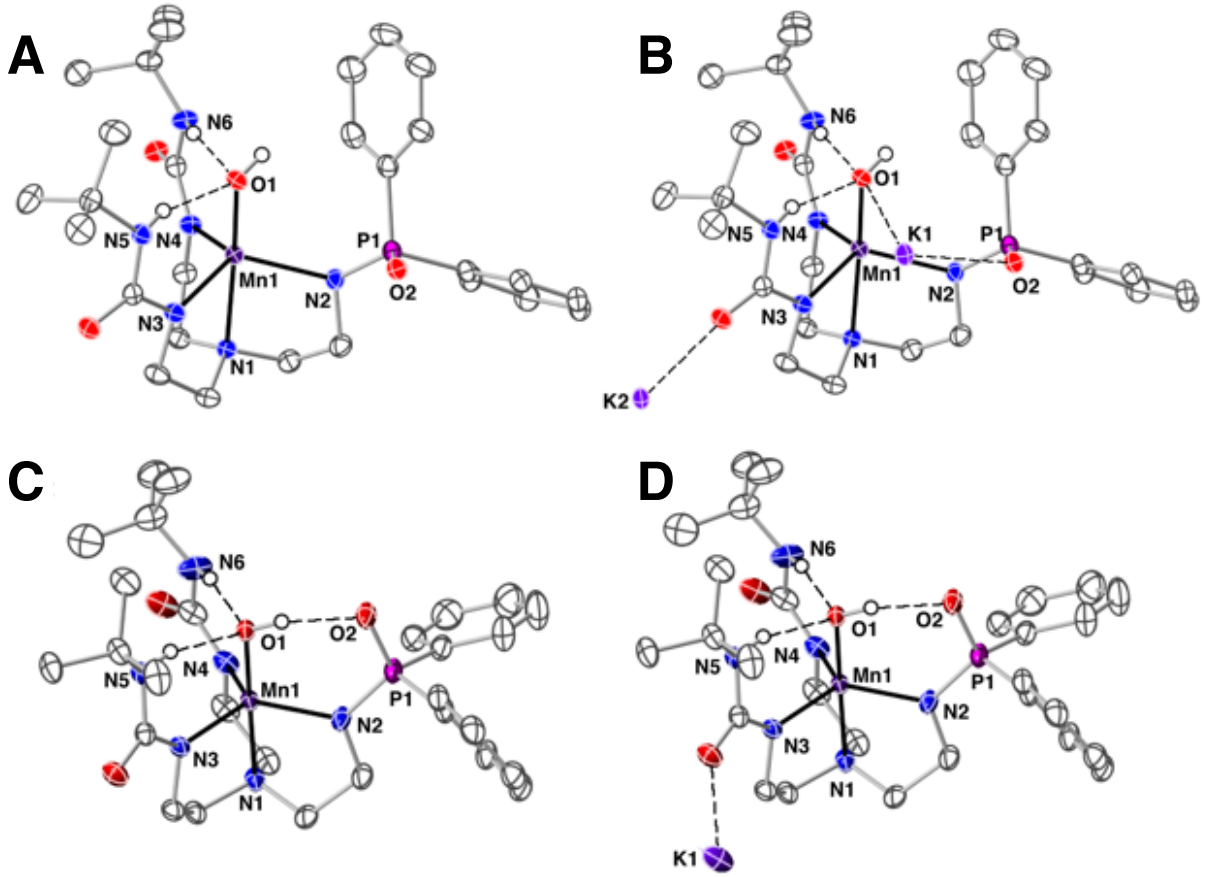

Figure 3.3 Thermal ellipsoid plots of $[Mn^{II}H_2pout(OH)]^{2-}$ (**A**), $K_2[Mn^{II}H_2pout(OH)]$ (**B**), $[Mn^{III}H_2pout(OH)]^-$ (**C**), $K[Mn^{III}H_2pout(OH)]$ (**D**). Thermal ellipsods are drawn at the 50% probability level, only urea and hyrdoxido hydrogen atoms are shown for clarity.

center in each complex is composed of a N_4O donor set with three anionic N-atom donors forming the trigonal plane. The axial site contains the apical amine N1-atom from the $[H_2pout]^{3-}$ ligand and O1-atom from the hydroxido ligand. Statistically significant differences are found between the Mn–N and Mn–O1 bond lengths between the two structures. For instance, the Mn–O1 bond distance is contracted from 2.051(1) Å to 1.834(1) Å upon conversion to $[Mn^{III}H_2pout(OH)]^-$, a change that is consistent with oxidation at the metal center. A similar shortening in bond lengths after oxidation is observed for the bonds within the equatorial plane in which the average Mn–N bond distance changed from 2.188(1) Å to 2.052(2) Å.

Table 3.1 Crystallographic Data and Structure Refinement Parameters

Complex	$K_2[Mn^{II}H_2POUT(OH)]$	$K[Mn^{II}H_2POUT(OH)]$
Empirical Formula	$C_{36}H_{61}K_2MnN_8O_6P$	$C_{36}H_{61}KMnN_8O_6P$
Formula weight	866.03	776.87
Crystal system	Orthorhombic	Triclinic
Space group	Pbca	$P\bar{1}$
a (Å)	17.8861(7)	11.5758(11)
b (Å)	21.3269(8	13.6752(13)
c (Å)	23.3999(9	14.4278(14)
α (°)	90°	70.2118(11)°
β (°)	90°	72.9494(11)°
χ (°)	90°	73.1226(12)°
Volume ($Å^3$)	8926.0(6)	2007.7(3
Z	8	2
δcalc (Mg/m3)	1.289	1.285
GOF	1.015	1.032
R1	0.0343	0.0377
wR2	0.0823	0.092
CCDC Code	1849229	1849228

The molecular structures also show that $[H_2pout]^{3-}$ interacts with the Mn–OH unit through H-bonds to influence the secondary coordination sphere. In each structure, the

urea NH groups serve as H-bond donors to the hydroxido ligand as judged by the average N···O distances of 2.910(2) Å in $[Mn^{II}H_2pout(OH)]^{2-}$ and 2.774(2) Å in $[Mn^{III}H_2pout(OH)]^{-}$. There is a third intramolecular H-bond in the Mn^{III}–OH structure that is formed between the hydroxido ligand and the O2-atom of the phosphinic group (2.685(2) Å). The presence of this additional H-bond could account for the shorter Mn–O bond distance in $[Mn^{III}H_2pout(OH)]^{-}$ when compared to that found in $[Mn^{III}H_3buea(OH)]^{-}$ (Figure 3.1A, Mn–O bond length of 1.877(2) Å).[124] Since the hydroxido acts as an H-bond donor, it should have more negative character, which would result in a shorter Mn1–O1 bond distance in $[Mn^{III}H_2pout(OH)]^{-}$. Similar structural results were found in Co–OH complexes and emphasized the structural effects of the H-bonds within the secondary coordination sphere.[88] Notice also that the potassium ion does not interact with the Mn–OH unit in the lattice of $K[Mn^{III}H_2pout(OH)]$; it only interacts with the carbonyl groups of the ureas, which are pointed away from the hydroxido ligand (Figure 3.3D).

Similar comparison for $[Mn^{II}H_2pout(OH)]^{2-}$ are hindered because the positioning of the potassium ions complicates interpretation of the secondary coordination sphere. One potassium ion (K2) interacts with the O2-atom of $[H_2pout]^{3-}$ that distorts the cavity and prevents formation of an intramolecular H-bond (Figure 3.3B). The O–H bond is positioned toward the phosphinic unit in a similar manner as in $[Mn^{III}H_2pout(OH)]^{-}$, but it is now closer to one of the phenyl substituents. This lack of a third intramolecular H-bonds results in a Mn1–O1 bond length that is the statistically the same as that found in the related Mn^{II}–OH complex, $[Mn^{II}H_3buea(OH)]^{2-}$ (Mn–O bond distance of 2.059(2) Å).[82]

Table 3.2 Selected Bond Distances and Angles for $K_2[Mn^{II}H_2poutOH)]$ and $K[Mn^{III}H_2pout(OH)]$ Determined by XRD and DFT Methods.

Bond Distances (Å) or Angles (˚)	XRD	DFT	XRD	DFT
	$K_2[Mn^{II}H_2pout(OH)]$		$K[Mn^{III}H_2pout(OH)]$	
Mn(1)-O(1)	2.051(1)	2.07	1.834(1)	1.85
Mn(1)-N(1)	2.315(1)	2.46	2.054(2)	2.11
Mn(1)-N(2)	2.214(1)	2.17	2.056(2)	2.03
Mn(1)-N(3)	2.220(1)	2.15	2.035(2)	2.06
Mn(1)-N(4)	2.121(1)	2.20	2.068(2)	2.10
O(1)···O(2)	3.958(2)		2.685(2)	2.71
O(1)···N(5)	2.768(2)	2.79	2.776(2)	2.78
O(1)···N(6)	3.053(2)	2.83	2.773(2)	2.77
O(1)-Mn(1)-N(1)	170.13(5)	172	179.18(7)	178
O(1)-Mn(1)-N(2)	103.60(5)	100	97.36(6)	99
O(1)-Mn(1)-N(3)	93.48(5)	98	97.49(6)	98
O(1)-Mn(1)-N(4)	108.76(5)	111	98.82(6)	97
N(1)-Mn(1)-N(4)	78.68(5)	77	81.91(7)	82
N(1)-Mn(1)-N(2)	78.62(5)	77	81.96(6)	83
N(2)-Mn(1)-N(4)	112.73(5)	107	116.27(7)	118
N(3)-Mn(1)-N(1)	77.22(5)	77	82.53(6)	81
N(3)-Mn(1)-N(2)	119.46(5)	116	124.58(7)	125
N(3)-Mn(1)-N(4)	115.48(5)	122	113.59(7)	111

Electronic Absorbance and Vibrational Properties. The conversion of $[Mn^{II}H_2pout(OH)]^{2-}$ to $[Mn^{III}H_2pout(OH)]^{-}$ was monitored by optical spectroscopy in 1:1 DMF:THF at – 80˚C. The Mn^{II}–OH species had no observable features in the visible region but upon oxidation new bands appeared at $\lambda_{max}(\varepsilon_M)$ = 440 (210) and 740 (236) nm (Figure 3.4A). The energies of these features are similar to those found in the related Mn^{III}–O(H) complexes $[Mn^{III}H_3buea(O)]^{2-}$ and $[Mn^{III}H_3buea(OH)]^{-}$; however, there are noticeable differences in the values of the extinction coefficients. For $[Mn^{III}H_3buea(OH)]^{-}$, bands were observed at $\lambda_{max}(\varepsilon_{\#M})$ = 427 (ε_1 = 390) and 720 (ε_2 = 500) nm ($\varepsilon_1/\varepsilon_2$ = 0.78) that change in $[Mn^{III}H_3buea(O)]^{2-}$ to $\lambda_{max}(\varepsilon_M)$ = 498 (ε_1 = 490) and 725 (ε_2 = 240) nm ($\varepsilon_1/\varepsilon_2$ = 2.0).[81] In

addition, an analogous Mn^{III}–OH in tbp coordination geometry with no intramolecular H-bonds has a similar visible absorbance spectrum in which the lower energy band has the greater intensity ($\varepsilon_1/\varepsilon_2 = 0.62$).[125] The comparable extinction coefficients of the absorbance bands in the spectrum of $[Mn^{III}H_2pout(OH)]^-$ ($\varepsilon_1/\varepsilon_2 = 0.89$) may be attributed to the Mn–OH unit being an H-bond donor to form a relatively strong H-bond with the phosphinic amide O–atom; this additional interaction would make the hydroxido ligand slightly more oxido-like, which would affect a change in the absorbance spectrum as observed.

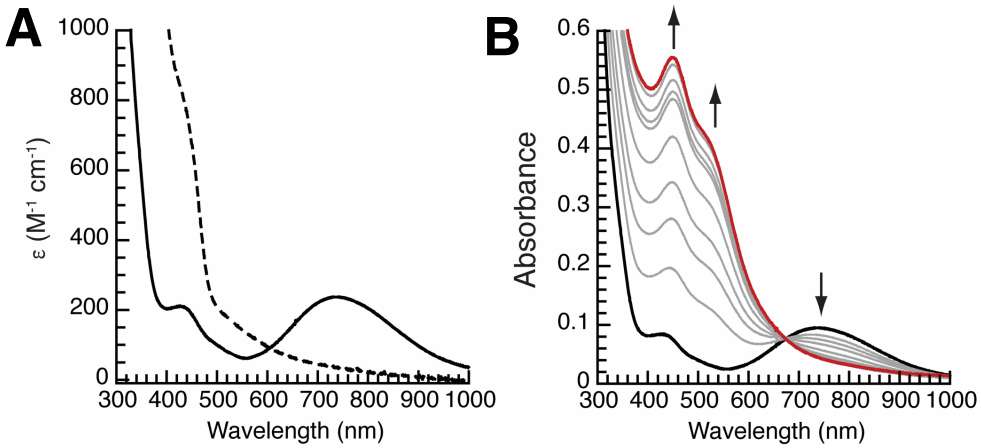

Figure 3.4 UV-visible spectra monitoring the conversion of $[Mn^{II}H_2pout(OH)]^{2-}$ (black dashed) to $[Mn^{III}H_2pout(OH)]^-$ (black solid) (**A**) and $[Mn^{III}H_2pout(OH)]^-$ to $[Mn^{IV}H_2pout(OH)]$ (red solid) (**B**). Spectra were recorded in a 1:1 DMF:THF mixture at – 80 °C.

Analysis of vibrational properties using FTIR spectroscopy showed bands attributed to the ν(MnO–H) at 3656 and 3300 cm^{-1} for the Mn^{II}–OH and Mn^{III}–OH complexes (Figure 3.5). Because of the interactions of the potassium ions with $[Mn^{II}H_2pout(OH)]^{2-}$ (Figure 3.3B) it is not possible to directly compare this complex with other Mn–OH species. A more straight forward comparison can be made for $[Mn^{III}H_2pout(OH)]^-$ and its ν(MnO–H) band is boarder (fwhm = 90 cm^{-1}) and at lower energy than the comparable peak for $[Mn^{III}H_3buea(OH)]^-$, which was found at 3613 cm^{-1} (fwhm = 15 cm^{-1}).[124] These vibrational

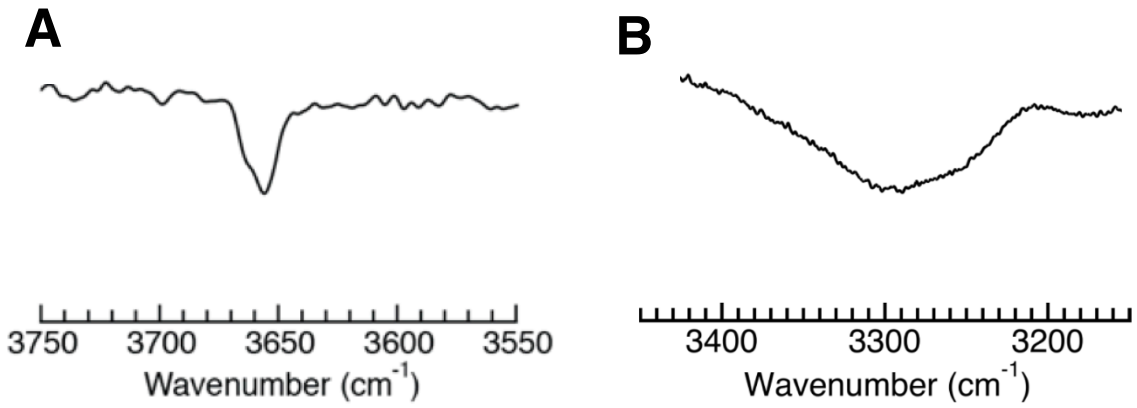

Figure 3.5 FTIR spectra for $[Mn^{II}H_2pout(OH)]^{2-}$ (**A**) and $[Mn^{III}H_2pout(OH)]^{-}$ (**B**) illustrating the region for the O–H vibration.

data are also consistent with the presence of an intramolecular H-bond between the phosphinic arm and the hydroxido ligand that causes a weakening of the O–H bond.

Electrochemical Properties. Cyclic voltammetry (CV) was employed to analyze the redox properties of the Mn–OH complexes. Electrochemical data showed a reversible one-electron redox couple at –1.47 V vs $[FeCp_2]^{+/0}$ that is assigned to the $Mn^{III/II}$–OH process (Figure 3.6A). This potential is similar to the one found in $[Mn^{III}H_3buea(OH)]^{-}$ that occurs at –1.50 V vs $[FeCp_2]^{+/0}$ and is assigned to the $Mn^{III/II}$ OH couple.[126] A second redox event was observed at a more positive potential that is center around – 0.25 V vs $[FeCp_2]^{+/0}$ and is

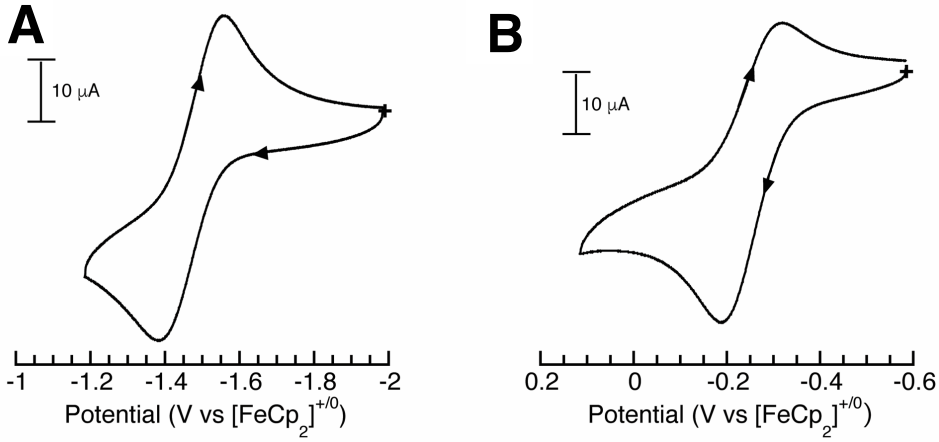

Figure 3.6 Cyclic voltammograms of $[Mn^{II}H_2pout(OH)]$ recorded in DMF: $Mn^{III/II}$ couple (**A**), $Mn^{IV/III}$ couple (**B**). Measurements were done at room temperature under Ar with a scan rate of 100 mV s^{-1}.

assigned to the $Mn^{IV/III}$–OH couple (Figure 3.6B). The process is not reversible under the experimental conditions, which we suggest is caused by the oxidized Mn^{IV}–OH species not being stable at room temperature. Again, a similar result was observed for the $Mn^{IV/III}$–OH couple (– 0.18 V vs $[FeCp_2]^{+/0}$) for $[Mn^{IV}H_3buea(OH)]$ at room temperature and subsequent studies found it was only stable at temperatures lower than – 50˚C.[120]

Accessing a Mn^{IV}–OH Species: Spectroscopic Studies. The electrochemical data of the Mn^{II}–OH complex suggested that accessing a higher valent Mn^{IV}–OH species should be possible with mild oxidants. We tested this premise by monitoring the formation of this complex at – 80˚C in 1:1 DMF:THF mixture using ferrocenium cation as the oxidant. Clean conversion was observed that initiated from $[Mn^{III}H_2pout(OH)]^-$ to produce a new spectrum with a prominent band at $\lambda_{max}(\varepsilon_M)$ = 460 nm (1390) and a shoulder at 560 nm; a single isosbestic point was found at 675 nm (Figure 3.4B). The final spectrum closely resembled that of $[Mn^{IV}H_3buea(OH)]$, which has an absorbance band λ_{max} (ε_M) = 466 nm (5600). This new oxidized species was stable for hours at – 80˚C.

EPR Studies. Previous studies from our group have shown that EPR spectroscopy is an effective method for probing changes in the electronic structure of monomeric Mn–O(H) complexes.[120] This approach utilized both perpendicular- and parallel-modes at X-band to follow spin state changes upon oxidation (Table 3.3). The EPR spectrum of $[Mn^{II}H_2pout(OH)]^{2-}$ (Figure 3.7) in perpendicular-mode showed signals over a wide magnetic field range. The spectra are complicated by resonances from multiple overlapping transitions, as has been described previously for $[Mn^{II}H_3buea(OH)]^{2-}$.[127] The simulation overlaid on the experimental spectrum in Figure 3.7 is for a $S = 5/2$ spin center using the parameters described in Table 3.3. The simulation intensity is in quantitative agreement

with the sample concentration determined from the weight of the complex dissolved in the solvent. The zero-field parameters are similar to the previously characterized $[Mn^{II}H_3buea(OH)]^{2-}$ and, as expected, $[Mn^{II}H_2pout(OH)]^{2-}$ showed a large rhombic parameter (E/D) owing to the unsymmetrical nature of the tripodal ligand.[127]

Table 3.3 EPR parameters of the $[Mn^nH_2pout(OH)]^m$ complexes

$[Mn^nH_2pout(OH)]^m$	*S*	D^a	*E/D*	g	$\|A\|^b$
Mn^{II}	5/2	-0.24	0.065	2.00, 2.00, 2.00	A_{iso} = 250
Mn^{III}	2	+1.7	0.04	–, –, 2.01	A_z = 270
Mn^{IV} (1)	3/2	+0.8	0.33	2.00, 2.01, 1.98	152, 198, 183
Mn^{IV} (2)	3/2	+0.7	0.17	2.06, 1.96, 2.02	224, 188, 201

$^a cm^{-1}$; ^{b}MHz

The addition of 1 equiv $[Fe^{III}Cp_2]^+$ resulted in the disappearance of the signals from the Mn^{II}–OH complex and the appearance of a 6-line hyperfine signal centered at g = 8 with A_z = 270 MHz (a = 9.6 mT) in parallel-mode (Figure 3.8). The simulation overlaid on the experimental spectrum are for an S = 2 spin center (Figure 3.8, Table 3.3) and its intensity is in quantitative agreement with the sample concentration. The zero-field parameters determined from the spectra are statistically the same as those of $[Mn^{III}H_3buea(OH)]^-$.[127] Taken together, these data are consistent with the formation of the high spin Mn^{III}–OH complex, $[Mn^{III}H_2pout(OH)]^-$.

The fully oxidized $[Mn^{IV}H_2pout(OH)]$ complex showed no features in parallel-mode, but perpendicular-mode signals were observed when measured at both S- and X-bands.

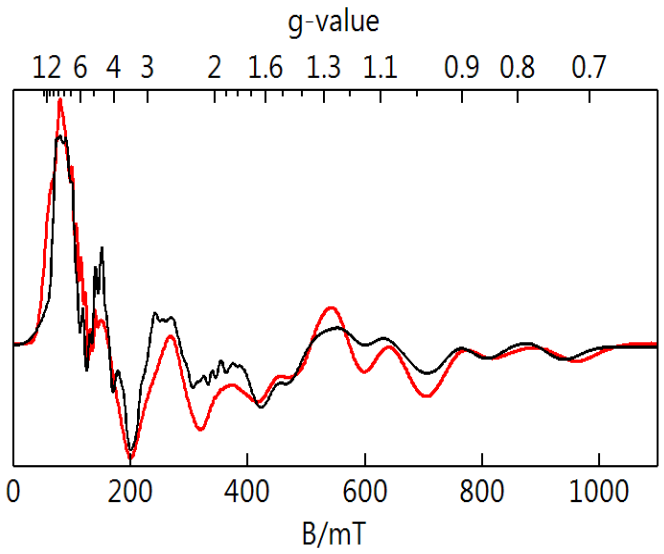

Figure 3.7 Perpendicular-mode EPR spectrum of a frozen solution of $[Mn^{II}H_2pout(OH)]^{2-}$ in 1:1 DMF:THF. Sample temperature 16 K, microwaves, 9.645 GHz, 0.2 mW. The black trace is a simulation for a S = 5/2 species.

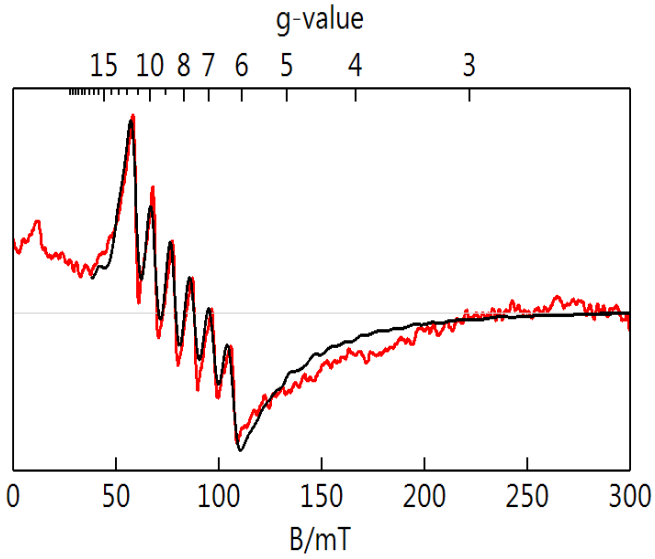

Figure 3.8 Parallel-mode EPR spectrum of a frozen solution of $[Mn^{III}H_2pout(OH)]^{-}$ in solvent 1:1 DMF:THF. Sample temperature 19 K, microwaves 9.318 GHz, 2 mW. The black trace is a simulation for a S = 2 species.

Figure 3.9 displays the spectra collected at both bands with the magnetic field ranges chosen to equate the g-value ranges for both frequencies. The positions of the resonances and the simulations are indicative of an $S = 3/2$ spin-state that is consistent with a high spin

Mn^{IV}–OH complex in local C_3 symmetry (Table 3.3). Our analysis of the EPR data showed that two distinct Mn^{IV}–OH species are formed, a result that is similar to what we reported for $[Mn^{IV}H_3buea(OH)]$.[120,127] The largest difference between the two species for $[Mn^{IV}H_2pout(OH)]$ is in their E/D values: species 1 (E/D = 0.33) is significantly more rhombic than species 2 (E/D = 0.17). The effective g-tensors for the |±1/2> and excited |±3/2> doublets for the two species are reported in Table 3.4 and indicated on Figure 3.9. For species 1, the effective g-tensors for each doublet are the same because of the large value of E/D. We have been successful in determining the hyperfine tensor for both species, even though the hyperfine splitting is not resolved in all directions. This determination was accomplished because we used two different frequencies in our analysis as previously described.[75]

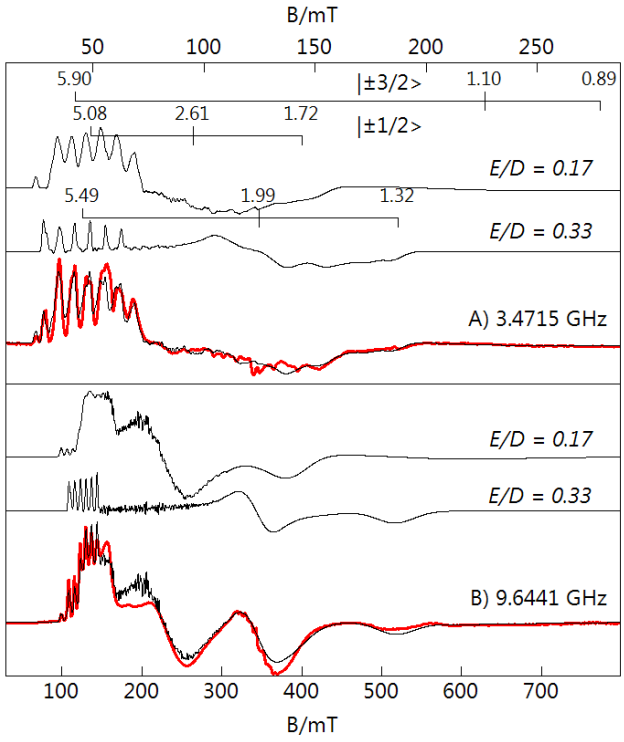

Figure 3.9 Perpendicular-mode EPR spectra of a 1:1 DMF:THF frozen solution $[Mn^{IV}H_2pout(OH)]$ at S-band (A) and X-band (B). Sample temperature was 5 K, microwave power was 0.03 mW for S-band and 0.2 mW for X-band. The black traces overlaid on the experimental spectra are the sum of the S = 3/2 simulations for the E/D = 0.17 and 0.33 species in a ratio of 70:30, respectively.

The rhombic character of the two species is consistent with a Mn^{IV} ion in a C_3 symmetry in which an appreciable Jahn-Teller distortion is expected. The reason(s) for the presence of two species and their exact structural differences are not known. The simulations showed that species 2 (the less rhombic species) was more abundant by a ratio of 2:1. Density functional theory (DFT) was used to probe the possible structures of [$Mn^{IV}H_2$pout(OH]]. The DFT calculations converged to two optimized structures shown in Figure 3.10 with selected bond lengths given in Table 3.4. Structure A had a lower energy and is similar to the structure of [$Mn^{III}H_2$pout(OH)]$^-$ with three intramolecular H-bonds involving the hydroxido ligand. Structure B has one urea arm rotated such that the carbonyl O-atom was proximal to the Mn–O(H) unit. A similar reorientation of a urea arm has been proposed for the protonated form of [$Fe^{IV}H_3$buea(O)]$^-$.[76] The computed equatorial Mn–N bond lengths were more similar for species A relative to those found for species B, which suggests A corresponds to the species with E/D values of 0.17. DFT calculations of the spin-dipolar A-tensors for the two species gave (29, -2, -27) MHz (A) and (30, 6, -36) MHz (B), which were in approximate agreement with the experimental values of (17, 3, -20) MHz for A and (26, -5, -21) MHz for B. Finally, we note that the EPR spectrum of the related complex [$Mn^{IV}H_3$buea(OH)]$^-$ also consisted of two species with similar values for *E/D* to that of [$Mn^{IV}H_2$pout(OH)]$^-$. One important difference between the two Mn^{IV}–OH complexes is that the more abundant species in [$Mn^{IV}H_3$buea(OH)]$^-$ is the one that is most rhombic (*E/D* = 0.33). The reason(s) for this difference is under investigation.

Table 3.4 DFT Computed Metrical Parameters for Proposed Structures of $[Mn^{IV}H_2pout(OH)]$.

Bond Distances (Å) or Angles (°)	A[a]	B[a]
Mn(1)-O(1)	1.80	1.78
Mn(1)-N(1)	2.15	2.11
Mn(1)-N(2)	1.91	1.92
Mn(1)-N(3)	1.93	2.01
Mn(1)-N(4)	1.96	1.91
O(1)…O(2)	2.58	2.59
O(1)…N(5)	2.73	4.36
O(1)…N(6)	2.76	2.70
O(1)-Mn(1)-N(1)	177	177
O(1)-Mn(1)-N(2)	97	97
O(1)-Mn(1)-N(3)	98	95
O(1)-Mn(1)-N(4)	96	98
N(1)-Mn(1)-N(4)	82	84
N(1)-Mn(1)-N(2)	83	84
N(2)-Mn(1)-N(4)	132	114
N(3)-Mn(1)-N(1)	84	82
N(3)-Mn(1)-N(2)	110	130
N(3)-Mn(1)-N(4)	114	112

[a]see Figure 3.10

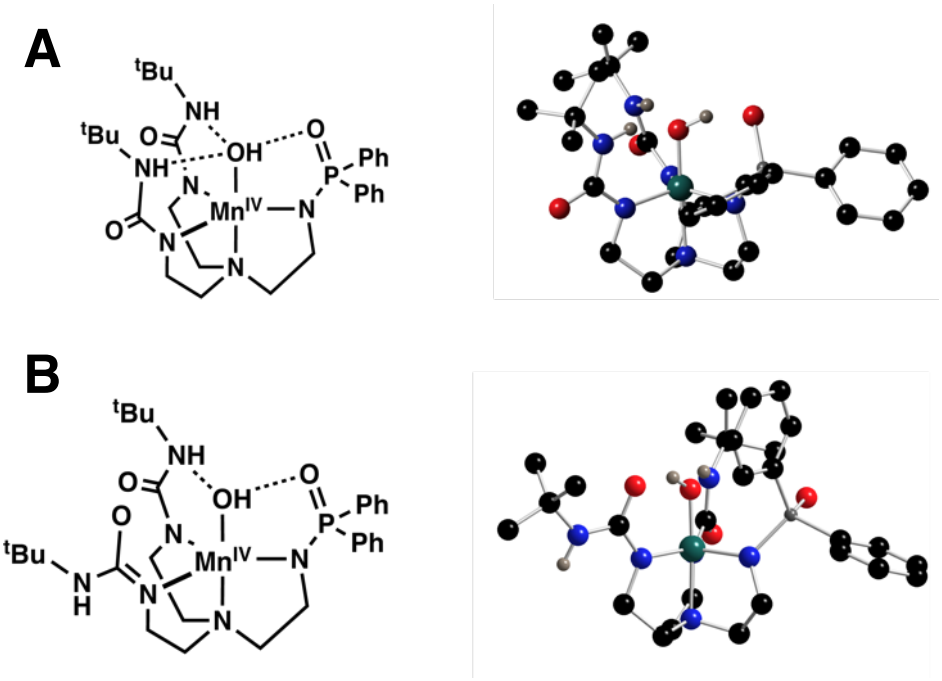

Figure 3.10 Possible structures for the two Mn^{IV}–OH complexes of $[Mn^{IV}H_2pout(OH)]$ determined from DFT. Only hydroxido/urea H-atoms shown for clarity.

Preparation and Properties of $[Mn^{III}H_2pout(O)]^{2-}$ and $[Mn^{IV}H_2pout(O)]^{-}$. The related $Mn^{III/IV}$–oxido complexes of $[H_2pout]^{3-}$ were also prepared in order to compare their spectroscopic properties to the related Mn–OH complexes. The synthesis of $[Mn^{III}H_2pout(O)]^{2-}$ was achieved via deprotonation of the Mn^{III}–OH complex with KO^{t}Bu (Scheme 3.2A). Conversion to its Mn^{IV}–oxido analog was accomplished using ferrocenium (Scheme 3.2B); $[Mn^{IV}H_2pout(O)]^{-}$ was also prepared via deprotonation of $[Mn^{IV}H_2pout(OH)]$ with KO^{t}Bu

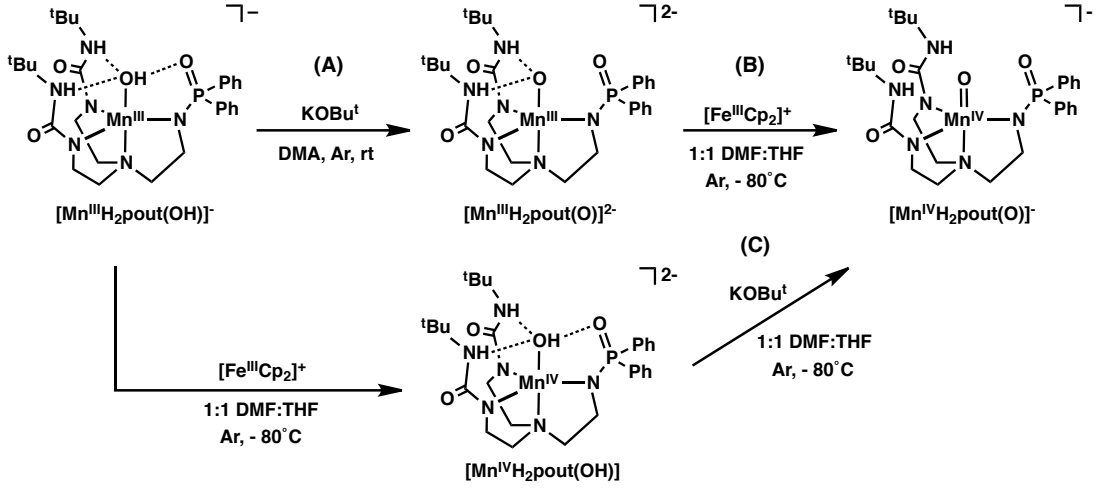

Scheme 3.2 Preparation of Mn–oxido complexes of $[H_2pout]^{3-}$.

(Scheme 3.2C). The electronic absorbance spectrum of $[Mn^{III}H_2pout(O)]^{2-}$ contains two major features in the visible region at $\lambda_{max}(\varepsilon_M)$ = 500 (400) and 760 (190) nm with an $\varepsilon_1/\varepsilon_2$ = 2.1 (Figure 3.11A). These values are reminiscent of those observed for $[Mn^{III}H_3buea(O)]^{2-}$ (see above). In addition, the parallel-mode EPR spectrum for $[Mn^{III}H_2pout(O)]^{2-}$ showed a six-lined signal at g = 7.91 with a hyperfine constant A_z = 290 MHz that consistent with a monomeric Mn^{III} complex having an S = 2 spin ground state (Figure 3.12A). Moreover, these values are distinct from those observed for $[Mn^{III}H_2pout(OH)]^{-}$. Similar differences were observed for $[Mn^{IV}H_2pout(O)]^{-}$ when compared to $[Mn^{IV}H_2pout(OH)]$: the Mn^{IV}–oxido

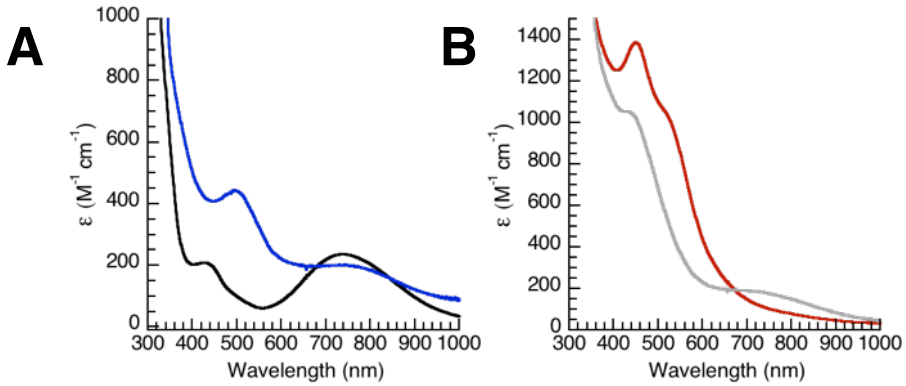

Figure 3.11 Overlaid UV-visible spectra of $[Mn^{III}H_2pout(OH)]^{2-}$ (black), $[Mn^{III}H_2pout(O)]^{2-}$ (blue) (**A**), $[Mn^{IV}H_2pout(OH)]^{-}$ (red) and $[Mn^{IV}H_2pout(O)]^{-}$ (gray) (**B**). Spectra were recorded in a 1:1 DMF:THF mixture at – 30 °C and – 80 °C, respectively.

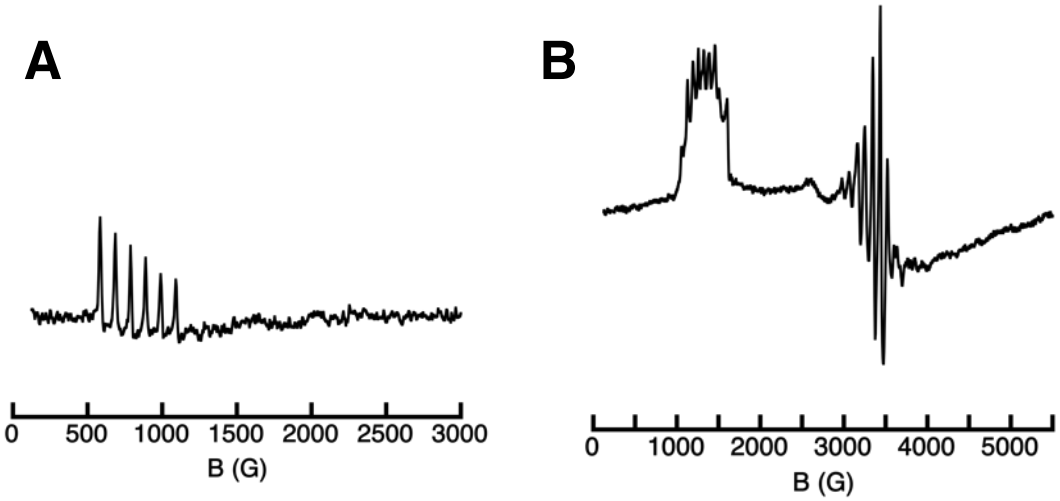

Figure 3.12 Parallel-mode EPR spectrum of a frozen solution of $[Mn^{III}H_2pout(O)]^{2-}$ (**A**) and perpendicular-mode EPR spectrum of a frozen solution $[Mn^{IV}H_2pout(O)]^{-}$ (**B**) in 1:1 DMF:THF. Sample temperature was 10 K.

complex had absorbance bands at $\lambda_{max}(\varepsilon_M)$ = 440 (1060) and 745 (200) nm (Figure 3.11B) that are similar to those found for $[Mn^{IV}H_3buea(O)]^-$. The perpendicular-mode EPR spectrum of $[Mn^{IV}H_2pout(O)]^-$ was broad and only the resonance at g = 5.09 could be identified (Figure 3.12B). The hyperfine pattern at g = 5.09 and the other broad features were different from that of $[Mn^{IV}H_2pout(OH)]$. Taken together, these findings demonstrate that the spectroscopic differences between Mn–hydroxido and Mn–oxido complexes with tripodal ligands can be used to differentiate these types of complexes in solution.

Preliminary Attempts to Access Mn^{V}–O(H) Species. Further analysis of the electrochemical properties of $[Mn^{II}H_2pout(OH)]^{2-}$ showed a third redox event at a positive potential that is + 620 mV vs $[FeCp_2]^{+/0}$ (Figure 3.13). Preliminary experiments to access the further oxidized species were performed by treating the $[Mn^{III}H_2pout(OH)]$ with 2 equiv of thianthrene radical ([Th][OTf]) (+ 0.680 V vs $[FeCp_2]^{+/0}$). The reaction to produce $[Mn^{IV}H_2pout(OH)]$ concomitantly generates an equiv of $FeCp_2$ that readily reacts with $[Th]^{\bullet+}$ complicating the ability to monitor the one-electron oxidation of Mn^{IV}–OH to the new species. Upon addition of 2 equivs of $[Th]^{\bullet+}$ to the Mn^{III}–OH produced a new spectrum with

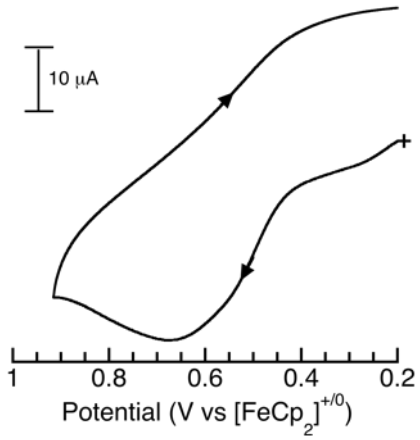

Figure 3.13 Cyclic voltammograms of $[Mn^{II}H_2pout(OH)]$ recorded in DMF: $Mn^{V/IV}$ couple. Measurements were done at room temperature under Ar with a scan rate of 100 mV s^{-1}.

a broad band about λ_{max} = 730 nm (Figure 3.14) and EPR data are needed to corroborate the oxidation state of the Mn ion.

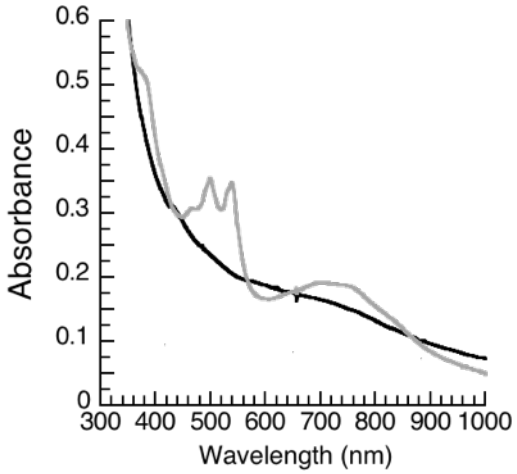

Figure 3.14 Overlaid UV-visible spectra of $[Mn^{III}H_2pout(OH)]^-$ 2 equivs of $[Th]^{\bullet+}$ (black), [and $[Mn^{III}H_2pout(OH)]^{2-}$ + xs KO^{t}Bu + 2 $[FcCp_2]^+$ (gray). Spectra were recorded in DCM and a 1:1 DMF:THF mixture, respectively, at – 80 °C.

Also interrogated was the possibility of accessing a Mn^V–O species. Generation of the reported $[Mn^VH_3buea(O)]$ was achieved by treatment of the corresponding $[Mn^{III}H_3buea(O)]^{2-}$ with two equivalents of oxidant, and in turn was the first reaction sequence attempted with the $[H_2pout]^{3-}$ complexes. Upon addition of two equivalents of $[FeCp_2]^+$ to the Mn^{III}–O compound showed growth of absorbance features λ_{max}/nm = 730, 540, 500, and 460 (Figure 3.14). These features are not consistent with previously reported $[Mn^VH_3buea(O)]$, which is reported to have optical features at λ_{max}/nm (ε_M/M^{-1} cm^{-1}) = 820 (3300), 320 (3400), and 430 (10000).[79] A possible problem with the reaction is the addition of base in order to generate the Mn^{III}–O complex *in situ*, which could be complicating the subsequent oxidation. Oxidation of the isolated Mn^{III}–O complex would allow for analysis if $^-$O^{t}Bu is causing any unproductive chemistry. Further investigation is needed to determine the identity of the newly generated species.

Preliminary Reactivity Studies with Ca^{2+} ions.

As mentioned in chapter 1, the presence of Ca^{2+} ions or other Lewis acids has been suggested to have an effect on the reactivity of high valent metal complexes. To analyze how [MnH_2pout] complexes may be affected by the presence of Lewis acids, initial studies were done with Ca^{2+} ions. Addition of Ca^{2+} ions (15c5Ca$(OTf)_2$) to a solution of [$Mn^{III}H_2$pout(OH)]$^-$ in a 1:1 DMF:THF mixture at – 30˚C resulted in shift in both absorbance features for [$Mn^{III}H_2$pout(OH)]$^-$ and the appearance of new absorbance features at λ_{max}/nm= 443, 310 and a shoulder at 810 (Figure 3.15). The energy of the absorbance features upon addition of Ca^{2+} ions are similar in energy to previously reported Ca–OH–Mn complexes from our group,[77] leading to the tentative assignment of this species to be [15c5Ca–OH–$Mn^{III}H_2$pout]$^+$. Deprotonation of the [15c5Ca–OH–$Mn^{III}H_2$pout]$^+$ species was

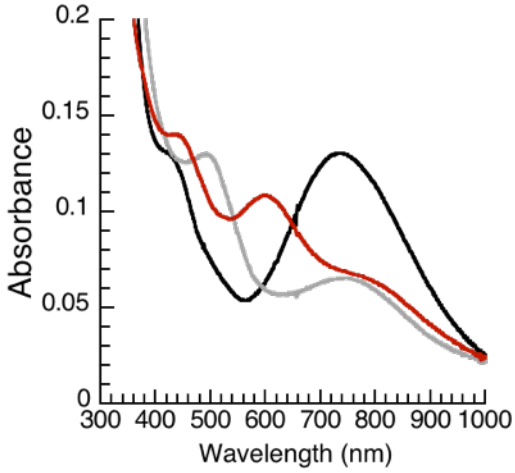

Figure 3.15 Overlaid UV-visible spectra of [$Mn^{III}H_2$pout(OH)]$^{2-}$ (black), [Ca-OH-$Mn^{III}H_2$pout]$^+$ (red), [Ca-O-$Mn^{III}H_2$pout] (gray). Spectra were recorded in a 1:1 DMF:THF mixture at – 30 °C.

performed with the addition of excess KO^{t}Bu (10 equivs) giving rise to new features in the absorbance spectrum at λ_{max}= 500 and 750 nm (Figure 3.15). To date, our lab has not been able to isolate an oxido bridged heterobimetallic species. Perhaps, the [H_2pout]$^{3-}$

framework would be able to better support such a structural motif given the ability for the two urea arms to support the oxido ligand with intramolecular H-bonds.

Addition of one equivalent of $FeCp_2^+$ results in the loss of the three bands attributed to the Ca adduct Mn^{III}–hydoxido species and subsequent growth of features at nearly identical energy as the band observed for the $[Mn^{IV}H_2pout(OH)]$ complex, suggesting that upon oxidation the interaction between the Mn complex and Ca ion was no longer present (Figure 3.16). Structural data from previously isolated heterobimetallic compounds consistently showed the Ca^{2+} ion interacting with two arms of the ligand framework, S=O units, as well as the hydroxido ligand—serving as a tridentate ligand to the Ca^{2+} ion. $[H_2pout]^{3-}$ may not provide an adequate binding site for the Ca^{2+} because it can only serve as a bidentate ligand (Figure 3.17). Additionally the two potential ligands (O–atoms from P=O and hydroxido) are presumably already involved in intramolecular H-bonds causing them to be weaker ligands to the Ca^{2+} ion.

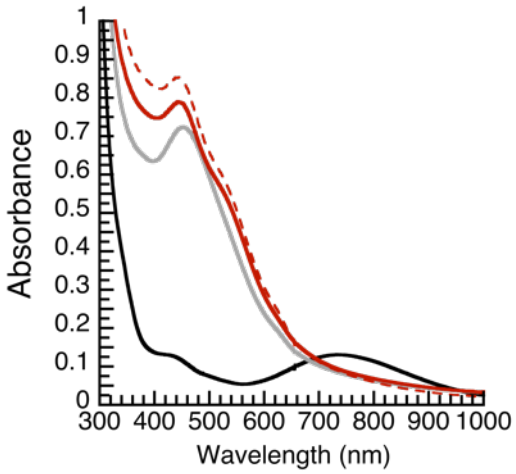

Figure 3.16 Overlaid UV-visible spectra of $[Mn^{III}H_2pout(OH)]^{2-}$ (black), $[Ca–OH–Mn^{III}H_2pout]^+ + Fc^+$ (red dashed), $[Mn^{IV}H_2pout(OH)]^{2-}$ (red solid) and $[Mn^{IV}H_2pout(OH)]$ + xs Ca^{2+} ions (gray). Spectra were recorded in a 1:1 DMF:THF mixture at – 80 °C.

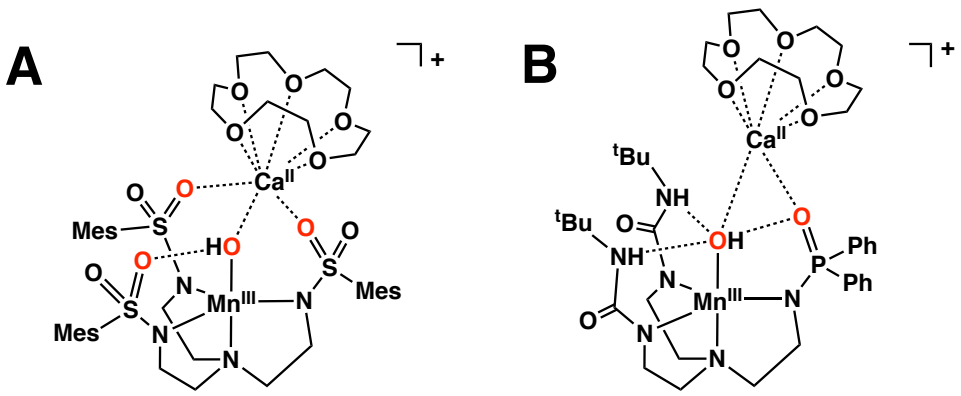

Figure 3.17 Chemdraw depiction of secondary metal binding site in $[MST]^{3-}$ (**A**) versus $[H_2pout]^{3-}$ (**B**).

To further test the hypothesis of whether the $[Mn^{IV}H_2pout(OH)]$ could support an interaction with Ca^{2+} ions, Ca^{2+} ions were directly added to the $[Mn^{IV}H_2pout(OH)]$ complex. Upon addition of 1 equiv of 15c5Ca$(OTf)_2$, no change was seen in the optical spectrum. Only after addition of an excess of 10 equivalents of Ca^{2+} ions was a new spectrum observed, which has a single absorbance feature at λ_{max}= 455 nm (Figure 3.16). These data support that there may not by a strong enough interaction between the Mn^{IV}–OH and Ca^{2+} ions, likely due to the lack of sufficient binding sites for the Ca^{2+} ion (Figure 3.17) as well as the absence of electrostatic interactions between the neutral complex and +2 cation. Perhaps $[H_2pout]^{3-}$ would more readily support a Ca^{2+}–O–Mn^{IV}: a monoanionic complex. Another way to circumvent the limitation of $[H_2pout]^{3-}$ could be to make a modification to the ligand and employ two phosphinic amides, one urea arm ($[Hput]^{3-}$, Figure 2.3B). $[Hput]^{3-}$ may allow for both a sufficient binding site for an auxiliary metal ion as well as maintain an intramolecular H-bond to support an oxido bridge heterobimetallic complex.

Summary and Conclusions

Manganese complexes with terminal hydroxido ligands are relatively rare because of the strong propensity of the Mn–OH units to aggregate to form multinuclear species;

however, they have been implicated as key intermediates in a variety of chemical processes,[82,120,124–126,128–135] most notably as intermediates formed during biological water oxidation.[110,136–140] Results from structural biology on the oxygen evolving complex (OEC) suggest that H-bonding networks to coordinate water molecules assist in forming Mn–OH complexes that can be in either the Mn^{III} or Mn^{IV} oxidation states.[20,141–144] One approach toward studying the structural outcomes of the secondary coordination sphere is to develop chelating ligands that can provide H-bond donors/accepts around the Mn–OH unit. Toward this goal, tripodal ligand $[H_2pout]^{3-}$ was designed to accommodate three intramolecular H-bonds to the hydroxido ligand. Spectroscopic and structural results on $[Mn^{II}H_2pout(OH)]^{2-}$ and $[Mn^{III}H_2pout(OH)]^{-}$ indicate that this type of H-bonding network was achieved and the O-atom of the phosphinic amide arm can serve as a H-bond acceptor. In addition, our electrochemical studies demonstrate that $[Mn^{III}H_2pout(OH)]^{-}$ can be converted to its Mn^{IV}–OH analog, which was achieved using the mild oxidant ferrocenium. The formation of $[Mn^{IV}H_2pout(OH)]$ was monitored spectrophotometrically and further characterized using variable frequency EPR spectroscopy that showed a high spin Mn^{IV} species is readily formed. These results illustrate the utility of this ligand design in forming mononuclear metal-hydroxido complexes that span a variety of different oxidation states.

Initial studies were also performed to assess to the possibility of accessing an Mn^{V} species as well as the interactions of the Mn complexes have with Ca^{2+} ions. Preliminary results suggests that the Mn^{III}–O(H) complexes react with 2 equivalents of oxidant to give new species; although, additional work is necessary to evaluate the identity of the species. Addition of Ca^{2+} ions to the Mn^{III}–OH complex generated an optical spectrum similar to the Ca^{2+}–OH–Mn^{III} heterobimetallic complexes previously prepared in our lab.[77] Deprotonation

of the Mn^{III}–OH Ca adduct was achieved with excess KOtBu, which is tentatively assigned as [15c5Ca–O–$Mn^{III}H_2$pout]. An oxido bridged heterobimetallic would be a new result and could be attributed to the capability of $[H_2pout]^{3-}$ to support the bridging oxido ligand with intramolecular H-bonds. Although results support that heterobimetallic species are generated at the +3 oxidation level, once oxidized the data suggest Ca^{2+} ion dissociates from the Mn complex.

Experimental Section.

General Procedures. All manipulations, unless otherwise stated, were completed under an argon atmosphere in a VAC drybox. Solvents were sparged with argon and dried over columns containing Q-5 and molecular sieves. All reagents were purchased from commercial suppliers and used as received unless otherwise noted. Potassium hydride as a 30% suspension in mineral oil was filtered and washed five times each with Et_2O and pentane and dried under vacuum. The ligand precursors 1,1′-(((2-aminoethyl)azanediyl)bis(ethane-2,1-diyl))bis(3-(*tert*-butyl)urea) and ferrocenium tetrafluoroborate were synthesized using literature procedures.[87,145]

Physical Methods. Electronic absorbance spectra were recorded in a 1 cm cuvette on an 8453 Agilent UV-vis spectrometer equipped with an Unisoku Unispeks cryostat. X-band (9.64 GHz) and S-band (3.50 GHz) EPR spectra were recorded on a Bruker spectrometer equipped with Oxford liquid helium cryostats. The quantification of all signals is relative to a CuEDTA spin standard. The concentration of the standard was derived from an atomic absorption standard (Aldrich). For all instruments, the microwave frequency was calibrated with a frequency counter and the magnetic field with an NMR gaussmeter. A modulation frequency of 100 kHz was used for all EPR spectra. The EPR simulation

software (*SpinCount*) was written by one of the authors.[146] EPR samples were prepared under an inert atmosphere, sealed with a septum, and cooled to 77K unless otherwise mentioned. ^{1}H and ^{13}C nuclear magnetic resonance (NMR) spectroscopies were conducted using a Bruker DRX500 spectrometer. Cyclic voltammetric experiments were conducted using a CHI600C electrochemical analyzer. A 2.0 mm glassy carbon electrode was used as the working electrode at scan velocities of 100 mV s^{-1}. A cobaltocenium/cobaltocene couple ($CoCp_2^{+}/CoCp_2$) (ΔEp = – 0.136 V vs $Fc^{+/0}$) was used to monitor the Ag wire reference electrode, and all potentials are reference to the $Fc^{+/0}$ couple. The DFT calculations were performed with Gaussian '09[147] using the hybrid functional B3LYP and the basis set 6-311G. Geometry optimizations were performed using the structures determined from X-ray diffraction for the Mn^{II} and Mn^{III} complexes. The calculations for the manganese(IV) complex were based on the crystal structure of the Mn^{III} complex.

X-ray Crystallographic Methods. A Bruker SMART APEX II diffractometer was used to collect all data. The APEX2[148] program package was used to determine the unit-cell parameters and for data collections. The raw frame data was processed using SAINT[149] and SADABS[150] to yield the reflection data files. Subsequent calculations were carried out using the SHELXTL[150] program. The structures were solved by direct methods and refined on F2 by full-matrix least-squares techniques.

Hydrogen atoms for $K_2[Mn^{II}H_2pout(OH)]$ H1, H5, and H6 were located from a difference-Fourier map and refined (x,y,z and U_{iso}). The remaining hydrogen atoms were included using a riding model. Disordered atoms were included using multiple components with partial site-occupancy-factors. The structure is polymeric.

The hydrogen atom on O1 for K[$Mn^{III}H_2$pout(OH)] was located from a difference-Fourier map and refined (x,y,z and U_{iso}). The remaining hydrogen atoms were included using a riding model. There is one-half molecule of diethylether solvent present per formula-unit. The solvent was disordered and included using multiple components with partial site-occupancy-factors. The structure is polymeric.

Preparative Methods. H_5pout. The preparative route for this compound followed the method previous report for H_22^{Tol} in which only the last step was different.[88] Details in chapter 2.

$K_2[Mn^{II}H_2pout(OH)]$ A solution of H_5pout (0.100 g, 0.183 mmol) in anhydrous DMA (4 mL) was treated with potassium hydride (KH) (0.030 g, 0.75 mmol) and the reaction allowed to proceed until gas evolution ceased and all solids were dissolved. To the colorless solution was added $Mn^{II}(OAc)_2$ (0.031 g, 0.18 mmol). After stirring for 90 min, water (3 μL, 0.2 mmol) was added via syringe and the reaction mixture was filtered after 15 min through a medium porosity glass-fritted funnel to afford a light-yellow filtrate and white solid on the glass frit (KOAc, 90%). Et_2O was allowed to diffuse into DMA resulting in pale yellow crystals (80%) suitable for XRD studies. Anal. Calcd for K_2[MnH_2pout(OH)], $C_{28}H_{43}K_2MnN_6O_4P$: C, 48.61; H, 6.27; N, 12.15. Found C, 48.79; H, 6.91; N, 12.48. FTIR (ATR, cm^{-1}) 3656, 3261, 3124, 3071, 2955, 2797, 1645, 1585, 1510, 1435, 1390, 1350, 1310, 1245, 1205, 1185, 1115, 1045, 1015, 975, 885, 815, 755, 710, 630. UV-vis (DMF:THF, λmax nm, (ε_{max}, M^{-1} cm^{-1})) 525 (sh). EPR (X-band Perpendicular, DMF:THF, 16 K, g = 6.0, 3.9, 2.4, 1.6, 1.4, 1.3, A_{iso} = 250). $E_{1/2}$ (DMF, V vs $[FeCp_2]^{+/-}$): $Mn^{III/II}$ = –1.47.

K[$Mn^{III}H_2$pout(OH)] was prepared by a similar method to K_2[$Mn^{II}H_2$pout(OH)] with the following modifications: after the addition of water, half an equivalent of elemental I_2 (0.028 g, 0.11 mmol) was added to the yellow filtrate that caused an immediately color

change to dark green. The solution was left to stir for 30 min and then concentrated to dryness under reduced pressure. The residue was titrated with Et_2O (20 mL) and again dried under vacuum. The free-flowing green solid was redissolved in MeCN and filtered through a fine porous-glass frit to remove a white solid (KI, 27 mg, 90%). Single crystals suitable for XRD studies were obtained by vapor diffusion of Et_2O into the solution of DMA of the salt (60%). Anal. Calcd for $K_2[MnH_2pout(OH)]$, $C_{28}H_{43}KMnN_6O_4P \bullet 0.5KI \bullet DMA$: C, 46.71; H, 6.37; N, 11.92. Found C, 46.74; H, 6.38; N, 11.28. FTIR (ATR, cm^{-1}) 3300, 3274, 3211, 2956, 2875, 2810, 1610, 1567, 1500, 1490, 1462, 1450, 1433, 1420, 1399, 1378, 1369, 1238, 1112, 1006, 1020, 978, 790, 743, 724, 696, 661, 616, 594. UV-vis (DMF:THF, λ_{max} nm, (ε_{max}, M^{-1} cm^{-1})) 440 (210), 740 (236). EPR (X-band Perpendicular, DMF:THF, 19 K, g = 8, A_z = 270) E_0 (DMF, V vs $[FeCp_2]^{+/-}$): $Mn^{IV/III}$ = – 0.25.

Oxidation of $[Mn^{III}H_2pout(OH)]^-$. A 20 mM stock solution of $K[MnH_2pout(OH)]$ was prepared in a 1:1 DMF:THF mixture at room temperature and kept in a -35 °C freezer for the duration of the experiment. Addition, via air tight syringe, of a 40 μL aliquot of stock metal complex to the solvent mixture (2 mL) in a 1 cm quartz cuvette, which was sealed with a rubber septum and precooled to the desired temperature in the 8453 Agilent UV–vis spectrophotometer equipped with an Unisoku Unispeks cryostat, to give the desired concentration for oxidation experiments (400 μM). The solution of metal complex was allowed to equilibrate to the desired temperature for at least 15 min. Additionally, a stock solution of $[FeCp_2]BF_4$ (40 mM) was prepared in 1:1 DMF:THF mixture and kept in a -35 °C freezer for the duration of the experiment. One equiv (20 μL) of $[FeCp_2]BF_4$ was added to the Mn^{III}–OH solution via gastight syringe. The disappearance of the two low-energy d-d transitions corresponding to the Mn^{III}–OH species were monitored spectrophotometrically,

with the appearance of new transitions attributed to the Mn^{IV}–OH species. EPR samples were prepared in a similar manner and frozen via submersion into liquid N_2. The sign of D for Mn(II)–OH and Mn(IV)–OH were determined from simulations of perpendicular-mode EPR spectra collected at variable temperatures.

Preparation of Low-Temperature $[Mn^{III}H_2pout(O)]^{2-}$ EPR Samples. A solution of $[Mn^{III}H_2pout(OH)]^-$ (~15 mM, 250 μL) in a DMF:THF mixture was transferred to an EPR tube and sealed with a rubber septum. The tube was brought out of the dry box and placed in a – 30 °C acetonitrile/dry ice bath and allowed to equilibrate for fifteen minutes. A 0.5 M (0.028 g, 0.25 mmol) stock solution of KO^tBu was prepared in a DMF:THF mixture and one equiv (8 μL) was added via a syringe. After mixing by careful shaking of the tube, the EPR tube was quickly removed from the cold bath, wiped clean of acetonitrile, and frozen in liquid nitrogen before analysis.

Preparation of Low-Temperature $[Mn^{IV}H_2pout(O)]^-$ EPR Samples. Samples were prepared in an analogous manner as described above with the following modifications: subsequent addition of one equivalent of $FcBF_4$ (18 μL of a 220 mM stock solution). Sample was prepared in a – 80 °C acetone/dry ice bath.

Generation of $[Mn^{III}H_2pout(O)]^{2-}$at Low Temperature using UV-vis Spectroscopy. For a typical experiment, a stock solution of $[Mn^{III}H_2pout(OH)]^-$ at 20 mM concentration (0.013 g, 0.020 mmol) was prepared in a DMF:THF mixture (1 mL) and stored at −35 °C. To a 1 cm cuvette was added 2 mL of DMF:THF mixture and 40 μL of metal complex solution giving the desired experiment concentration (400 μM). The cuvette was sealed with a rubber septum then transferred to the precooled UV-vis spectrometer cryostat and allowed to equilibrate for at least 15 minutes at – 30 °C under a flow of argon gas. A 45 mM (0.010 g, 0.089 mmol)

stock solution of KO^{t}Bu was prepared in 1 mL of a DMF:THF mixture and one equiv (18 µL) was added via a syringe and the progress of the reaction monitored optically.

Generation of [Mn^{IV}H$_2$pout(O)]$^-$ at Low Temperature using UV-vis Spectroscopy. Experiments were performed in an analogous manner as described above with the following modifications: subsequent addition of one equivalent (20 µL) of a 40 mM $FcBF_4$ (0.011 g, 0.040 mmol) stock in 1 mL of DMF:THF mixture at – 80 ºC.

Generation of Ca^{2+} adducts at Low Temperature using UV-vis Spectroscopy. Experiments were performed in an analogous manner as described above with the following modifications: subsequent addition of 1-10 equivalents of a 40 mM 15c5[$Ca(OTf)_2$] (0.022 g, 0.039 mmol) stock in 1 mL of DMF:THF mixture at – 80 ºC.

CHAPTER 4

Preparation and Characterization of a Monomeric Fe-hydroxido Complexes

Chapter 1 introduced a common reactivity pathway suggested for metalloenzymes that bind and activate dioxygen. The mechanism implicates that oxidation of substrates proceeds through homolytic cleavage of the C–H bond via a metal-O_2 derived intermediate. As previously mentioned, Green successfully trapped Compound I in P450s and provided substantial spectroscopic and kinetic evidence to confirm that Compound I is in fact a high valent Fe^{IV}–oxido/porphyrin radical.[17,151] Fe^{IV}–oxido species have also been identified in non-heme systems as intermediates responsible for enzymatic activity. For example, the groups of Bollinger/Krebs[19,152–157] and Hausinger[158,159] identified such species in as the oxidative intermediate in a-ketoglutarate-dependent monooxygenases. All these high valent Fe–oxido intermediates are often suggested to react with substrate to form Fe–hydroxido species. For example, in Rieske proteins, another non-heme oxygenase, an Fe^{V}–oxido/hydroxido species is proposed to be responsible for initial substrate activation, which is then suggested proceeds to an Fe^{IV}–OH species and substrate radical (Figure 4.1).[160,161]

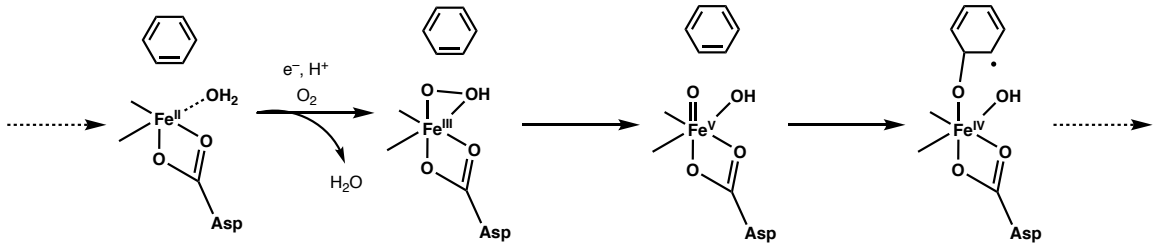

Figure 4.1 One proposed route of Rieske dioxygenases. (Partial mechanism)

While there have been several reports of synthetic Fe^{IV}–oxido complexes[38,40,41,162–181], generation of an analogous Fe^{IV}—hydroxido species poses a major obstacle due to the redox potential of high valent metal–oxido species and the acidity of the hydroxido ligand,

which are estimated to be less than 5 pK_a units. In a recent report from the Goldberg lab,[182] an Fe–OH species had been generated with the oxidative competence to perform chemistry similar to that of Compound II (Scheme 4.1); however, the identity of the Fe–OH complex as a true Fe^{IV} species or an Fe^{III} species with an oxidative equivalent delocalized about the corrole ligand is still unclear.

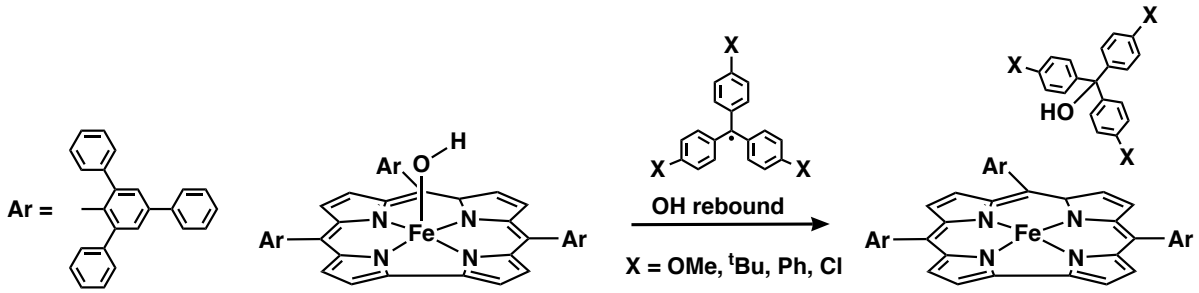

Scheme 4.1 Oxygen rebound reactivity of a proposed Fe^{IV}–OH complex generated analyzed by Goldberg and coworkers.

One key structural component essential in many protein active sites, but lacking in most synthetic systems, are intramolecular H-bonding interactions to help regulate proton and electron movement to and from the metal center. The work in this chapter extends the employment of the hybrid ligand scaffold, $[H_2pout]^{3-}$, designed to form an "ideal" H-bonding cavity to stabilize a M–OH unit. A series of Fe–hydroxido complexes have been prepared, including the possible generation of an authentic Fe^{IV}–hydroxido synthetic complex.

Results and Discussion

Synthesis. The preparation of H_5pout was detailed in Chapter 2 and 3.

The synthesis of $Fe^{II/III}$–OH complexes were accomplished in an analogous manner to the Mn–OH series in Chapter 3 and are outlined in Scheme 4.2. The ligand precursor was deprotonated with KH and subsequently metallated with $Fe^{II}(OAc)_2$. The hydroxido ligand was derived from water; an extra equivalent of base was added to the reaction mixture in

order to produce the hydroxido ligand. Successive treatment of the Fe^{II}–OH complex with half an equivalent of elemental iodine gave the corresponding Fe^{III}–OH complex (Scheme 4.2).

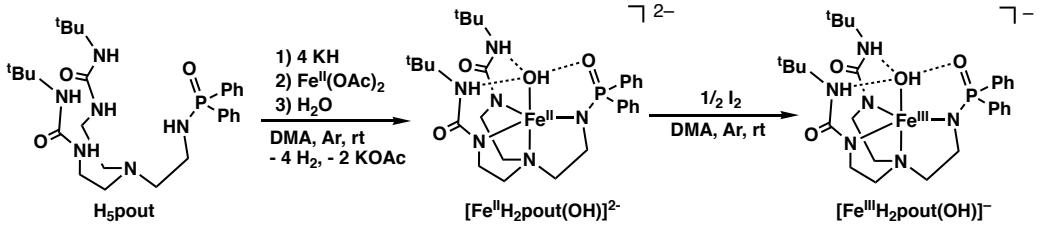

Scheme 4.2 Preparation of Fe–OH complexes.

Structural Properties. The molecular structures of the hybrid Fe^{II}–OH and Fe^{III}–OH complexes were characterized with X-ray diffraction methods (Figure 4.2, Table 4.1 and 4.2). The structures for both salts revealed that each Fe–OH anion is mononuclear with a distorted tbp coordination geometry. The primary coordination spheres around the Fe center in each complex is composed of a N_4O donor set with three anionic N-atom donors forming the trigonal plane. The axial positions contain the apical amine N1-atom from the $[H_2pout]^{3-}$ ligand and O1-atom from the hydroxido ligand. Comparison of Fe–O1 bond lengths between the two structures, there is a significant decrease in length from 2.052(1) Å to 1.893(2) Å in the Fe^{II}–OH and Fe^{III}–OH, respectively, which is consistent with oxidation of the metal center.

Comparison of features in the secondary coordination sphere show similar results as described in the Mn system of Chapter 3. Both structures illustrate H-bonds between the urea NH groups to the hydroxido ligand as evaluated by the average N···O distances of 2.842(X) Å in $[Fe^{II}H_2pout(OH)]^{2-}$ and 2.776(3) Å in $[Fe^{III}H_2pout(OH)]^{-}$. In the Fe^{III}–OH there is a third intramolecular H-bond that is formed between the hydroxido ligand and the O2-atom of the phosphinic group (O1···O2 of 2.694(3) Å). The presence of the three

intramolecular H-bonds illustrates the successful design concept by which this ligand was developed. Moreover, there is contraction of the Fe^{III}–OH bond to 1.893(2) Å in $[Fe^{III}H_2pout(OH)]^-$ compared to the Fe^{III}–OH bond length of 1.926(2) Å in $[Fe^{III}H_3buea(OH)]^-$.[124] A similar argument cannot be made in $[Fe^{II}H_2pout(OH)]^{2-}$, because

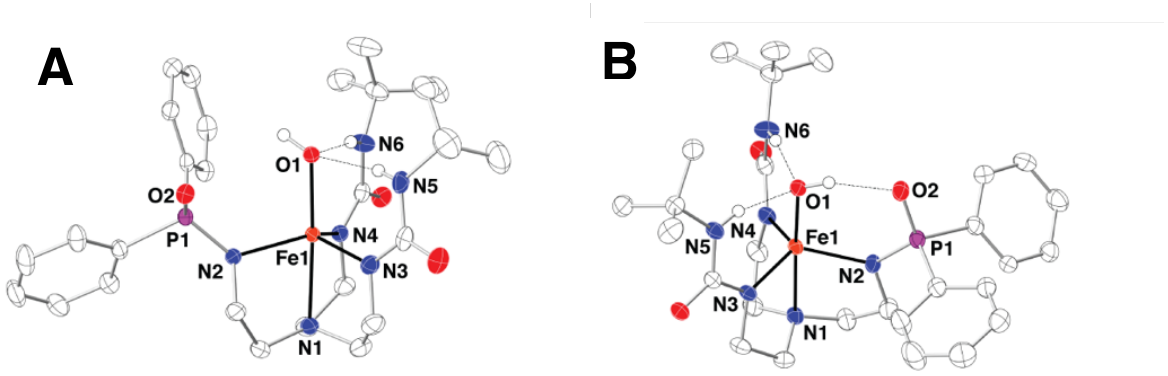

Figure 4.2 Thermal ellipsoid plots of $[Fe^{II}H_2pout(OH)]^{2-}$ (**A**), $[Fe^{III}H_2pout(OH)]^-$ (**B**). Thermal ellipsods are drawn at the 50% probability level, only urea and hyrdoxido hydrogen atoms are shown for clarity.

Table 4.1 Crystallographic Data and Structure Refinement Parameters

Complex	$K_2[Fe^{II}H_2POUT(OH)]$	$K[Fe^{III}H_2POUT(OH)]$
Empirical Formula	$C_{36}H_{61}FeK_2N_8O_6P$	$C_{30}H_{46}FeKN_7O_4P$
Formula weight	866.94	694.66
Crystal system	Orthorhombic	Triclinic
Space group	*Pbca*	$P\bar{1}$
a (Å)	17.158(2)	12.0041(8)
b (Å)	21.630(3)	12.4628(9)
c (Å)	24.678(3)	14.8605(10)
α (°)	90	74.7723(9)
β (°)	90	66.4482(8)
χ (°)	90	85.2450(9)
Volume ($Å^3$)	9158.6(19)	1965.8(2)
Z	8	2
δcalc (Mg/m3)	1.257	1.174
GOF	1.029	1.032
R1	0.0405	0.0497
wR2	0.1020	0.1454
CCDC Code		1860166

the potassium ion interacts with the hydroxide ligand, a structural element also seen in the molecular $K_2[Mn^{II}H_2pout(OH)]$.[183]

Table 4.2 Selected Bond Distances and Angles for $K_x[Fe^nH_2pout(OH)]$

Bond Distances (Å) or Angles (°)	$K_2[Fe^{II}H_2pout(OH)]$	$K[Fe^{III}H_2pout(OH)]$
Fe1–O1	2.052(1)	1.893(2)
Fe1–N1	2.309(2)	2.206(2)
Fe1–N2	2.120(2)	2.046(2)
Fe1–N3	2.060(2)	2.014(2)
Fe1–N4	2.113(2)	2.012(2)
O1···O2	N/A	2.694(3)
O1···N5	2.920(X)	2.777(3)
O1···N6	2.783(X)	2.772(3)
O1–Fe1–N1	174.81(6)	178.30(8)
O1–Fe1–N2	98.65(6)	99.30(8)
O1–Fe1–N3	105.38(6)	100.75(8)
O1–Fe1–N4	99.37(7)	101.02(8)
N1–Fe1–N4	79.25(7)	80.08(8)
N1–Fe1–N2	77.24(6)	79.05(8)
N2–Fe1–N4	109.54(7)	114.56(9)
N3–Fe1–N1	79.70(7)	79.82(8)
N3–Fe1–N2	125.32(7)	119.16(9)
N3–Fe1–N4	113.77(7)	116.79(9)

Vibrational Properties. Analysis of vibrational properties using FTIR spectroscopy showed bands attributed to the ν(FeO–H) at 3650 and 3600 cm^{-1} for the Fe^{II}–OH and Fe^{III}–OH complexes, respectively (Figure 4.3). Similar to the $[Mn^{II}H_2pout(OH)]^{2-}$ systems, comparison of $[Fe^{II}H_2pout(OH)]^{2-}$ with other Fe^{II}–OH complexes is complicated due to the interactions of the complexes with the potassium counter ion. Comparisons can be made at the Fe^{III} level: $[Fe^{III}H_2pout(OH)]^-$ has a ν(FeO–H) at lower energy than the comparable peak for $[Fe^{III}H_3buea(OH)]^-$, which was found at 3630 cm^{-1}.[124] The lower O–H bond vibration is consistent with presence of an additional intramolecular H-bond between the phosphinic arm and the hydroxido ligand (O–H···O=P) causing a weakened O–H bond.

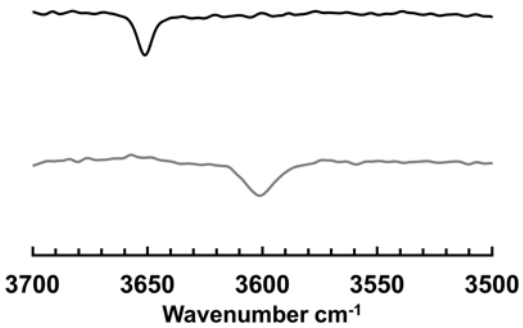

Figure 4.3 AT-FTIR spectra for $[Fe^{II}H_2pout(OH)]^{2-}$ (black), $[Fe^{III}H_2pout(OH)]^{-}$ (gray).

To further evaluate the effects of the H-bonding network on the properties of the Fe–OH unit, we collaborated with the Hendrich and Guo Labs at Carnegie Mellon University to employ nuclear resonance vibration spectroscopy (NRVS), which is a technique that allows us to probe the vibrations associated with ligands directly bound to the Fe center. Using a series of Fe^{III}–O(H) complexes from our group in different ligand frameworks (prepared in collaboration with Dr. Ethan Hill), we were able to draw a correlation between the ν(Fe–O) and H-bonding about the Fe–O(H) unit (Figure 4.4). These effects are illustrated for four Fe^{III}–O(H) complexes: three of the complexes contain Fe^{III}–OH units and one contains a pure Fe^{III}–O unit. As expected, the oxido complex has the strongest Fe–O

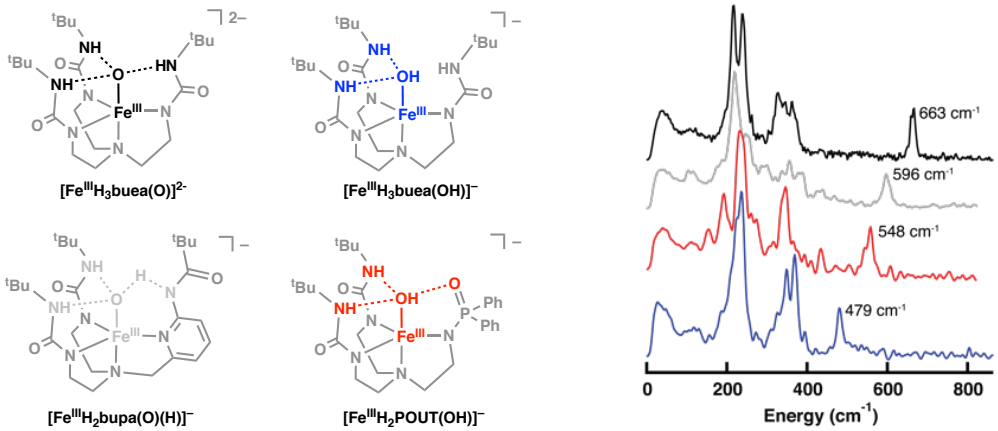

Figure 4.4 NRVS spectra for $[Fe^{III}H_3buea(O)]^{2-}$ (black), $[Fe^{III}H_2bupa(OH)]^{-}$ (gray), $[Fe^{III}H_2pout(OH)]^{-}$ (red), and $[Fe^{III}H_3buea(OH)]^{-}$ (blue). The peaks for the Fe–O vibrations are labelled with their corresponding energies.

bond with a ν(Fe–O) = 663 cm^{-1}. The other three Fe^{III}–OH complexes have various H-bonding interactions to the hydroxido ligand. As the H-bonding interactions becomes stronger, the Fe–O vibration also becomes stronger. These vibrational data demonstrate that a M–OH unit can be tuned through H-bonds and in turn have direct effects on the physical properties of the complexes.

Electrochemical Properties. Cyclic voltammetry was employed to analyze the redox properties of the Fe–OH complexes. Electrochemical data showed a reversible one-electron redox couple at –1.38 V vs $[FeCp_2]^{+/0}$ that is assigned to the $Fe^{III/II}$–OH process (Figure 4.5). The potential of the $Fe^{III/II}$ couple is approximately 500 mV more positive than the one found in $[Fe^{III}H_3buea(OH)]^-$ that occurs at –1.79 V vs $[FeCp_2]^{+/0}$.[126]

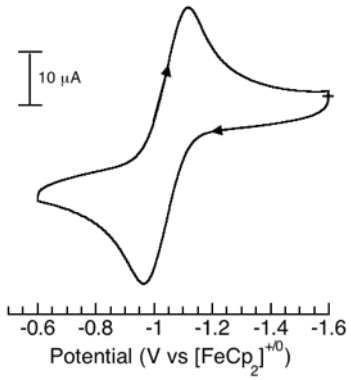

Figure 4.5 Cyclic voltammograms of $[Fe^{II}H_2pout(OH)]$ recorded in DMF: $Fe^{III/II}$ couple. Measurement were done at room temperature under Ar with a scan rate of 100 mV s^{-1}.

Accessing an Fe^{IV}–OH Species at Low Temperatures: Spectroscopic Studies.

Electronic Absorbance Properties. The conversion of $[Fe^{III}H_2pout(OH)]^-$ to $[Fe^{IV}H_2pout(O)(H)]$ was monitored optically in 1:1 DMF:THF at – 80˚C with the addition of 18-crown-6 ether (18c6) to help solubilize the compound. The Fe^{III}–OH species has a feature in the visible region at $\lambda_{max}(\varepsilon_M)$ = 400 (3230) (Figure 4.6A, black spectrum)

consistent with the spectrum that was previously reported for the $[Fe^{III}H_3buea(OH)]^-$ complex.[184] Upon oxidation with one equivalent of ferrocenium salt ($FcBF_4$) (Scheme 4.3), the strong 400 nm band is no longer well defined with an increase in intensity that makes it

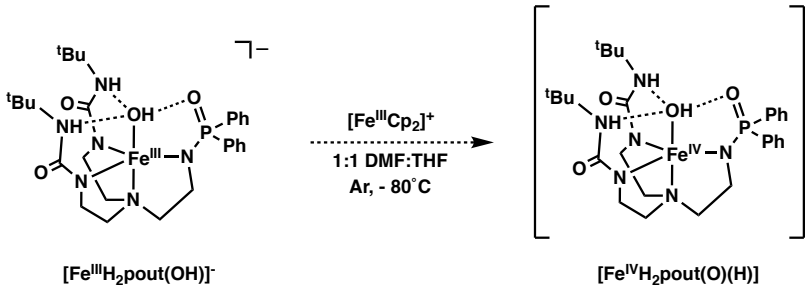

Scheme 4.3 Oxidation of Fe^{III}–OH complex.

difficult to assign a wavelength of the peaks. There is an additional low-energy feature at λ_{max} = 700 nm that grows in upon oxidation (Figure 4.5, red spectrum). The spectrum of the oxidized species is different from those of our other Fe^{IV} complexes. The 700 nm feature is higher in energy and distinct in shape when compared to the well characterized oxido complex, which has an absorption band at λ_{max} = 808 nm; an absorbance that is a trademark feature within nearly all non-heme Fe^{IV}–oxido complexes.[38,46,171]

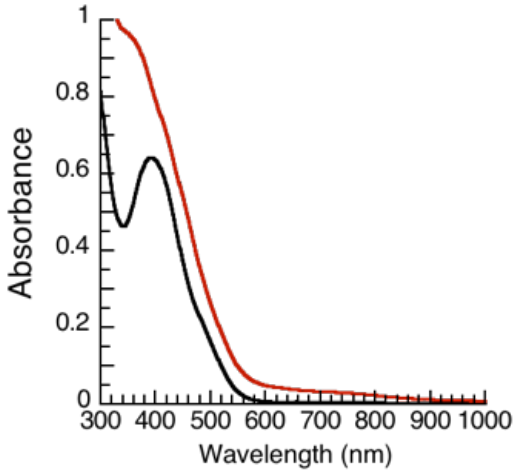

Figure 4.6 UV-visible spectra of $[Fe^{III}H_2pout(OH)]^-$ (black) and $[Fe^{IV}H_2pout(O)(H)]$ (red).

EPR Studies. These magnetic studies led us to consider changes in the zero field splitting parameters (ZFS): D and E are energy terms that describe the extent of ZFS splitting in the axial (D) or equatorial (referred to as rhombic) (E) directions. A positive D parameter implicates compression along one axis, while a negative D term indicates elongation in a single direction. Differences in the D term could reflect the difference in an axial ligand, e.g. $^{-}$OH vs O^{2-}. Electronic parameters for the [FeH_2pout(OH)] series are found in Table 4.3. The low valent Fe^{II}–OH has a clean signal at g = 8.47 in the parallel-mode X-band EPR spectrum, consistent with an high spin Fe^{II} center (Figure 4.7A). In perpendicular-mode, the isolated Fe^{III}–OH complex has a rhombic spectrum typical of high spin Fe^{III} system in an asymmetrical trigonal field (Figure 4.7B). The E/D value for $[Fe^{III}H_2pout(OH)]^-$ is ~ 0.15, which is similar to the E/D value of 0.157 found in $[Fe^{III}H_3buea(OH)]^-$.[180]

Upon oxidation, a new axial feature appears near g = 8 in parallel-mode that is characteristic of an Fe^{IV}, S=2 species (Figure 4.7C). Initial studies estimated the E/D for the

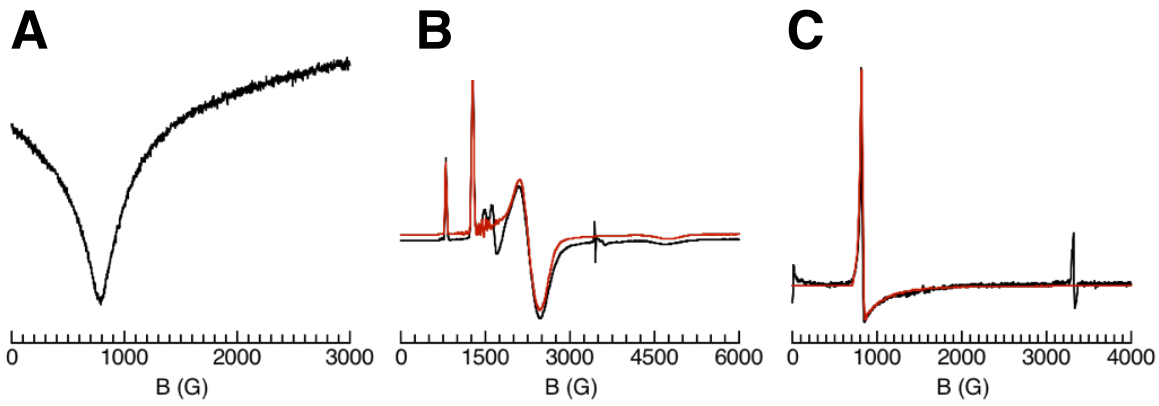

Figure 4.7 Parallel-/Perpendicular-mode EPR spectra of $[Fe^{II}H_2pout(OH)]$ (**A**); $[Fe^{III}H_2pout(OH)]^-$ (**B**); and $[Fe^{IV}H_2pout(O)(H)]$ (**C**) in 1:1 DMF:THF. Sample temperature 10 K. The red traces are simulations of S = 5/2 and S = 2 species, in **B** and **C**, respectively.

new Fe^{IV} complex to be ~0.07, which is consistent with the previously reported $[Fe^{IV}H_3buea(O)]^-$ complex with an E/D = 0.03.[180,184] One important distinction between the

[$Fe^{IV}H_2$pout(O)(H)] species and all known Fe^{IV}–oxido[19,40,176] complexes is that the measured D value is negative. [$Fe^{IV}H_2$pout(O)(H)] was fit with D = – 2 cm^{-1}; whereas, [$Fe^{IV}H_3$buea(O)]$^-$ has an associated D value of + 4.7 cm^{-1}.[180,184] As mentioned above, a negative D parameter suggests lengthening in one direction of the complex, which correlates with protonation of an oxido unit. Protonation of the exogenous oxido ligand would cause a lengthening in the Fe–O bond and a decrease in the D parameter.

Table 4.3 EPR and Mössbauer parameters of the [Fe^nH_2pout(OH)]^m complexes

[Fe^nH_2pout(OH)]^m	*S*	*D*[a]	*E/D*	g	$\delta^b E_Q{}^b$
Fe^{II}	2	N/A	N/A	8.47	1.05, 3.24
Fe^{III}	5/2	-2	0.15	8.53, 5.38, 3.02, 1.46	0.35, 0.40
Fe^{IV}	2	-2	0.07	8	0.05, 0.37

[a]cm^{-1}; [b]mm/s

Upon comparison of reported M–O/OH complex pairs, the trend of decreasing value of D is apparent when the complex is protonated. For example, [$Fe^{III}H_3$buea(O)]$^{2-}$ has a D value of – 0.7 cm^{-1} and upon protonation, the complex's D parameter drops to – 2.4 cm^{-1}.[180] A similar trend is observed in [$Mn^{III}H_3$buea(O/OH)]^n with D parameter dropping from +2.0 cm^{-1} in the oxido species to +1.75 cm^{-1} in the hydroxido complex.[75,127] The trend holds in higher valent species as well, for [$Mn^{IV}H_3$buea(O/OH)]^n, the Mn^{IV}–O has a D value of +2.5(2) cm^{-1} that decreases to +0.67(5) and +0.88(5) cm^{-1} in the two Mn^{IV}–OH species.[75,127]

Mössbauer Studies. The generation of an Fe^{IV} center in the [H_2pout]$^{3-}$ was also interrogated by Mössbauer spectroscopy. The Mössbauer spectrum of the of the Fe^{II}–OH has isomer shift and quadrupole splitting values consistent with a high spin Fe^{II} consistent with an S = 2 spin ground state (Figure 4.8A). The Fe^{III}–OH was also found to have Mössbauer

parameters of δ = 0.35 mm/s and ΔE_Q = 0.40 mm/s that are consistent with a high spin Fe^{III} center as with both D and E/D parameters that were consistent with the magnetic properties evaluated by EPR spectroscopy (Figure 4.8B). The one-electron oxidation of the Fe^{III}–OH revealed a Mössbauer spectrum that also reflected the results of the parallel-mode EPR experiment, albeit with a much lower purity. While the Mössbauer spectrum confirmed generation of an Fe^{IV} species with parameters of δ = 0.05 mm/s and ΔE_Q = 0.37 mm/s, the yield was 40% (Figure 4.8C). The rest of the sample constituted unreacted Fe^{III}–OH and some other Fe^{III} species. The minimal amount of Fe^{III}–OH complex can be observed in the perpendicular-mode EPR spectrum of the Fe^{IV} species. While the Mössbauer studies did confirm the generation of an Fe^{IV} complex, magnetic studies are hindered by the low

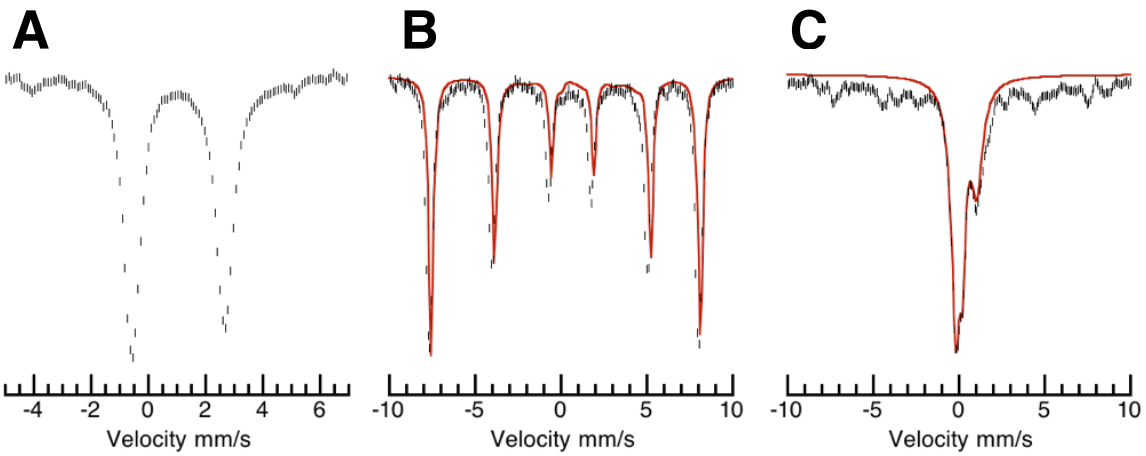

Figure 4.8 ^{57}Fe Mössbauer spectra of $[Fe^{II}H_2pout(OH)]^{2-}$ (**A**); $[Fe^{III}H_2pout(OH)]^{-}$ (**B**); and $[Fe^{IV}H_2pout(O)(H)]$ (**C**) in 1:1 DMF:THF. Sample temperature 4.2 K. Red lines are least square fits of the experimental data.

purity of the sample. Further experiments are necessary to optimize the preparation of a Mössbauer sample for $[Fe^{IV}H_2pout(O)(H)]$.

Vibrational Studies on Fe^{IV} species. We returned to NRVS spectroscopy to further interrogate the Fe^{IV} species. Although, as noted above the Fe^{IV} sample was not pure, we did a preliminary investigation of the Fe–(O)(H) vibration using NRVS. [$Fe^{IV}H_2$pout(O)(H)] species showed an Fe–O vibration at 795 cm^{-1}, which is consistent with the Fe^{IV}–oxido vibrations reported for [$Fe^{IV}H_3$buea(O)]$^-$ (Figure 4.9).[76] The preliminary vibrational data suggested that an Fe^{IV}–hydroxido species was not produced from the one-electron

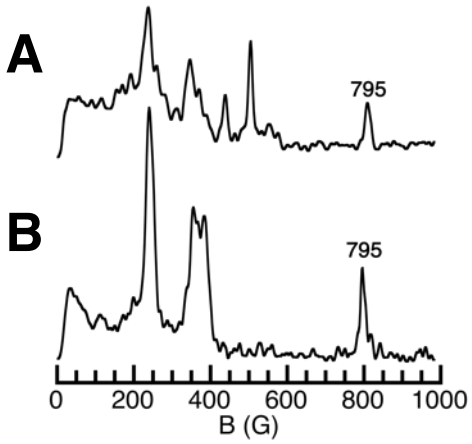

Figure 4.9 NRVS spectra for [$Fe^{IV}H_2$pout(O)(H)]$^-$ (**A**), [$Fe^{IV}H_3$buea(O)]$^-$ (**B**). The peaks for the Fe–O vibrations are labelled with their corresponding energies.

oxidation of [$Fe^{III}H_2$pout(OH)]$^-$. It is worth noting that the Fe–O vibration associated with an Fe^{IV}–oxido complex in the symmetrical phosphinic amide system, [poat]$^{3-}$ (*see chapter 6*) is at 843 cm^{-1}, which is significantly higher in energy than the vibration reported for the symmetrical urea system. It is difficult to predict, quantitatively, how alteration of the ligand field as well as the local environment will affect the Fe–O vibration. It is possible that that [$Fe^{IV}H_2$pout(O)(H)] and [$Fe^{IV}H_3$buea(O)]$^-$ have the same energy Fe–O band, but are of different composition. Further experiments are needed to fully characterize this species and determine if it is an Fe^{IV}–OH species.

Independent preparation of [Fe^{IV}H$_2$pout(O)]$^-$.

In order to further identify the species resulting from the one-electron oxidation of [Fe^{III}H$_2$pout(OH)]$^-$, an [Fe^{IV}H$_2$pout(O)]$^-$ species was prepared by a different method. A solution of H$_5$pout, Fe^{II}(OAc)$_2$, and three equivalents of KH in DMA afforded for the isolation of the "empty" cavity complex [Fe^{II}H$_2$pout]$^-$. Subsequent addition of one equivalent of isopropyl 2-iodoxybenzoate (IBX-iPr) to a solution of [Fe^{II}H$_2$pout]$^-$ and 18-crown-6 ether (18c6) to help solubilize in EtCN at – 80 °C showed generation of a new compound with spectroscopic features suggestive of an Fe^{IV} center (Scheme 4.4).

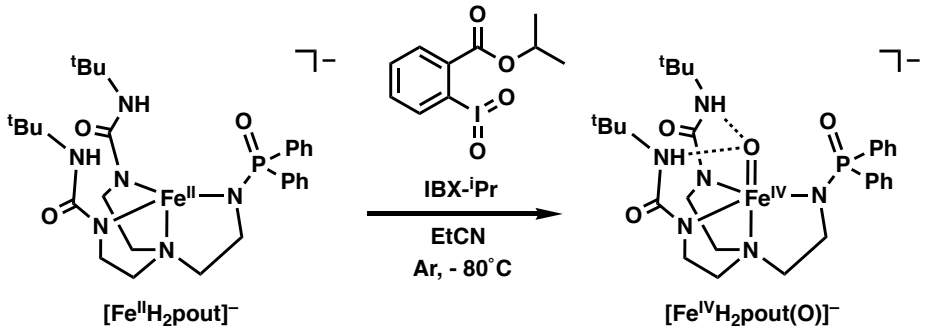

Scheme 4.4 Alternative route to prepare of Fe^{IV}–O complex.

Initiation of the reaction of [Fe^{II}H$_2$pout]$^-$ with IBX-iPr was monitored optically and produced a new spectrum with bands at λ_{max} = 380, 500 (sh), 807 and 867 (sh) nm (Figure 4.8A). The final spectrum resembles that of [Fe^{IV}H$_3$buea(O)]$^-$, which has absorbance features λ_{max} (ε_M) = 350 (4200), 440 (3100), 550 (1900) and 808 (280) nm (Figure 4.8A). The Mössbauer spectrum of the initial [Fe^{II}H$_2$pout]$^-$ revealed a clean spectrum with parameters of δ = 1.01 mm/s and ΔE_Q = 2.75 mm/s, consistent with a high spin Fe^{II} species, but distinct from the Fe^{II}–OH complex (Figure 4.10B). Upon addition of IBX-iPr, the sample shows full consumption of the starting Fe^{II} compound, but a mixture of paramagnetic

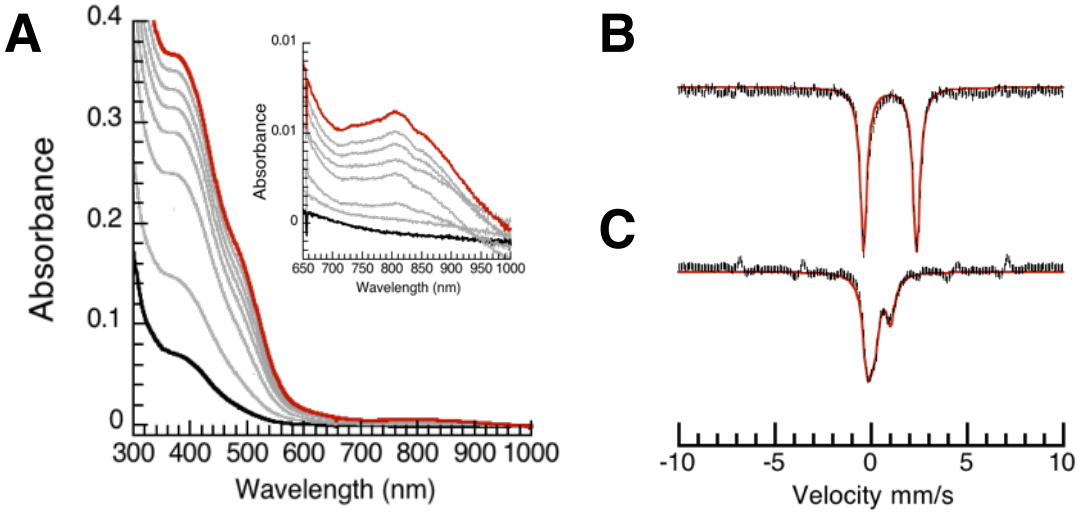

Figure 4.10 Monitoring the generation of $[Fe^{IV}H_2pout(O)]^-$ via UV-vis, $[Fe^{II}H_2pout]^-$ (black) to $[Fe^{IV}H_2pout(O)]^-$ (red) (**A**) and Mössbauer spectroscopies (**B** and **C**). Sample temperature 4.2 K. Red lines are simulations.

species. Initial analysis assigns the mixture to be composed of $[Fe^{III}H_2pout(OH)]^-$, adventitious Fe^{III}, and a species with parameters consistent with an Fe^{IV} center of $\delta = 0.06$ mm/s and $\Delta E_Q = 0.30$ mm/s (Figure 4.8C). The parameters for the Fe^{IV} species generated by route of an O-atom transfer reagent are similar to that of the one-electron oxidized species from $[Fe^{III}H_2pout(OH)]^-$; however, it is still necessary to improve the yield of this species, to evaluate this species by EPR spectroscopy, and analyze the magnitude of D for this species.

Summary and Conclusions

Although protein active sites have been suggested to readily employ protonated Fe^{IV}–oxido species, they are tremendously difficult to prepare in synthetic frameworks. One possible reason for this difficulty is the lack of highly regulated and controlled local environments about metal centers in synthetic systems. To this end, we developed a hybrid tripodal ligand that has the capability to form three intramolecular H-bonds with a hydroxido ligand. Isolation and interrogation of the low valent $[Fe^{II}H_2pout(OH)]^{2-}$ and

$[Fe^{III}H_2pout(OH)]^-$ validate the conceptual design principles of the H-bonding cavity in $[H_2pout]^{3-}$. This is demonstrated clearly by the solid state structure of $[Fe^{III}H_2pout(OH)]^-$, where the urea NH groups act as H-bond donors and the O–atom of the phosphinic amide arm as a H-bond acceptor.

We further demonstrated that the $[Fe^{III}H_2pout(OH)]^-$ compound can be oxidized by one-electron to give an Fe^{IV} species. It remains unclear whether this species exists as an Fe^{IV}–OH or Fe^{IV}–O as preliminary data is contradictory. While vibrational data suggests that upon oxidation of $[Fe^{III}H_2pout(OH)]^-$, an Fe^{IV}–oxido species is generated, the distinct negative zero field splitting parameter (– 2 cm^{1-}) necessitates further investigation. Independent preparation of a tentative Fe^{IV}–oxido complex via an O–atom transfer reagent show optical signatures different from the one-electron oxidized species. This species' magnetic properties have yet to be thoroughly evaluated and need to be before a definitive assignment can be made.

Experimental Section

General Procedures. All manipulations, unless otherwise stated, were completed under an argon atmosphere in a VAC drybox. Solvents were sparged with argon and dried over columns containing Q-5 and molecular sieves. All reagents were purchased from commercial suppliers and used as received unless otherwise noted. Potassium hydride as a 30% suspension in mineral oil was filtered and washed five times each with Et_2O and pentane and dried under vacuum. IBX-iPr Ester[185], $FcBF_4$[145] and the ligand precursors H_5pout[183] were synthesized using literature procedures.

Physical Methods. Electronic absorption spectra were recorded in a 1 cm cuvette on an 8453 Agilent UV-vis spectrometer equipped with an Unisoku Unispeks cryostat. X-band

(9.28 GHz) EPR spectra were collected as frozen solutions using a Bruker EMX spectrometer equipped with an ER041XG microwave bridge. Mössbauer spectra were recorded with a Janis Research Super-Varitemp dewar.

X-ray Crystallographic Methods. A Bruker SMART APEX II diffractometer was used to collect all data. The APEX23 program package was used to determine the unit-cell parameters and for data collections. The raw frame data was processed using SAINT4 and SADABS5 to yield the reflection data files. Subsequent calculations were carried out using the SHELXTL6 program. The structures were solved by direct methods and refined on F2 by full-matrix least-squares techniques. The analytical scattering factors7 for neutral atoms were used throughout the analysis. Hydrogen atoms H1, H5, and H6 were located from a difference-Fourier map and refined (x,y,z and U_{iso}). The remaining hydrogen atoms were included using a riding model. Disordered atoms were included using multiple components with partial site-occupancy-factors. The structure is polymeric.

K[Fe^{II}H$_2$pout] A solution of H_5pout (0.100 g, 0.184 mmol) in 5 mL DMA was treated with solid KH (0.022 g, 0.55 mmol) and stirred until all H_2 evolved. $Fe(OAc)_2$ (0.032 g, 0.18 mmol) was subsequently added to the yellow solution and stirred for 35 minutes to produce a dark yellow heterogeneous mixture. The mixture was filtered and concentrated to approximately 1 mL DMA. Triturating with the DMA solution with Et_2O allowed for isolation of a pale yellow powder (90%). Mossbauer (DMF:THF, 4K, δ= 1.01 mm/s; ΔE_Q = 2.75 mm/s)

K$_2$[Fe^{II}H$_2$pout(OH)] A solution of H_5pout (0.150 g, 0.275 mmol) in 5 mL DMA was treated with solid KH (0.046 g, 1.1 mmol) and stirred until all H_2 evolved. $Fe(OAc)_2$ (0.048 g, 0.28 mmol) was subsequently added to the light yellow solution and stirred for 35 minutes to

produce a dark red heterogeneous mixture. Water (5 μL, 0.3 mmol) was added via syringe that was stirred for 15 minutes and then filtered through a medium porous-glass frit. Et_2O was allowed to diffuse resulting in light yellow-orange crystals (79 %) suitable for XRD studies. Anal. Calcd for $K_2[FeH_2pout(OH)]$, $C_{28}H_{43}K_2FeN_6O_4P$: C, 48.55; H, 6.26; N, 12.13. Found C, ; H, ; N, . FTIR (ATR, cm^{-1}) 3656, 3261, 3124, 3071, 2955, 2797, 1645, 1585, 1510, 1435, 1390, 1350, 1310, 1245, 1205, 1185, 1115, 1045, 1015, 975, 885, 815, 755, 710, 630. UV-vis (DMF:THF, λmax nm, (ε_{max}, M^{-1} cm^{-1})) 525 (sh). EPR (X-band Parallel-mode, DMF:THF, 16 K, g = 8.57). Mossbauer (DMF:THF, 4K, δ= 1.05 mm/s; ΔE_Q = 3.24 mm/s). $E_{1/2}$ (DMF, V vs $[FeCp_2]^{+/-}$): $Fe^{III/II}$ = – 1.38.

K[$Fe^{III}H_2$pout(OH)] A solution of H_5pout (0.103 g, 0.189 mmol) in 5 mL DMA was treated with solid KH (0.032 g, 0.80 mmol) and stirred until all H_2 evolved. $Fe(OAc)_2$ (0.034 g, 0.20 mmol) was subsequently added to the light yellow solution and stirred for 30 minutes to produce a dark red heterogeneous mixture. Water (4 μL, 0.2 mmol) was added via syringe to the mixture and stirred for 15 minutes. The color of the solution lightened. The now light red-orange mixture was filtered through a medium porous-glass filter. Half an equivalent of elemental I_2 (0.025 g, 0.10 mmol) was added to the light red-orange filtrate, which immediately turned dark red-brown. The solution was left to stir for 1 hour and then was concentrated to dryness under vacuum. The residue was triturated with Et_2O (20 mL x 2) and again dried under vacuum. The free-flowing solid was then redissolved in MeCN (5 mL total) and filtered through a fine porous-glass frit to remove the white solid (KI). Single dark red crystals suitable for XRD studies were afforded by vapor diffusion of Et_2O into the solution of MeCN (83 %). Anal. Calcd for K[FeH_2pout(OH)], $C_{28}H_{43}KFeN_6O_4P$: C, 48.55; H, 6.26; N, 12.13. Found C, 48.87; H, 6.96; N, 12.56. FTIR (ATR, cm^{-1}) 3395, 3238, 3174, 3056,

2953, 2922, 2854, 2727, 2671, 1646, 1611, 1594, 1556, 1461, 1378, 1312, 1297, 1249, 1221, 1120, 1158, 1119, 1068, 1048, 971, 928, 896, 785, 723, 698, 589, 552. UV-vis (DMF:THF, λ_{max} nm, (M^{-1} cm^{-1})) 395 (6500), 480 (sh). EPR (X-band Perpendicular, DMF:THF, 10 K, g = 8.53, 5.38, 3.02, 1.46) Mossbauer (DMF:THF, 4K, δ = 0.35 mm/s; ΔE_Q = 0.40 mm/s)

Preparation of Low-Temperature [$Fe^{VI}H_2$pout(O)(H)] EPR Samples. A solution of [$Fe^{III}H_2$pout(OH)]$^-$ (20 mM, 250 μL) in a DMF:THF mixture with 18c6 added to increase solubility was transferred to an EPR tube and sealed with a rubber septum. The tube was brought out of the dry box and placed in a − 80 °C acetone/dry ice bath and allowed to equilibrate for fifteen minutes. A 0.44 M (0.060 g, 0.22 mmol) stock solution of $FcBF_4$ was prepared in a DMF:THF mixture and kept at – 35 °C for the duration of the experiments. One equiv of oxidant (11 μL) was added via a syringe. After mixing by careful shaking of the tube, the EPR tube was quickly removed from the cold bath, wiped clean of acetone, and frozen in liquid nitrogen before analysis.

Preparation of solution NRVS Samples for and [$^{57}Fe^{III}H_2$pout(OH)]$^-$ and [$^{57}Fe^{IV}H_2$pout(O)(H)]. Solution NRVS sample holders were prepared from Mössbauer sample holders by cutting a 2 x 6 mm slot out of the bottom and covering the hole with kapton tape. A 40 mM solution of 96% ^{57}Fe-enriched [$^{57}Fe^{III}H_2$pout(OH)]$^-$ (0.027 mg, 0.041 mmol) was prepared in DMF:THF (1 mL) with 18c6 added to increase solubility. A NRVS sample holder was cooled in the cold well of a drybox to -196 °C. To the pre-cooled NRVS sample holder, a sample of [$^{57}Fe^{III}H_2$pout(OH)]$^-$ (500 μL of the 40 mM solution) was added via syringe and allowed to freeze completely. The sample was then transferred from the dry box and quickly placed in a storage container pre-cooled to 77 K. Samples were analyzed for purity using Mössbauer

spectroscopy prior to, and after NRVS data collection. In the case of [$^{57}Fe^{IV}H_2$pout(O)(H)], analogous prep was followed in a DMF:THF mixture with the following modifications: A 40 mM solution of 96% ^{57}Fe-enriched [$^{57}Fe^{II}H_2$pout(OH)]$^{2-}$ (0.028 mg, 0.040 mmol) was prepared in DMF:THF (1 mL) with 18c6 added to increase solubility. A 4.4 M (0.030 g, 0.11 mmol) stock solution of $FcBF_4$ was prepared in a DMF:THF mixture (500 µL) and kept at –35 °C for the duration of the experiments. Two equivalents of oxidant (90 µL) was added via a syringe. After mixing, a 500 µL (34 mM) aliquot of the sample was transferred to the NRVS cup and allowed to completely freeze followed by transferred from the dry box and quickly placed in a storage container pre-cooled to 77 K.

CHAPTER 5

A High Spin Fe^{IV}–oxido Complex and Its Interactions with Lewis Acids

To gain insight on the role of the Ca^{2+} ion in the oxygen evolving complex (OEC), synthetic chemists have sought to interrogate the influence of Lewis acids (LA) on the reactivity of high valent metal-oxido units. The works of Fukuzumi/Nam[186], Que[187], and Goldberg[188–191] are a few examples exploring the effects of LA on synthetic compounds. Recently, the Goldberg lab reported that addition of LA (LA = $Zn(OTf)_2$, $B(C_6F_5)_3$, HBArF , or TFA) to their $Mn^{V}(O)(TBP_8Cz)$ complex resulted in tautomerization to a Mn^{IV}–ligand radical ($Mn^{IV}(O–LA)(TBP_8Cz^{\bullet+})$) species (Figure 5.1). The subsequent $Mn^{IV}(O–LA)(TBP_8Cz^{\bullet+})$) was found to be more reactive towards C–H substrates than the Mn^{V} complex when LA = $Zn(OTf)_2$ or $B(C_6F_5)_3$. Surveying several LA, Goldberg and coworkers found that the rate of reactivity toward C–H bond activation was dependent on the strength of the LA added.[191]

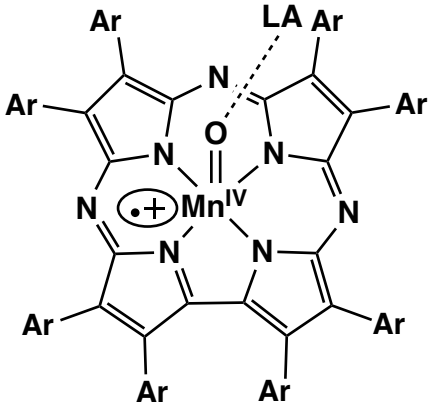

Figure 5.1 The ($Mn^{IV}(O–LA)(TBP_8Cz^{\bullet+})$) complex derived from addition of LA to the Mn^{V}–oxido complex developed in the Goldberg lab. LA = $Zn(OTf)_2$, $B(C_6F_5)_3$, HBArF , or TFA.

While the work discussed above and in chapter 1 shed light on how LA can influence the reactivity of redox-active metal ions, these approaches often lack evidence of the structural implications of the auxiliary metal ion. Reports commonly will illustrate that the LA directly interacts with the high valent metal-oxido unit without sufficient evidence to

support that assumption. For example, in 2010, Nam and Fukuzumi reported the first crystallographic evidence of a complex containing a Fe^{IV}–O–Sc^{III} core (Figure 5.2A);[59] however, they did not evaluate the complex by several methods that would be standard protocol when interrogating an Fe center, especially Mössbauer spectroscopy. Shortly after, a computational study by Swart questioned these findings suggesting that the scandium ion was playing an active role in the formation of the complex and that the generated complex did not contain an Fe^{IV} center.[192] Additionally five years later, after a thorough reinvestigation of this compound by Mössbauer, X-ray absorption, and EPR spectroscopies as well as electrospray ionization mass spectrometry, Que reported that the adduct should instead be formulated as Fe^{III}–O–Sc^{III} (Figure 5.2B).[174] These studies further bring to question the ability of an electrophilic metal–oxido to bind a LA.

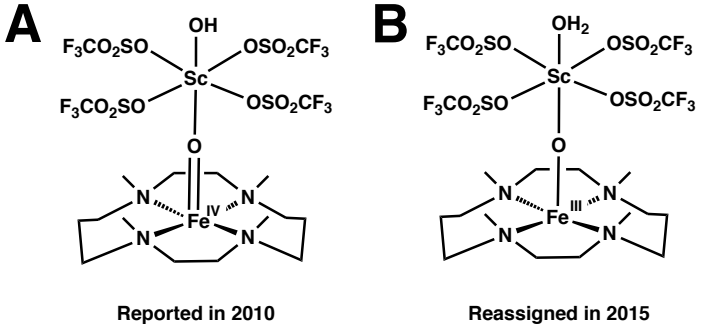

Figure 5.2 Reported Sc^{3+} ion bound Fe^{IV}–oxido complex reported by Nam (**A**). Revisited complex, reassigned to be an Fe^{III} species by Que in 2015 (**B**).

To achieve synthetic structural motifs similar to enzyme active sites, like in the OEC, is challenging due to the intricate arrangement of metal ions and non-covalent interactions found within proteins. The OEC is exceptionally difficult to structurally emulate due to the nature of the multimetallic cluster, which, as previously described, requires precise placement of four Mn and one Ca^{2+} ions. One impressive synthetic example that illustrates how multiple redox active and inactive metal ions cooperatively interact with metal-

oxido/hydroxido units is from the Agapie group, who developed and structurally characterized a tri-Mn cluster with the capacity to bind a fourth metal ion (Figure 5.3). Upon coordination of an auxiliary fourth metal ion (Na^{+}, Ca^{2+}, Sr^{2+}, Zn^{2+}, or Y^{3+}) to the cluster, they showed a correlation between the Lewis acidity of the added metal and redox

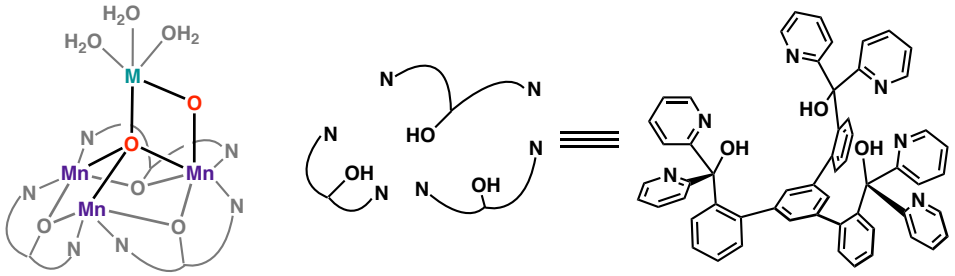

Figure 5.3 Multimetallic cluster developed by the Agapie group to study the effect of a series of redox-inactive metal ions on the tri-Mn core. M = Na^{+}, Ca^{2+}, Sr^{2+}, Zn^{2+}, Y^{3+}

potential of the cluster, which was found to decrease ~100 mV per pK_a unit.[57,193,194] (pK_a was used was used as a measure of Lewis acidity) Similar studies were also performed on the analogous tri-Fe cluster, which was found to follow a similar trend as the Mn cluster.[195]

In our lab, the $[MST]^{3-}$ system established a foundation for the preparation of bimetallic complexes with both redox-active and redox-inactive metal ions that resembles one structural component of the OEC cube: M^{II}–(μ–OH)–TM^{III} (M^{II} = Ca^{II}, Sr^{II}, or Ba^{II} and TM^{III} = Mn^{III} or Fe^{III}) (Figure 5.4);[68,83,196] however, the system is unable to access high valent

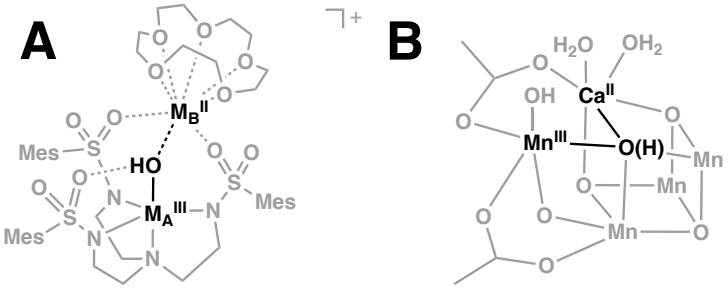

Figure 5.4 Discrete heterobimetallic complex developed by our group (**A**) resembling one structural component of the OEC cube (**B**). M^{II}–(μ–OH)–TM^{III} (M^{II} = Ca^{II}, Sr^{II}, or Ba^{II} and TM^{III} = Mn^{III} or Fe^{III}).[14-16]

metal species that are relevant to the active oxidants in biological systems. Additionally, even though the $[H_3buea]^{3-}$ framework (Figure 1.6) has been able to support such high valent species, the culmination of data presented in chapter 4, in conjunction with a previously published report,[76] support that in order to interrogate the addition of Lewis acids to our complexes, we must move away from urea containing systems. As discussed in Chapter 2, the design premise behind the usage of phosphinic amides was that the deprotonated phosphinic amide nitrogen atom would produce a ligand field that stabilizes high valent complexes, and that the P=O units would serve as an H-bond acceptor, an auxiliary metal binding site, and produce a negative polarized cavity to help stabilize high valent metal–hydroxido/oxido complexes (Figure 5.5).

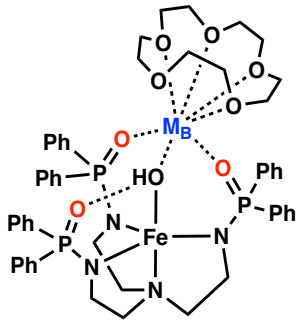

Figure 5.5 Schematic of metal complex with $[poat]^{3-}$ illustrating the utility of the P=O moieties as an auxiliary binding site and/or H-bond acceptor.

In this chapter, the chemistry of a new high spin, Fe^{IV}–oxido complex supported by $[poat]^{3-}$ is discussed along with its reactivity with Lewis acids. These complexes have been characterized by several spectroscopic methods including UV-vis, parallel-mode (||–mode) electron paramagnetic resonance (EPR), Mössbauer, nuclear resonance vibrational (NRVS), and X-ray absorption (XAS) spectroscopies. The combined data show that addition of a series of Lewis acids to the $[Fe^{IV}poat(O)]^-$ complex generate distinct Fe^{IV} species. For example, unlike $[Fe^{IV}poat(O)]^-$, the LA adducts showed strong features in their ||–mode

EPR spectra. The change in signal intensity was attributed to the disruption of the high symmetry of the Fe^{IV}–oxido complex upon binding a LA. Throughout this study, Ca^{2+} and Mg^{2+} adducts were found to have similar spectroscopic characteristics and were further interrogated to determine how the LA was interacting with the oxido ligand. Preliminary data on the addition of protons to $[Fe^{IV}poat(O)]^-$ is also discussed.

Results and Discussion

Synthesis of [Fe^{II}poat]$^-$. To prepare the Fe^{II} complex of $[poat]^{3-}$, a solution of H_3poat in anhydrous tetrahydrofuran (THF) was treated with three equivalents of potassium hydride (KH). After H_2 evolution ceased, $Fe^{II}(OAc)_2$ was added. The reaction mixed was filtered and

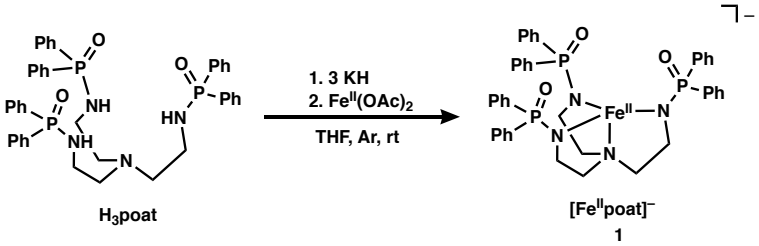

Scheme 5.1 Synthesis of $[Fe^{II}poat]^-$ (**1**).

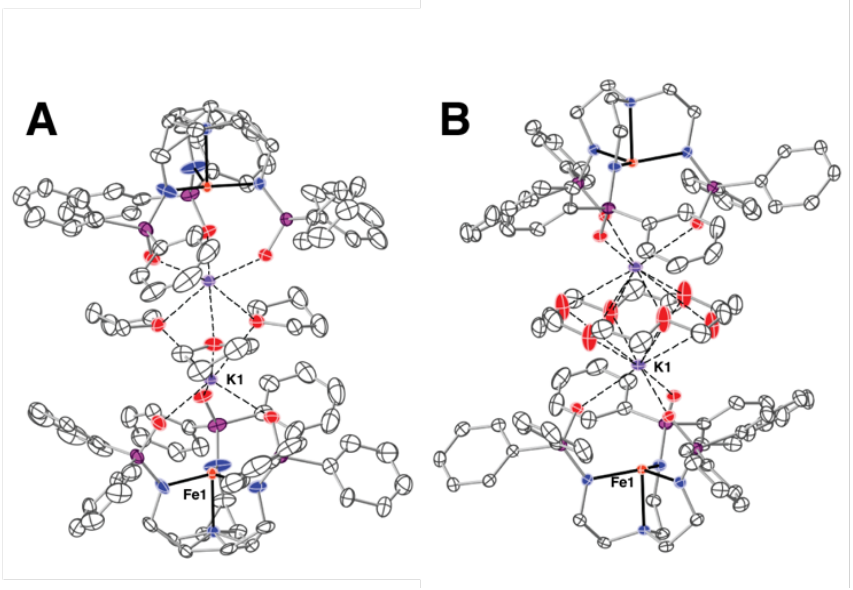

Figure 5.6 Molecular structure of $K[Fe^{II}POAT])_2$•3THF (**A**) and (18c6)$(K[Fe^{II}POAT])_2$ (**B**) determined by XRD methods illustrating the interaction of the K^+ ions with the oxygen atoms of the P=O units. Thermal ellipsoids are drawn at the 50% probability level.

single crystals of the metal salt were obtained by diffusion of diethyl ether (Et_2O) in the THF solution (Scheme 5.1). The structure of K[Fe^{II}poat] showed a four-coordinate, mononuclear, Fe^{II} center in trigonal monopyramidal geometry with a potassium ion bound to the P=O oxygen atoms (Figure 5.6A). Two K[Fe^{II}poat] complexes assemble about three THF molecules, which fill the coordination spheres of K^+ ions.

The ||–mode EPR spectrum of a frozen solution of the recrystallized material with 2 equivalents of 18-crown-6 ether (18c6), added to increase solubility, corroborated the assignment of a monomeric high spin ferrous center with a sharp feature at g = 9.47 (Figure 5.7A). A Mössbauer spectrum of [Fe^{II}poat]$^-$, prepared analogously to the EPR sample, showed a single doublet with an δ = 1.02 mm/s and ΔE_Q = 2.54 mm/s that are consistent with a monomeric Fe^{II} center (Figure 5.7B). The two equivalents of 18c6 were found necessary to disrupt the K^+ ion interactions with the P=O moieties of the complex. It was determined crystallographically that one equivalent of 18c6 produced a structure in

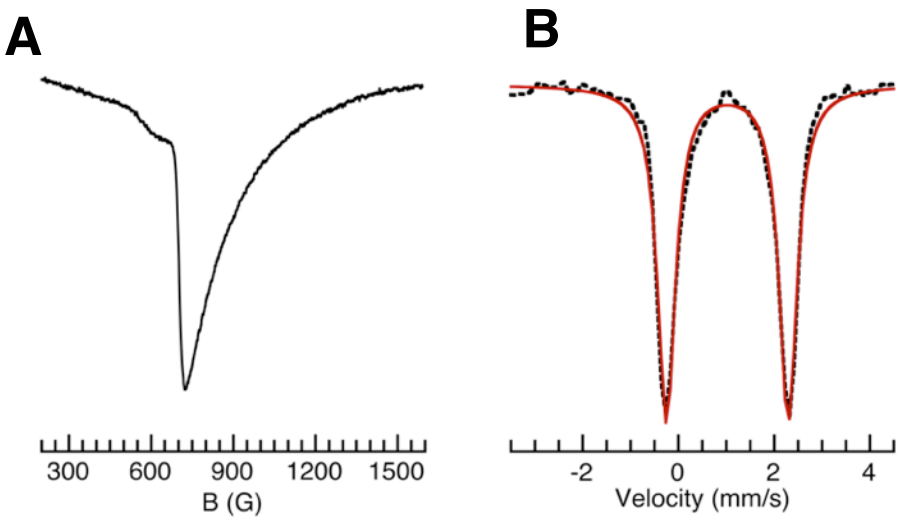

Figure 5.7 EPR (**A**) and Mössbauer (**B**) spectra of **1+18c6**. Recorded at 10 K and 4 K, respectively, in a DMF:THF. Red lines are the least-squares fits of the experimental Mössbauer data.

which the K^+ would sit outside of the crown ether and fill its coordination sphere with the oxygen atoms of the P=O moieties (Figure 5.6B).

G*eneration of the (18c6)$_2$K[Fe^{IV}poat(O)].*

Spectroscopic Studies. The treatment of (18c6)$_2$K[Fe^{II}poat] (**1**) with one equivalent of the O–atom transfer reagent, isopropyl 2-iodoxybenzoate (IBX-iPr), in propionitrile (EtCN) at – 60 °C (Scheme 5.2) was monitored spectrophotometrically and showed growth of absorbance

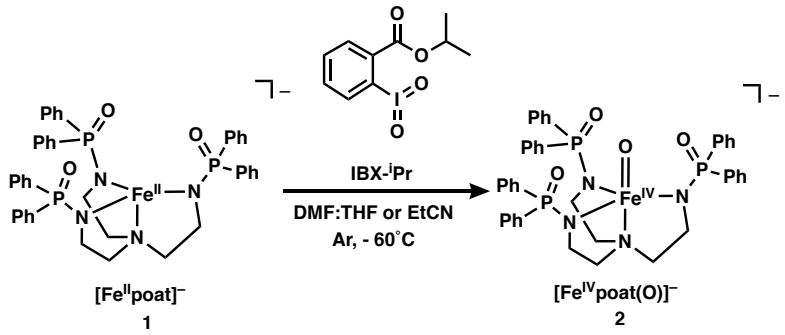

Scheme 5.2 Generation of [Fe^{IV}poat(O)]$^-$ (**2**).

features at λ_{max}, nm (ε, M^{-1} cm^{-1}) = 320 (8260), 370 (9590), 520 (1205) and 950 (450) (Figure 5.8A) consistent with the previously characterized [Fe^{IV}H$_3$buea(O)]$^-$ and assigned as [Fe^{IV}poat(O)]$^-$ (**2**).[42] Although red shifted compared to [Fe^{IV}H$_3$buea(O)]$^-$, the low energy absorbance band at λ_{max} = 950 nm is suggestive of the generation of a high valent Fe^{IV}–oxido species.[42] The Mössbauer spectrum corroborated the assignment of an Fe^{IV} species, revealing a single doublet with an δ = 0.1 mm/s and ΔEq = 0.28 mm/s consistent with a monomeric S = 2 system (Figure 5.8B) in high purity (> 95% of the Fe content). In addition, the ||–mode EPR spectrum showed a weak signal at g = 8 (Figure 5.8C). Initially, the signal intensity was surprising as the [Fe^{IV}H$_3$buea(O)]$^-$ complex has a strong and sharp signal at g = 8.1.[180,184] After further analysis, the rhombicity parameter (E/D) for **2** was found to equal 0.013(8), which is significantly smaller than that found for [Fe^{IV}H$_3$buea(O)]$^-$ (E/D =

0.03(12)).[42,180] Signal intensity is proportional to $(E/D)^4$, suggesting that systems with highly symmetrical ligand fields are expected to have weak EPR signals. The small E/D value for **2** is attributed to the nearly symmetric C_{3V} environment provided by the ligand framework of $[poat]^{3-}$ surrounding the Fe–oxido unit.

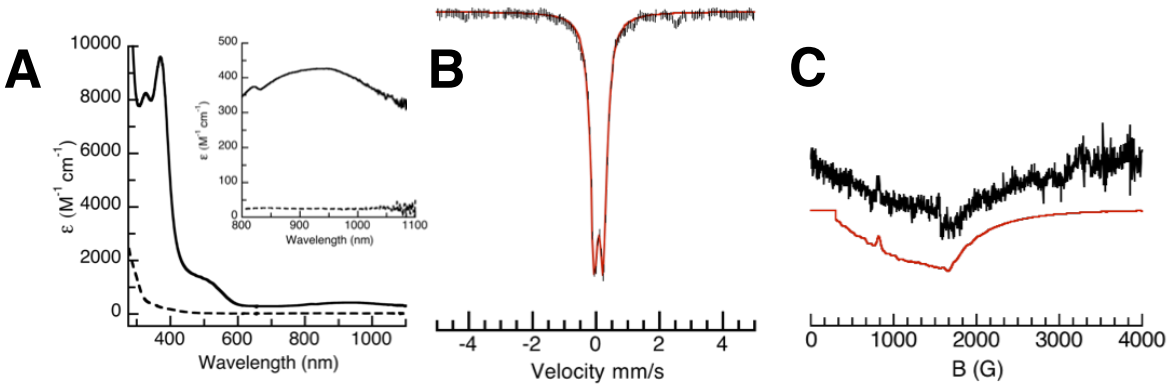

Figure 5.8 Electronic absorbance spectra for the generation of **2** (black solid) from treatment of **1** (black dashed) with IBX-iPr at – 60 °C in a EtCN mixture. Inset: A zoom of the low energy (**A**). Mössbauer (**B**) and EPR (**C**) spectra of **2**. Recorded at 10 K in a DMF:THF and 4 K in EtCN, respectively. Red lines are simulations of experimental data.

Treatment of $(18c6)_2K[Fe^{IV}poat(O)]$ with Lewis acids.

The nearly axial symmetry imposed by the ligand framework on the Fe^{IV}–oxido unit with $[poat]^{3-}$, allowed for us to probe the binding of Lewis acids to the complex. We hypothesized if a Lewis acid interacted with the metal complex, it would disturb the symmetry of the pure Fe^{IV}–oxido species, which would be reflected in the EPR spectrum. Due to the relevance of the Ca^{2+} ion in the OEC, studies began with $15c5Ca(OTf)_2$. The addition of one equivalent of $15c5Ca(OTf)_2$ to **2** was first monitored spectrophotometrically at – 60 °C in EtCN. Upon addition of Ca^{2+} ions the spectrum showed formation of a new species assigned as $[(15c5)\supset Ca^{II}–(\mu\text{-}O)–Fe^{IV}poat]^+$ (**3**) with λ_{max} = 420, 600 and 860 nm (Figure 5.9A). Worth noting is the low energy band at 860 nm. The persistence of the low energy transition is suggestive that the Fe^{IV}–oxido unit is still

present after the addition of a Ca^{II} ion. Density functional theory (DFT) calculations are currently underway to further evaluate the shift.

The addition of 15c5Ca$(OTf)_2$ to **2** was also found to affect the EPR and Mössbauer properties. In the ||–mode EPR spectrum there was growth of a signal at g = 8.07 with both a larger intensity and broader line shape (fwhm = 70 G) than seen for the independent $[Fe^{IV}poat(O)]^-$ (fwhm = 40 G) (Figure 5.9B). The growth of the signal intensity can be attributed to perturbation of the complex's symmetry upon binding of the external ion to the Fe^{IV}–oxido unit reflected in the increase of the E/D parameter to 0.056(3). Upon addition of Ca^{2+} ions, the Mössbauer spectrum showed a doublet with δ = 0.03 mm/s and ΔE_q = 0.39 mm/s remaining consistent with an Fe^{IV} center, but distinct from the Fe^{IV}–oxido species (Figure 5.9C). Of interest is the decrease in the isomer shift indicating a more positive iron center, which is consistent with electron density being pulled away from the Fe center by a coordinated Ca^{2+} ion.

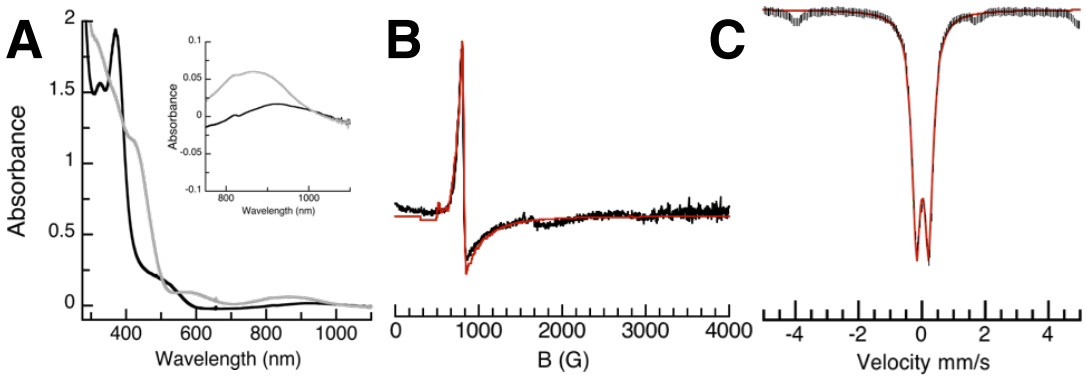

Figure 5.9 Electronic absorbance spectra (**A**) Inset: A zoom of the low energy region. EPR spectra (**B**) and Mössbauer spectra (**C**) of for the conversion of **2** (black)to **3** (gray)at – 60 °C in EtCN. Spectra recorded at 10 K for EPR and 4 K for Mossbauer in a DMF:THF mixture or EtCN, respectively, at – 80 °C. Red lines are simulations of the experimental spectra.

Studies surveying several additional alkaline metals (Mg^{2+}, Sr^{2+}, and Ba^{2+}) were started to examine how varying Lewis acidity would affect the Fe^{IV}–oxido unit. Initial studies monitored the addition of Mg^{2+}/Sr^{2+}/Ba^{2+} ions (with appropriate crown ether used based on size of LA) to **2** by UV-vis spectroscopy (Figure 5.10A and B). As seen with Ca^{2+}, addition of Mg^{2+}/Sr^{2+}/Ba^{2+} showed a blue shift of the low energy band attributed to the Fe^{IV}–oxido complex. The energy of the low energy feature of the [(crown)⊃M^{II}–(μ-O)–

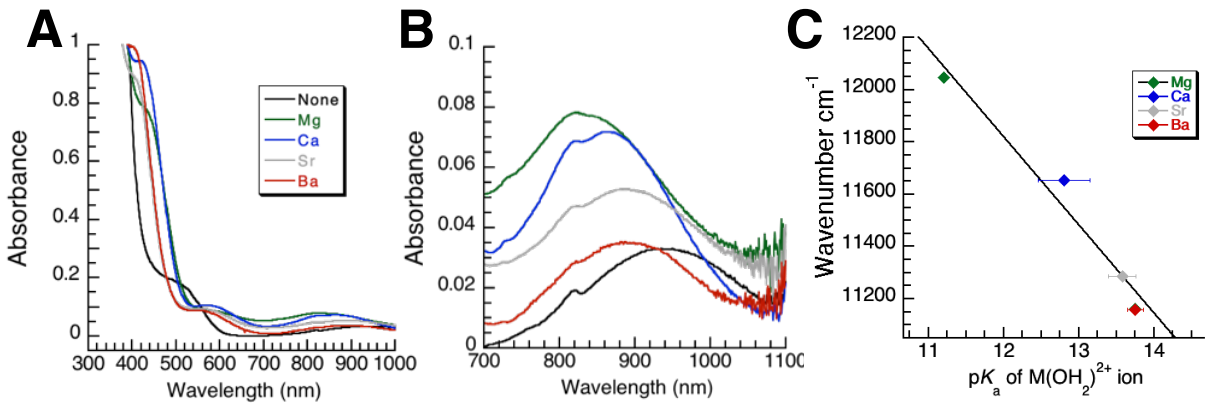

Figure 5.10 Electronic absorbance spectra of respective [(crown)⊃M^{II}–(μ-O)–Fe^{IV}poat]$^+$ (**A**). A zoom of the low energy region for comparison (**B**). Spectra recorded in EtCN at – 60 °C. Energy of low energy feature for [(crown)⊃M^{II}–(μ-O)–Fe^{IV}poat]$^+$ complexes vs pKa of the corresponding $M(OH_2)^{2+}$ ion as a measure of Lewis acidity (**C**).

Fe^{IV}poat]$^+$ was plotted against the pK_a of the metal-aquo complex ions, $M(OH_2)_x{}^{n+}$, in water[197], which has previously been used as a measure of Lewis acidity.[193–195] There is a nearly linear correlation (R^2 = 0.96) between the energy of the d–d transition and Lewis acidity of the redox-inactive metal added (Figure 5.10C). This effect could be a consequence of the LA interacting with the Fe^{IV}=O unit, P=O units, or both: the stronger the LA, the larger amount of splitting within the d-orbital manifold, which is reflected in a progressive shift to higher energy of the d-d transition.

The series of LA adducts was also interrogated by ||–mode EPR spectroscopy. The Mg^{2+} adduct showed a feature at g = 8.15 that was similar in shape to the signal seen for the

Table 5.1 ||–mode EPR signal for Fe^{IV}–oxido complexes

LA	G
Mg	8.15
Ca	8.07
Sr	7.89
Ba	--

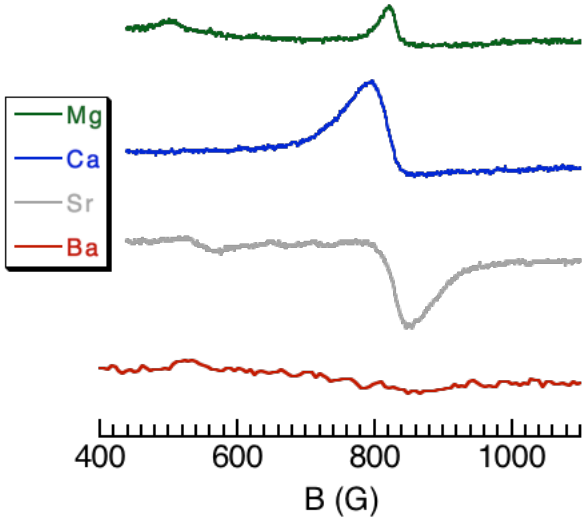

Figure 5.11 ||–mode EPR spectra of respective [(crown)⊃M^{II}–(μ-O)–Fe^{IV}poat]$^+$ adducts. Samples were ~15 mM prepared in a DMF:THF mixture at –80 °C. Spectra recorded at 10 K.

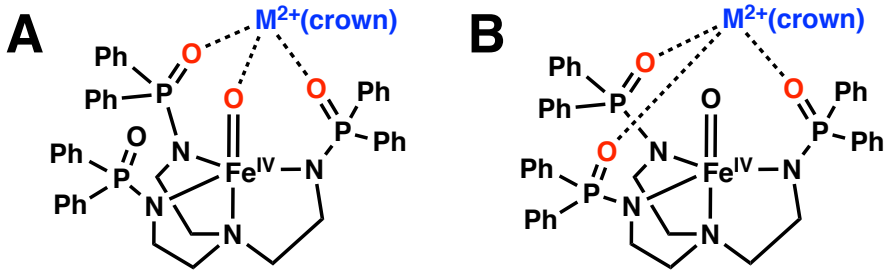

Figure 5.12 Possible binding modes of Lewis acids.

Ca^{2+} species. The Sr^{2+} and Ba^{2+} complexes showed different results: for the Sr^{2+} adduct a signal was observed at higher field, g = 7.89, and inverted in shape, while the Ba^{2+} system showed no apparent signal in the ||–mode spectrum (Figure 5.11 and Table 5.1). Reasons for the differences in the EPR spectra are still being investigated. One possibility is that there are multiple modes of binding a LA to the complex. For example, when adding a smaller LA, like Ca^{2+}, the Ca^{2+} ion has access to directly interact with the Fe–oxido unit (Figure 5.12A). Directly binding the oxido ligand would be expected to disrupt the

symmetry of the complex to a larger extent as seen with the more intense EPR signals. Conversely, large ions like Ba^{2+} ion would perhaps not be able to access the oxido ligand and just binds the three oxygen atoms of the P=O moieties (Figure 5.12B), which could maintain a higher degree of symmetry that prevents detections of an EPR signal.

With these preliminary data in hand, experiments went forward focusing on the Mg^{2+} and Ca^{2+} adducts since the ||–mode EPR spectra were most similar to the previously characterized $[Fe^{IV}H_3buea(O)]^-$ complex. Before continuing with the Mg^{2+} adduct, however, the oxidation state of the Fe was corroborated by Mössbauer spectroscopy giving the following parameters, δ = 0.14 mm/s and ΔEq = 0.432 mm/s (Figure 5.13) indicating that an Fe^{IV} center is present. Therefore, we assigned this species as $[(15c5)\supset Mg^{II}–(\mu\text{-}O)–Fe^{IV}poat]^+$ (**4**).

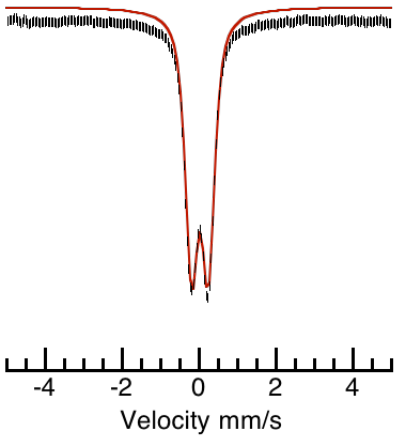

Figure 5.13 Mössbauer spectrum of **4**.

Vibrational Properties. The vibrational properties of **2**, **3**, and **4** were evaluated using nuclear resonance vibrational spectroscopy (NRVS). Evaluating samples containing greater than 85% yield of **2** (^{57}Fe), we obtained a NRVS spectrum with a peak at 843 cm^{-1} that is assigned to the Fe–O vibration, which is significantly higher in energy than the Fe–O

vibration $[Fe^{IV}H_3buea(O)]^-$ complex (795 cm^{-1}).[42,76,198] The energy of the Fe–O vibration of **2** is comparable to that of $[Fe^{IV}(O)(TMG_3tren)]^{2+}$ (843 cm^{-1}), which is also an S = 2 system, but supported by a neutral ligand field.[41,199] Upon addition of Lewis acids to **2**, a decrease in the Fe–O vibration was observed to 822 cm^{-1} and 817 cm^{-1} for **3** and **4**, respectively (Figure 5.14), suggesting that a direct interaction of the complex with these Lewis acids weakens the Fe–O vibration.

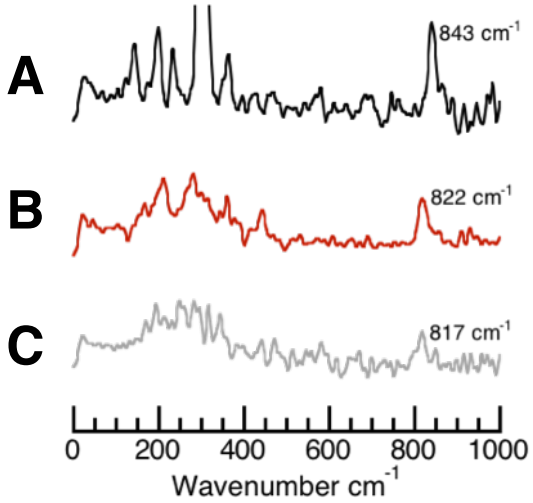

Figure 5.14 NRVS spectra for **2** (**A**), **3** (**B**), and **4** (**C**). Samples were ~25 mM ^{57}Fe in a DMF:THF mixture. The peaks for the Fe–O vibrations are labelled with their corresponding energies.

The Fe–O vibration for **2** was further investigated by solution FTIR studies (Figure 5.15). These experiments include an ^{18}O-labelled sample whose formulation was supported by negative-mode ESI-MS spectrometry. The $[Fe^{IV}poat(^{16}O)]^-$ sample contained a strong m/z = 815.2 that shifted 2 mass units in the ^{18}O–isotopomer (Figure 5.16). Vibrational studies with ^{16}O-labelled samples showed a vibrational peak at 843 cm^{-1} that based on NRVS data is the Fe–^{16}O, however a band attributed to $[Fe^{IV}poat(^{18}O)]^-$ is not resolvable because there are peaks attributed to the complex that prevent detection. Studies are underway to confirm the isotopic shift using NRVS spectroscopy.

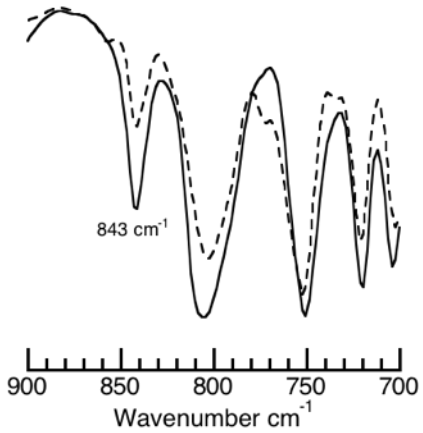

Figure 5.15 Solution FTIR spectra for **2**. Fe–^{16}O (black solid), Fe–^{18}O (black dashed). Samples were ~25 mM in a MeCN at – 40 °C. The peak for the Fe–O vibration is labelled with corresponding energy.

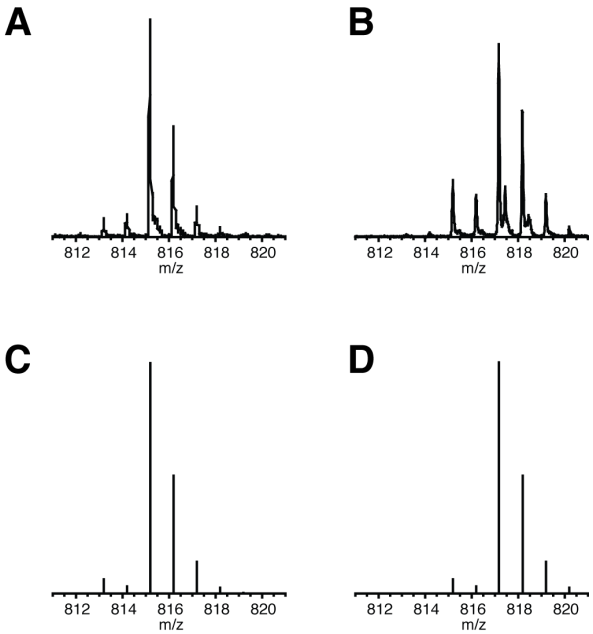

Figure 5.16 Negative-mode ESI mass spectra for [Fe^{IV}poat(^{16}O)]$^-$ (**A**) and [Fe^{IV}poat(^{18}O)]$^-$ (**B**) and their calculated spectra (**C**) and (**D**), respectively. The samples were prepared from [Fe^{II}poat]$^-$ and (^{16}O)IBX-iPr and (^{18}O)IBX-iPr, respectively, in EtCN at – 90 °C.

Structural Properties of [Fe^{IV}(O)] complexes. The thermal instability of the Fe^{IV}–oxido complexes prohibited determination of the molecular structures by X-ray diffraction. Evaluation of the coordination environment about the Fe^{IV} centers thus was analyzed by X-ray absorption spectroscopy (XAS) collected at the Fe K-edge for **2**, **3**, and **4** as frozen

solutions in DMF:THF. The X-ray absorption near-edge structure (XANES) region of **2, 3,** and **4** show similar Fe-K edge energies at 7124.2 eV, 7125.6 eV and 7125.3 eV (Figure 5.17A), which are within the range of these previously reported for synthetic Fe^{IV} complexes.[178,199–201] Within this series, there is a distinct decrease in pre-edge peak area upon addition of the Lewis acids, with values decreasing from 32 units for **2** to 28 and 25 units for **3** and **4**, respectively (Figures 5.17B and 5.18). This trend in pre-edge peak area is consistent with the Lewis acid interacting with the oxido ligand, which would cause a decrease in the mixing of the 3p and 3d orbitals on the Fe center. This decrease causes a less intense transition from the 1s to 3d orbitals and weakening the ligand field strength

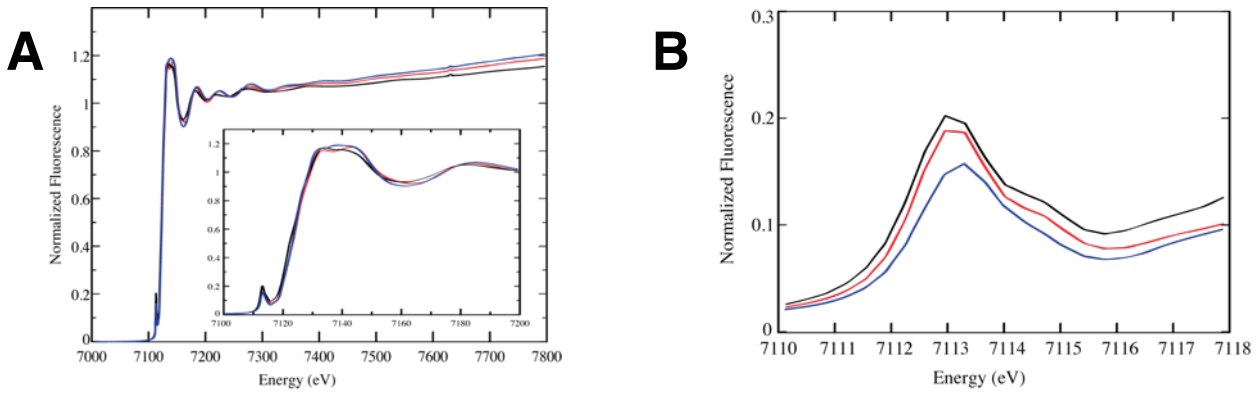

Figure 5.17 Normalized Fe K-edge fluorescence spectra of **2** (black), **3** (red), and **4** (blue). Inset is the zoom on the XANES region (**A**). XAS spectra showing an overlay of the pre-edge region for **2** (black), **3** (red), and **4** (blue) (**B**).

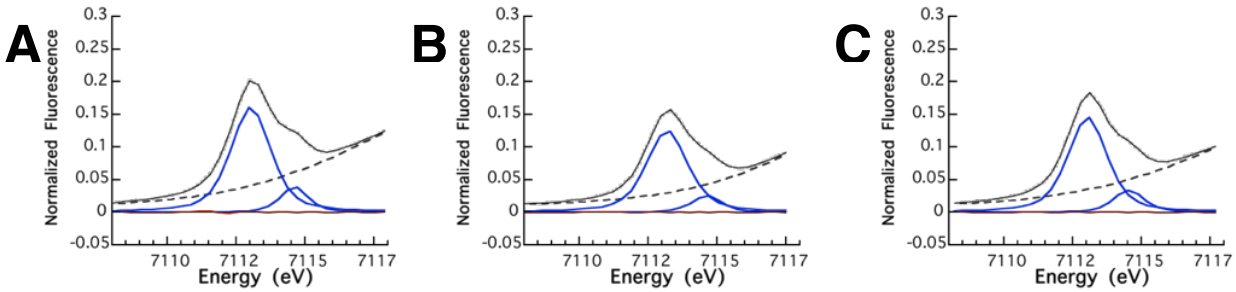

Figure 5.18 Observed X-ray absorption pre-edge regions of **2** (**A**), **3** (**B**), and **4** (**C**). Experimental data are represented by gray dotted lines, with the best fits as black solid lines, the modeled baselines as black dashed lines, the fitted component peaks as blue solid lines, and the residuals as red solid lines.

about the Fe center.[202,203] EXAFS analysis found that the Fe–O bond of **2** to be 1.65(2) Å and 1.67(2) Å for **3** and **4**. The bond lengths of the three oxido complexes are within experimental error of each other (Table 5.2 and Figure 5.19).

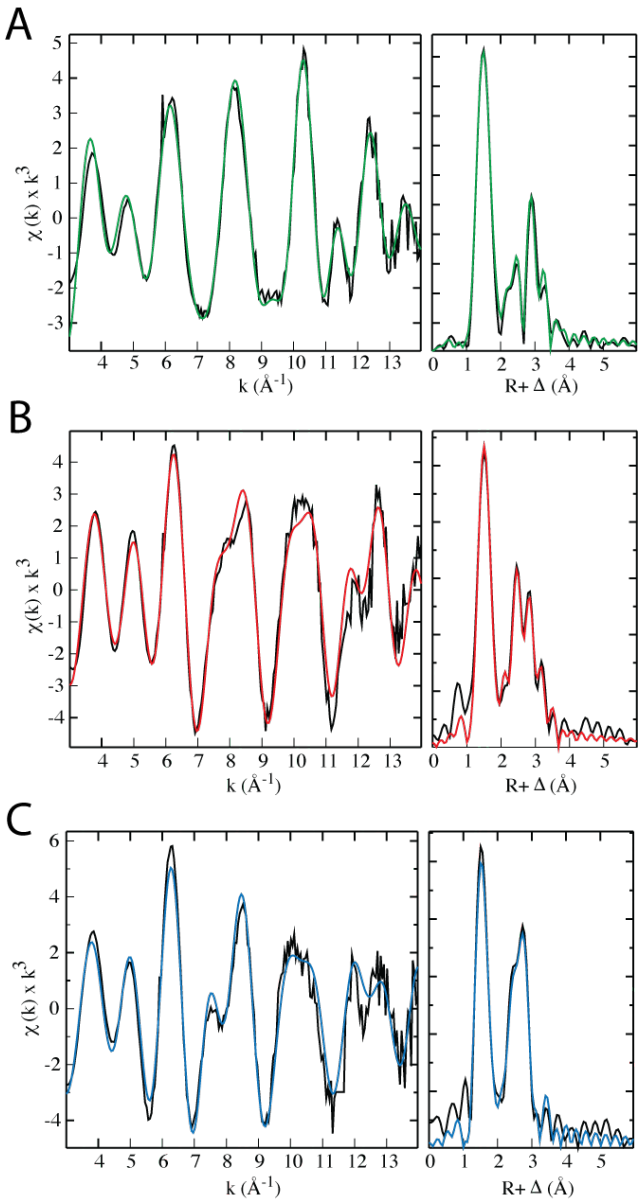

Figure 5.19 Unfiltered EXAFS data (left) and the Fourier transforms (right) for **2** (**A**), **3** (**B**), and **4** (**C**).

Table 5.2 Best fits of EXAFS data collected for the Fe^{IV}–oxido complexes

		Complex		
		2	**3**	**4**
Fe–O	N	1	1	1
	R (Å)	1.65	1.67	1.67
	σ^2 (10^{-3})	2.34	1.36	3.18
Fe–N	N	4	4	4
	R (Å)	1.99	2.00	1.98
	σ^2 (10^{-3})	5.70	6.62	5.53
Fe–C	N	3	4	3
	R (Å)	2.85	2.95	2.94
	σ^2 (10^{-3})	5.75	2.41	1.63
Fe–P	N	3	3	3
	R (Å)	3.30	3.23	3.19
	σ^2 (10^{-3})	5.38	3.36	2.48
Fe–O_P	N	2	3	3
	R (Å)	3.72	3.59	3.46
	σ^2 (10^{-3})	3.32	4.05	4.71
GOF	E_0	-15.19	1.73	-4.63
	F	33	66	89
	F'	205	257	286

Since the EXAFS data cannot resolve changes in the Fe–O bond distances, we sought to analyze the series by Badger's rule, which is an empirical formula correlating bond length and vibrational frequency (Eq. 5.1), where r_{Fe-O} is the Fe–O bond distance, v_{Fe-O} is the Fe–O vibrational frequency, and C_{Fe-O} and d_{Fe-O} are constants determined by a training set used for fitting the correlation. Using the experimentally determined vibrational frequencies, we calculated the predicted associated bond lengths for **2**, **3**, and **4** using two sets of parameters: one developed by Green[204] (C_{Fe-O} = 55.702 and d_{Fe-O} = 1.003) and another more recently developed by Guo[198] (C_{Fe-O} = 56.692 and d_{Fe-O} = 1.038). While Green's model does consider both heme and non-heme systems, Gou's model uses our

$$r_{Fe-O} = \frac{C_{Fe-O}}{v_{Fe-O}^{2/3}} + d_{Fe-O}$$

Equation 5.1 Badger's Rule

group's compounds as his training set for analysis, making it more applicable for analysis the compounds in this study. For example, Gou's model predicted that the Fe–O vibration measured for **2** would have Fe–O bond length of 1.67 Å, while Green's model calculated a bond length of 1.63 Å, both values are within the same error from the experimental data fit at 1.65(1) Å. Gou's model holds in more reasonable agreement with the fits of the EXAFS data across the series of three Fe^{IV}–oxido compounds (Table 5.3).

Table 5.3 Badger's Rule Comparisions of Fe^{IV}–oxido bond lengths

Complex	Fe–O Bond Length (Å)	Experimental Fe–O Vibration (cm^{-1})	Calculated Fe–O Bond Length (Å) Guo[198]	Calculated Fe–O Bond Length (Å) Green[204]
2	1.65	843	1.67	1.63
3	1.67	822	1.68	1.64
4	1.67	817	1.69	1.64

Preliminary Studies with Protons.

Having analyzed that Group II redox-inactive metal ions do influence the properties of the Fe^{IV}–oxido unit, we sought to interrogate how protonation of $[Fe^{IV}poat(O)]^-$ would affect the Fe–oxido unit. We hypothesized two possibilities: 1) protonation of the oxido ligand to a hydroxido species (Figure 5.20A) or 2) protonation would produce a complex in which the proton interacts with not only the oxido ligand but also the oxygen atoms of the P=O moieties, much like the proposed structure of bound LA (Figure 5.20B and C). Several acids were tested to assess the pK_a of $[Fe^{IV}poat(O)(H)]$, which was bracketed between 7 – 9. (H^+ sources: $[H_3NPh]^+$(pK_a ~ 5 in THF); protonated 2,4,6-tris-methyl-pyridine (pK_a ~ 7 in DMSO); $[HDMAP]^+$(pK_a ~ 9 in DMSO); $[HDBU]^+$(pK_a ~ 12 in DMSO). All as isolated $[BF_4]^-$ salts.)

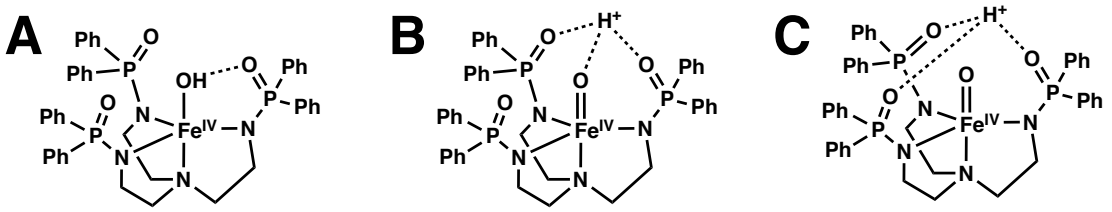

Figure 5.20 Possible protonation states of $[Fe^{IV}poat(O)]^{-}$.

Upon addition of one equivalent of H^+ ions, the UV-vis spectrum of $[Fe^{IV}poat(O)]^-$ showed loss of the 520 nm band and a shift in the low energy feature giving rise to a new species assigned as $[Fe^{IV}poat(O)(H)]^+$ (**5**) with at λ_{max}, nm = 370, 600 and 860 nm (Figure 5.21A). As expected, the addition of H^+ to $[Fe^{IV}poat(O)]^-$ was found to cause a change in both the EPR and Mössbauer parameters. In the ||–mode EPR spectrum there was growth of a signal at g = 8.01 with a larger intensity and broader line shape (fwhm = 60 G) than seen for the independent $[Fe^{IV}poat(O)]^-$, but weaker and narrower than seen with the addition of a Ca^{2+}(fwhm = 70 G) (Figure 5.21B). The E/D parameter was found to be 0.034(15), which is between the values for **2** and **3**, while no change was reflected in D value upon addition of H^+ ions. The fact that the D value remains the same throughout the addition of LA suggests that there is not a large change to the Fe^{IV}–oxido unit, which would negate the assignment of generating an Fe^{IV}–OH species upon protonation of $[Fe^{IV}poatO)]^-$. Addition of H^+ ions was reflected in the Mössbauer spectrum as a distinct doublet with parameters of δ = 0.05 mm/s and ΔE_Q = 0.85 mm/s, again remaining consistent with an Fe^{IV} center, albeit with an estimated yield of only ~50% (Figure 5.21C). The other 50% of the sample was found to be a ferric species that's identity is currently under investigation.

Preliminary data suggests that protons interact with the $[Fe^{IV}poat(O)]^-$ complex, however upon comparison of the parameters associated with **3** and **4,** compound **5** is very similar (Table 5.4). Two pieces of data that heavily negate the generation of an Fe^{IV}–OH

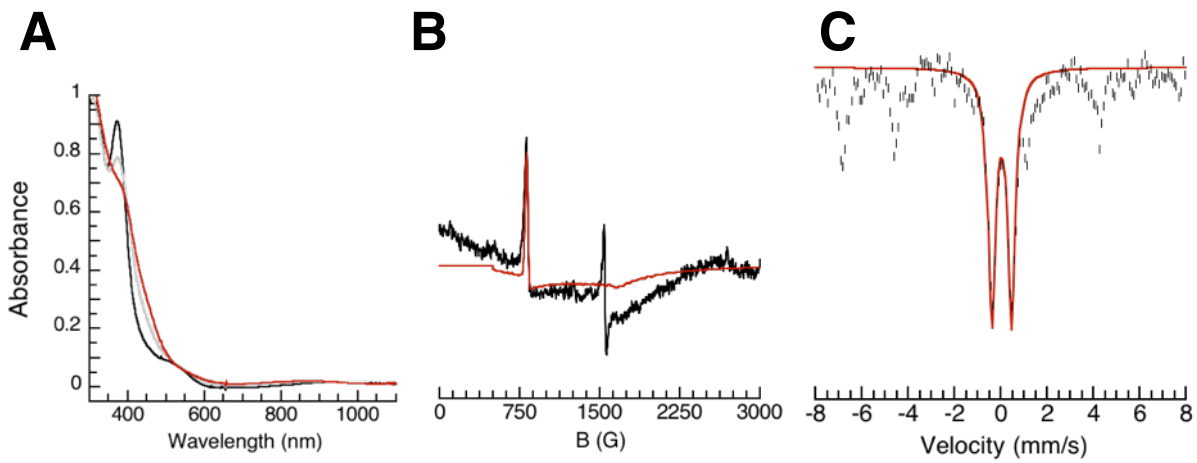

Figure 5.21 Electronic absorbance spectra (A) Inset: A zoom of the low energy region. EPR spectra (B) and Mössbauer spectra (C) of for the conversion of **2** (black) to **5** (red) in EtCN. Spectra recorded at 10 K for EPR and 4 K for Mossbauer in a DMF:THF mixture or EtCN, respectively, at – 80 °C.

species are: 1) **5** retained a low energy optical band and 2) the D value associated with **5** is identical to **2**. As previously mentioned, the low energy d–d transition is indicative of an Fe^{IV}–oxido species, and it is unclear that an Fe^{IV}–hydroxide complexes would retain this transition. Additionally, as discussed in the previous chapter, if an oxido ligand were to be protonated, it would be expected that the elongation of the Fe–O bond would be reflected in a decrease in the D value. Comparing to the data for the one-electron oxidized species of $[Fe^{III}H_2pout(OH)]^-$, this oxidized species was found to not have a low energy band or a positive D value, suggestive of species different than an Fe^{IV}–oxido complex. These data suggest that proton in **5** could be interacting with the complex through the P=O unit rather than protonating the oxido ligand (Figure 5.20B or C). In order to further interrogate the nature of **5**, additional experiments are currently under way including NRVS and XAS/EXAFS. In addition, attempts to prepare an Fe^{IV}–hydroxido species via a different synthetic route for comparison were also explored (see chapter 6).

Table 5.4 Summary of EPR and Mössbauer parameters of [Fepoat] complexes

Compound	*S*	λ_{max}[a]	*D*[b]	*E/D*	g	δ^c $\Delta E_Q{}^c$
1	2	N/A	N/A	N/A	9.44	1.02, 2.66
2	2	950	4.5	0.013(08)	8.02	0.086, 0.264
3	2	860	4.5	0.056(26)	8.07	0.029, 0.432
4	2	830	4.5	0.045(16)	8.01	0.014, 0.418
5	2	850	4.5	0.032(18)	8.01	0.05, 0.85

[a]nm (d–d transition); [b]cm^{-1} [c]mm/s

Summary and Conclusions

LA are often invoked as promoters for reactivity of high valent metal-oxido species, however knowing how the LA interacts with the metal-oxido complex, especially since the oxido itself is such a poor ligand for the cations, is difficult. To this end, a high spin Fe^{IV}–oxido complex was developed in the ligand framework $[poat]^{3-}$, which provides a secondary binding site for an auxiliary ion. A series of LA (LA = Mg^{2+}, Ca^{2+}, Sr^{2+}, Ba^{2+}, and H^+) were added to $[Fe^{IV}poat(O)]^-$ and generated distinct Fe^{IV} species. The Mössbauer data showed significant changes in the isomer shifts values of the Fe^{IV}–oxido complexes upon addition of LA, supporting that the LA is directly interacting with the oxdio ligand. The NRVS data shows a clear decrease in the Fe–O vibrations when Mg^{2+} or Ca^{2+} ions are added, corroborating that these ions affect the Fe^{IV}–oxido unit. Analysis by XAS and EXAFS suggested an elongation of the Fe–O bond length upon of addition of Mg^{2+} or Ca^{2+} ions; however, within the limits of the EXAFS experiments, there was no measurable difference

between the bond lengths for the Mg^{2+} and Ca^{2+} adducts. The use of Badger's rule showed that based on the NRVS data a small change in bond length should occur.

The data here in allows for the installation of a single LA within the complex framework such that it can interact with the Fe–oxido unit. In turn, having established a precedence that incorporation of an additional binding site can install the LA within the secondary coordination of the Fe–oxido unit allows for future reactivity studies. Utilizing the $[poat]^{3-}$ framework will allow for correlation of how a single LA interacting with the oxido ligand affects reactivity.

Experimental

General Procedures. All manipulations, unless otherwise stated, were completed under an argon atmosphere in a VAC drybox. Solvents were sparged with argon and dried over columns containing Q-5 and molecular sieves. All reagents were purchased from commercial suppliers and used as received unless otherwise noted. Potassium hydride as a 30% suspension in mineral oil was filtered and washed five times each with Et_2O and pentane and dried under vacuum. IBX-iPr[185,205], 15c5Ca$(OTf)_2$[68], 15c5Mg$(OTf)_2$[206], and amine based acids[76,207] were prepared according to literature procedures.

Physical Methods. Electronic absorption spectra were recorded in a 1 cm cuvette on an 8453 Agilent UV-Vis spectrometer equipped with an Unisoku Unispeks cryostat. X-band (9.28 GHz) EPR spectra were collected as frozen solutions using a Bruker EMX spectrometer equipped with an ER041XG microwave bridge. Mössbauer spectra were recorded with a Janis Research Super- Varitemp dewar. Isomer shifts are reported relative to Fe metal at 298 K. Negative mode electrospray ionization electrospray mass spectra were collected using a Micromass MS Technologies LCT Premier Mass Spectrometer. The

mass spectrum of [Fe^{IV}poat(^{16}O)]$^-$ and [Fe^{IV}poat(^{18}O)]$^-$ were collected at potentials of 2000V.

The ^{57}Fe nuclear resonance vibrational spectroscopy (NRVS) data were recorded using published procedures on multiple occasions at beamline 3-ID at the Advanced Photon Source (APS).[208,209] The incident flux provided by the beamline is ~2 x 109 photos/s in a 1 meV bandwidth centered at 14.4125 keV in a 1 mm (vertical) x 3 mm (horizontal) spot. The monochromators used in the experiment consisted of a water-cooled diamond (1,1,1) double crystal with 1.1 eV bandpass, followed by two separate Si(4,0,0) and Si(10,6,4) channel-cut crystals in a symmetric geometry. During the measurements, samples were maintained at low temperatures using a closed-cycle helium cryostat. The temperature for individual spectra were calculated using the ratio of anti-Stokes to Stokes intensity according to $S(-E) = S(E) \exp(-E/kT)$ and were generally in the range of 40 K to 80 K. Spectra were recorded between -40 meV and 120 meV in 0.25 meV steps.

Delayed nuclear fluorescence and iron K fluorescence (from internal conversion) were recorded with a single avalanche photodiode detector (APD) with 1 cm^2 detection area. Each scan required about 50 minutes, and all scans were added and normalized to the intensity of the incident beam. The ^{57}Fe partial vibrational density of state (PVDOS) was extracted from the raw NRVS data using the PHOENIX software package.[210]

XAS experiments were performed at the Stanford Synchrotron Radiation Laboratory (SSRL) on beam line 7-3 at 13 K. Fe K-edge data was collected using a Si(220) φ=0° double-crystal monochromator with a 9.0 keV cutoff for harmonic rejection. Data was collected in fluorescence mode with a Canberra 30-element Ge solid- state detector. To limit photoreduction of the samples, only first scans were averaged into the final data sets

(exposure time ~35 minutes). Fe K-edge data for the both all species was comprised of 7 first scans. Energies were calibrated using an iron foil (7111.2 eV) and edge energies were obtained from the first derivative of the data with 1.0 eV smoothing and a third order polynomial in the program EXAFSPAK.[211]

The Fe K-edge data sets were fit over the region k = 3-14 Å-1 using EXAFSPAK[211] with *ab initio* phases and amplitudes generated with the program FEFF v8.40.[212] The Fe K-edge fits for the three iron species were comprised of the first, second, third, fourth, fifth shell atoms. All Debye-Waller factors were treated as free parameters. The scale factor, S_0, was set to 0.9. Monochromator glitches in the Fe K-edge data sets at approximately k = 12.5 Å-1 were removed using a cubic polynomial fit to the data. No other modifications to the raw data were performed.

Ligand Synthesis.

H_3poat. Described in Chapter 2

Complex Synthesis.

K[Fe^{II}poat]. To a solution of H_3poat (200 mg, 0.269 mmol) in anhydrous THF (6 mL) was added potassium hydride (KH) (33 mg, 0.81 mmol) and the reaction allowed to proceed until gas evolution ceased and all solids were dissolved. To the light yellow solution was added Fe^{II}(OAc) (47 mg, 0.26 mmol). The solution was stirred for 25 minutes and then filtered through a medium fritted glass funnel to remove insoluble material. Light yellow crystals (208 mg, 93%) are afforded by vapor diffusion or layering of diethyl ether (Et_2O) into or on top of the solution of THF. EPR (X-band Parallel, DMF:THF, 10 K, g = 9.44) Mossbauer (DMF:THF, 4K, δ= 1.02 mm/s; ΔE_Q = 2.66 mm/s)

Low-temperature Solution studies using [Fe^{II}poat]$^{-\cdot}$ In a typical experiment, a 20 mM solution of K[Fe^{II}poat] (17 mg, 0.020 mmol) with 18-crown-6 ether (11 mg, 0.042 mmol) added to increase solubility was prepared in the desired solvent (1 mL) at room temperature and kept in a – 35 °C freezer for the duration of the experiment. Addition, via air tight syringe, of a 20 μL aliquot of stock metal complex to the solvent mixture (2 mL) in a 1 cm quartz cuvette, which was sealed with a rubber septum and precooled to the desired temperature in the 8453 Agilent UV−vis spectrophotometer equipped with an Unisoku Unispeks cryostat, to give the desired concentration for oxidation experiments (0.2 mM). The solution of metal complex was allowed to equilibrate to the desired temperature for at least 15 min. Stock solutions of other reagents prepared to between 20 and 50 mM in the same solvent and added via gas-tight syringe to an aliquot of (18c6)$_2$K[Fe^{II}poat]. Reactions were monitored spectrophotometrically either by UV-vis or EPR spectroscopies. Mössbauer samples were prepared in an analogous manner using 95% ^{57}Fe-enriched K[Fe^{II}poat].

Preparation of Low-Temperature Solution NRVS Samples. Solution NRVS sample holders were prepared from Mössbauer sample holders by cutting a 2 x 6 mm slot out of the bottom and covering the hole with kapton tape. A 40 mM solution of 96% ^{57}Fe-enriched [Fe^{II}poat]$^-$ (34 mg, 0.041 mmol) was prepared in a DMF:THF mixture (1 mL) with 18-crown-6 ether (22 mg, 0.083 mmol) added to increase solubility. The A NRVS sample holder was cooled in the cold well of a drybox to −196 °C. Additionally, a stock solution of IBX-iPr (40 mM) was prepared in 2:1 DMF:THF mixture and kept in a – 80 °C cold well for the duration of the experiment. An aliquot of (18c6)$_2$K[Fe^{II}poat] (300 μL) was added to one equivalent of IBX-iPr (300 μL). To the pre-cooled NRVS sample holder, a sample of

$[Fe^{IV}poat(O)]^-$ (500 μL of the 20 mM solution) was added via syringe and allowed to freeze completely. The sample was then transferred from the dry box and quickly placed in a storage container pre-cooled to 77 K. Samples were analyzed for purity using Mössbauer spectroscopy prior to NRVS data collection. Analogous preparation was followed for **3** and **4** with the subsequent addition of 15c5Ca$(OTf)_2$ (100 μL, M) or 15c5Mg$(OTf)_2$ (100 μL, M), respectively.

Preparation of Low-Temperature Solution XAS Samples. Solution XAS samples were prepared in a similar manner as solution NRVS samples described above with the following modifications: a 20 mM solution of $[Fe^{II}poat]^-$ (34 mg, 0.041 mmol) of which 2 mM was prepared with 96% ^{57}Fe-enriched $[Fe^{II}poat]^-$, was prepared in a DMF:THF mixture (2 mL) with 18-crown-6 ether (22 mg, 0.083 mmol) added for increase solubility. Samples were analyzed for purity using Mössbauer spectroscopy prior to XAS data collection. Analogous preparation were followed for **3** and **4** with the subsequent addition of 15c5Ca$(OTf)_2$ (100 μL, M) or 15c5Mg$(OTf)_2$ (100 μL, M), respectively. Solution XAS sample holders were prepared from Mössbauer sample holders by cutting off the bottom and covering the hole with kapton tape.

Labelling Studies.

Preparation of ^{18}O Labeled Samples. $H_2{}^{18}O$ (50 μL, 2.7 mmol) was added to a solution of ^{16}O IBX-iPr (0.013 g, 0.040 mmol) in D_3COD (1 mL) and stirred for 30 mins. All volatiles were removed in vacuo. The residue was redissolved in D_3COD (1 mL) and treated with a second iteration of $H_2{}^{18}O$ (50 μL, 2.7 mmol), stirred for an additional 30 mins and then reduced under pressure to a white solid that was used without further purification. $[Fe^{IV}poat(^{18}O)]^-$

was prepared according to the low temperature procedure above in which the ^{18}O source was ^{18}O IBX-iPr.

CHAPTER 6

g = 10

In chapter 5, the starting synthon $[Fe^{II}poat]^-$ was employed to generate a high spin Fe^{IV}–oxido (**2**) complex. This well-characterized complex was subsequently treated with a variety of Lewis Acids (LA), including protons, leading to the generation of distinct Fe^{IV} complexes that have the LA bound through the oxygen atoms of the P=O units and/or interacting with the Fe–oxido unit. One compound from the study of interest is the protonated species (**5**), specifically whether or not an Fe^{IV}–hydroxido complex was formed upon addition of a proton. Determining the composition of the **5** is complicated due to the lack of sufficient evidence to identify exactly where the proton resided on the complexes, considering the following possibilities: 1) protonation of the oxido ligand (Figure 6.1A) or 2) the proton rather sits just above the cavity, binding the oxygen atoms of the P=O units and minimally interacting with the metal-oxido unit (Figure 6.1B) or not at all (Figure 6.1C), as suggested for the larger LA.

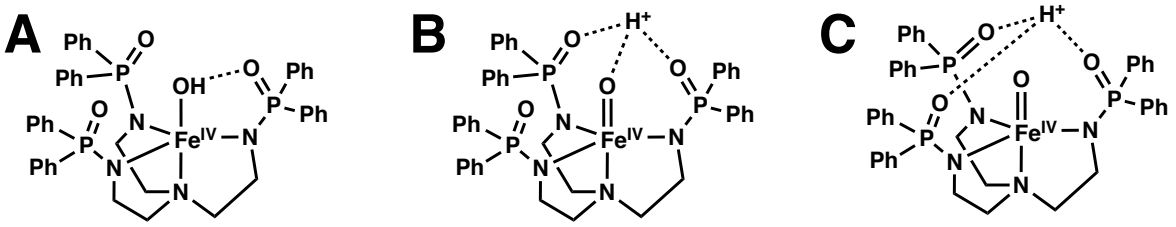

Figure 6.1 Possible sites of protonation on Fe^{IV}–O complex.

Given the D value of **5** (4.5 cm^{-1}) was the same value as in the with that of the pure Fe^{IV}–oxido complex, the data supports that the proton is not interacting with the oxido ligand. As previously discussed, it would be expected that if protonated the "Fe^{IV}–OH" species would be expected to show a major change in its D value. This chapter explores

generating an Fe^{IV}–OH species within $[poat]^{3-}$ by a different route. Taking advantage of the versatility of $[Fe^{II}poat]^-$, attempts to prepare an Fe^{IV}–hydroxido are performed via oxidation of its Fe^{III}–OH complex (Scheme 6.1, Route B). The low valent Fe^{II}–OH_2, Fe^{II}–OH and Fe^{III}–OH complexes were prepared and structurally characterized. The one-electron oxidation of the Fe^{III}–OH complex was monitored by several spectroscopic methods including UV-vis, ||–mode EPR, Mössbauer, NRVS spectroscopies.

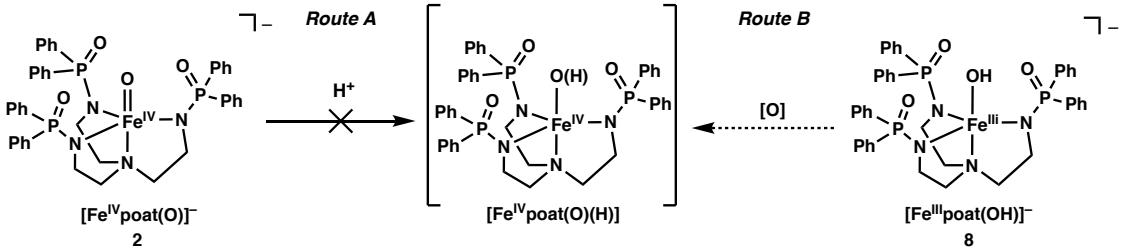

Scheme 6.1 Synthetic attempt for preparation of Fe^{IV}–O(H) complex.

Results and Discussion

Synthesis. Addition of one equivalent of water to the starting complex $[Fe^{II}poat]^-$ (**1**) allowed for the isolation of the corresponding $[Fe^{II}poat(OH_2)]^-$ complex (**6**). The aqua ligand was subsequently deprotonated with one equivalent of base to yield the low valent $[Fe^{II}poat(OH)]^{2-}$ species (**7**). One-electron oxidation of the Fe^{II}–OH complex with half an equivalent of elemental iodine gave the related Fe^{III}–OH species, $[Fe^{III}poat(OH)]^-$ (**8**) (Scheme 6.2).

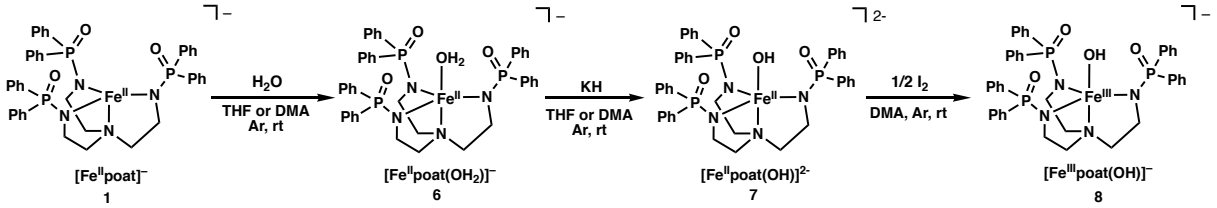

Scheme 6.2 Preparation of Fe–OH_X complexes.

Structural Properties. The molecular structures of crypt-222K[Fe^{II}poat$(OH)_2$], K_2[Fe^{II}poat(OH)], and K[$Fe^{III}H_2$pout(OH)] salts were characterized with X-ray diffraction (XRD) methods (Figure 6.2, Tables 6.1and 6.2). All three complexes were found to be mononuclear Fe–OH_x species (X = 2 for **6** and 1 for **7** and **8**) within the asymmetric unit. The Fe centers each sit in a distorted tbp coordination geometry. The primary coordination spheres around the Fe centers are composed of a N_4O donor set with three anionic N-atom donors forming the trigonal plane. The axial positions contain the apical amine N1-atom from the $[poat]^{3-}$ ligand and O1–atom from the aqua/hydroxido ligand. There is a shorten in the Fe^{II}–O1 bond length in **6** versus **7** from 2.150(2) Å to 2.032(8) Å consistent with related Fe^{II}–OH_2, Fe^{II}–OH complexes in trigonal symmetry.[98,213] There is a significant

Table 6.1 Crystallographic Data and Structure Refinement Parameters for **6**, **7**, and **8**

Complex	Crypt-222 K[Fe^{II}poat(OH_2)] **6**	K_4[Fe^{II}poat(OH)]$_2$ **7**	K_2[Fe^{III}poat(OH)]$_2$ **8**
Empirical Formula	C_{60} H_{80} Fe K N_6 O_{10} P_3	C_{100} H_{118} Fe_2 K_4 N_8 O_{12} P_6	C_{84} H_{86} Fe_2 K_2 N_8 O_8 P_6
Formula weight	1233.16	2077.94	1711.32
Crystal system	Triclinic	Triclinic	Monoclinic
Space group	$P\bar{1}$	$P\bar{1}$	$P2_1/c$
a (Å)	14.0676(12)	13.4005(17)	15.8093(12)
b (Å)	15.5743(14)	14.5096(19)	14.4288(11)
c (Å)	16.6439(15)	14.6020(19)	19.8831(15)
α (°)	67.3004(11)	98.6992(16)	90
β (°)	82.3762(12)	106.9916(16)	111.1598(9)
χ (°)	64.3286(10)°	105.8621(15)	90
Volume (Å^3)	3029.4(5)	2528.1(6)	4229.7(6)
Z	2	1	2
δcalc (Mg/m3)	1.352	1.365	1.344
GOF	1.021	1.038	1.063
R1	0.0414	0.0286	0.0294
wR2	0.1065	0.0743	0.0786

decrease in the length of Fe1–O1 to 1.896(9) Å in the Fe^{III}–OH, which is reflective of oxidation at the metal center.[124]

Table 6.2 Selected Bond Distances and Angles for **6**, **7**, and **8**.

Bond Distances (Å) or Angles (˚)	222,cryptK[Fe^{II}poat(OH_2)] **6**	K_4[Fe^{II}poat(OH)]$_2$ **7**	K_2[Fe^{III}poat(OH)]$_2$ **8**
Fe(1)-O(1)	2.1496(15)	2.0318(8)	1.8961(9)
Fe(1)-N(2)	2.1085(17)	2.1408(9)	2.0034(11)
Fe(1)-N(4)	2.0680(17)	2.1209(9)	2.0042(11)
Fe(1)-N(3)	2.0887(16)	2.1223(9)	2.0256(11)
Fe(1)-N(1)	2.2790(17)	2.3444(9)	2.3734(11)
O1…O2	2.677(2)	--	--
O1…O3	2.720(2)	--	--
O(1)-Fe(1)-N(2)	94.48(6)	90.29(3)	105.69(4)
O(1)-Fe(1)-N(4)	108.35(7)	103.27(3)	101.44(4)
N(2)-Fe(1)-N(4)	124.22(7)	124.05(4)	113.33(4)
O(1)-Fe(1)-N(3)	96.92(7)	114.80(3)	99.42(4)
N(2)-Fe(1)-N(3)	114.46(7)	116.28(4)	118.96(5)
N(4)-Fe(1)-N(3)	112.32(7)	106.46(4)	114.67(5)
O(1)-Fe(1)-N(1)	171.01(6)	165.36(3)	175.84(4)
N(2)-Fe(1)-N(1)	79.31(6)	77.51(3)	78.16(4)
N(4)-Fe(1)-N(1)	80.59(6)	77.66(3)	78.15(4)
N(3)-Fe(1)-N(1)	80.01(6)	78.33(3)	77.13(4)

Examining the features within the secondary coordination sphere, both **7** and **8** have interactions between the oxygen atoms of the phosphinic amide moieties and the potassium counter ion(s) (Figure 6.2C and 6.2D) The interactions with K^+ ions disrupts the anticipated H-bond interactions between the O–atoms of the P=O moieties and the hydroxido units in the solid state. In the molecular structure of **6,** the K^+ ion is sequester in a chelating agent (2.2.2-cryptand) (Figures 6.2A). Encapsulation of the K^+ ion allows for the two of the P=O oxygen atoms to participate in intramolecular H-bonding with the aqua

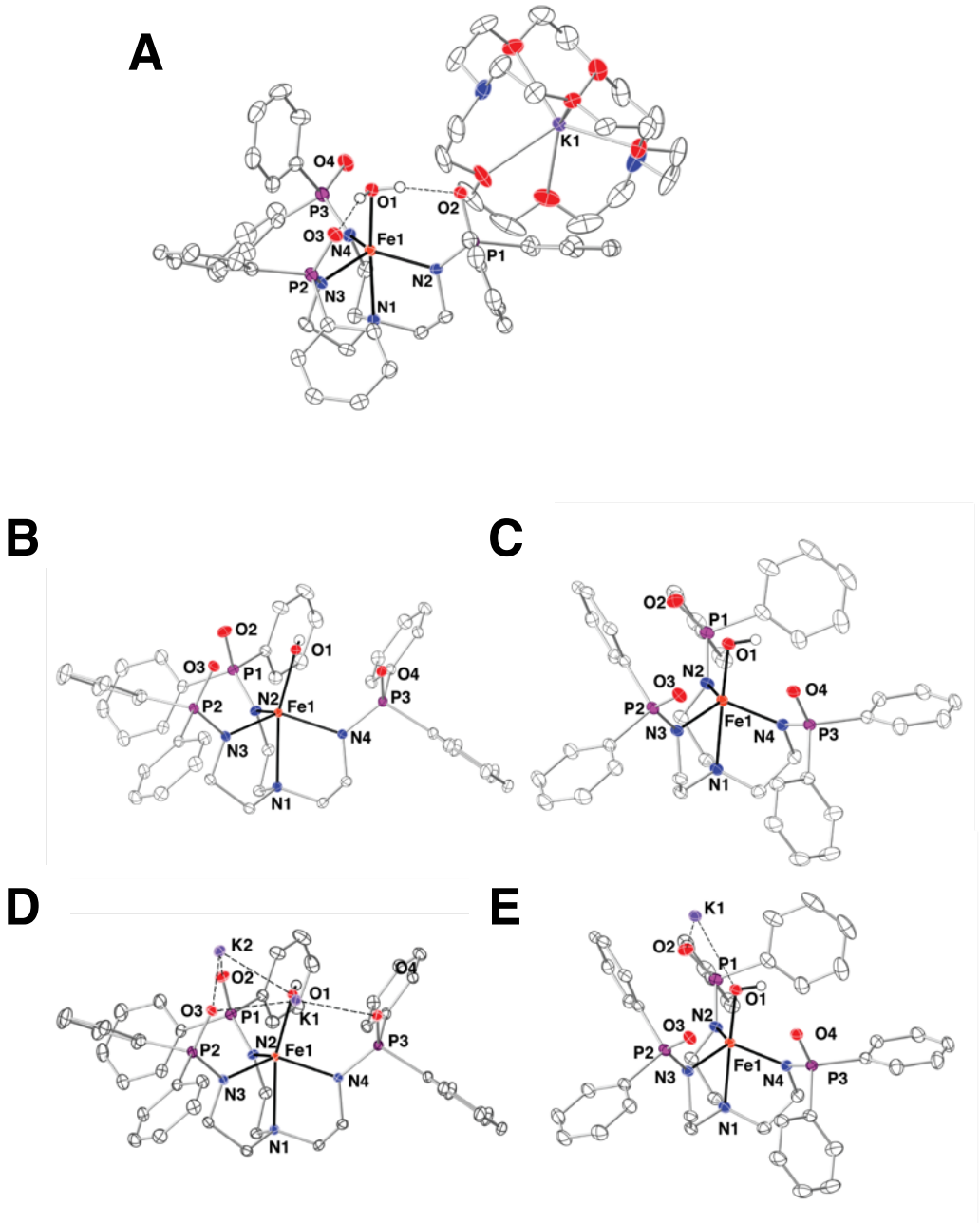

Figure 6.2 Thermal ellipsoid plots of $[Fe^{II}poat(OH_2)]^-$ (**A**), $[Fe^{II}poat(OH)]^{2-}$ (**B**), $[Fe^{III}poat(OH)]^-$ (**C**) $K_2[Fe^{II}poat(OH)]$ (**D**), $K[Fe^{III}poat(OH)]$ (**E**). Thermal ellipsods are drawn at the 50% probability level, only hyrdoxido hydrogen atoms are shown for clarity.

ligand at distance of 2.677(2) Å and 2.720(2) Å for O1···O2 and O1···O3, respectively. Similar structural results were found for aqua compounds within the sulfonamido frameworks. For example, $[Fe^{III}PST(OH_2)]^-$, ($[PST]^{3-}$ is a derivative of the sulfonamido

ligand series, where the mesityl is $[MST]^{3-}$ is replaced by a phenyl ring), showed the presence of two intramolecular H-bonds between the the exogenous water ligand and sulfonamido O-atoms at distances of 2.697(1) Å and 2.676(1) Å.[213]

Electrochemical Properties. Cyclic voltammetry (CV) was employed to analyze the redox properties of the Fe–OH complexes. Electrochemical data showed a reversible one-electron redox couple at – 1.76 V vs $[FeCp_2]^{+/0}$ that is assigned to the $Fe^{III/II}$–OH process (Figure 6.3), which is consistent with the $Fe^{III/II}$ couple found in $[Fe^{III}H_3buea(OH)]^-$ that occurs at – 1.79 V vs $[FeCp_2]^{+/0}$.[124] A second redox event was observed at a more potential of – 0.98 V vs $[FeCp_2]^{+/0}$. At first this event was thought to be an $Fe^{IV/III}$ event, however it appears at a much potential more negative potential than the $Fe^{IV/III}$ seen for $[Fe^{III}H_3buea(OH)]^-$ (0.34 V vs $[FeCp_2]^{+/0}$). One defining feature of the cyclic voltammogram is that while the second

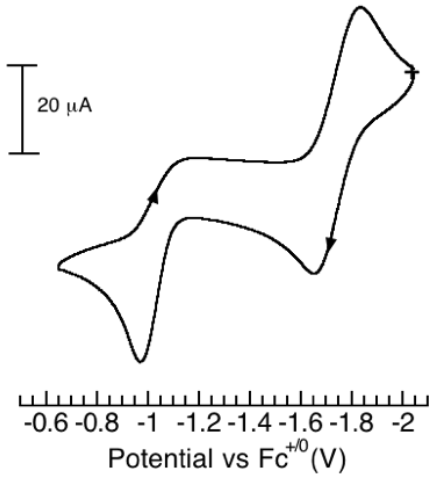

Figure 6.3 Cyclic voltammograms of $[Fe^{II}poat(OH)]$ recorded in DMF. Measurement was done at room temperature under Ar with a scan rate of 100 mV s^{-1}.

redox event is irreversible, the return current is retained for the $Fe^{III/II}$ couple. If the two processes were from the same species, it would be expected that if the second redox event did not have cathodic current then the reversibility of the $Fe^{III/II}$ couple would be affected.

One possibility is that the two events are attributed to different compounds, one for the $Fe^{III/II}$–OH coupled and the other for perhaps $Fe^{III/II}$–OH_2 or $Fe^{III/II}$ empty cavity complexes. Studies are underway to probe the presence of multiple species. Along this effort, [Fe^{III}poat] (**9**) has been isolated and structural characterized (Figure 6.4A). The chemical potential for the $Fe^{III/II}$ empty cavity was collected by Chen Sun and found E_0= – 1.053 V vs $[FeCp_2]^{+/0}$ in a DMF:THF mixture. Additionally, there is preliminary spectroscopic data to show that **6** can be oxidized by one electron using a mild oxidant, $FcBF_4$, to give a S = 5/2 species that is distinct from Fe^{III} and Fe^{III}–OH (Figure 6.4B and 6.4C).

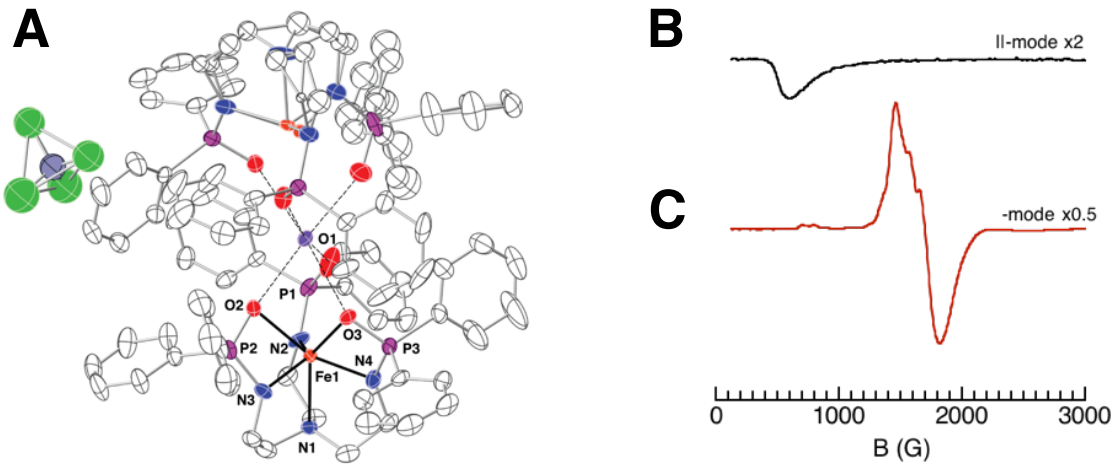

Figure 6.4 Thermal ellipsoid plots of [KBF_4][Fe^{III}poat], **9** (**A**). EPR spectra of **6** (**A**) and **6** + $FcBF_4$ (**B**) at – 80 °C in a DMF:THF mixture. Recorded at 10 K in a DMF:THF, respectively.

Magnetic Properties. Both the Fe^{II}–OH and Fe^{III}–OH complexes were analyzed by EPR and Mössbauer spectroscopies. Addition of either 18-crown-6 ether (18c6) or 2.2.2-cryptand (2.2.2.-crypt) was added to increase solubility. Analysis of the Mössbauer parameters for 18c6-**7** showed values of δ = 1.04 mm/s and ΔE_Q = 3.07 mm/s consistent with a high spin Fe^{II} center (Figure 6.5A). The corresponding EPR spectra of 18c6-**7** were silent in both

modes. Evaluation of the Mössbauer spectrum of 2.2.2.crypt-**8** showed a 6-line magnetic spectrum indicative of a high spin Fe^{III} complex with parameters of δ = 0.331 mm/s and ΔE_Q = 0.856 mm/s, consistent with previously report Fe^{III}–OH species (Figure 6.5B).[180] An additional ferric species was present in the spectrum and has been quantified to make up approximately 20% of the sample. The identity of the ferric impurity is no known. The impurity is of interest because the Mössbauer samples are prepared as a frozen solution of recrystallized material, suggesting the Fe^{III}–OH complex is not stable in solution. Preparation and analysis of a Mössbauer sample with solid material would be necessary to corroborate this hypothesis. The EPR spectrum of 2.2.2.crypt-**8** revealed a highly rhombic species with g values of 9.57 and 4.30. The zero-field splitting term (D) and rhombicity term (E/D) values were determined to be – 1.53 cm^{-1} and 0.27, respectively, which are consistent values from both $[Fe^{III}H_3buea(OH)]^-$ and $[Fe^{III}H_2pout(OH)]^-$.[180]

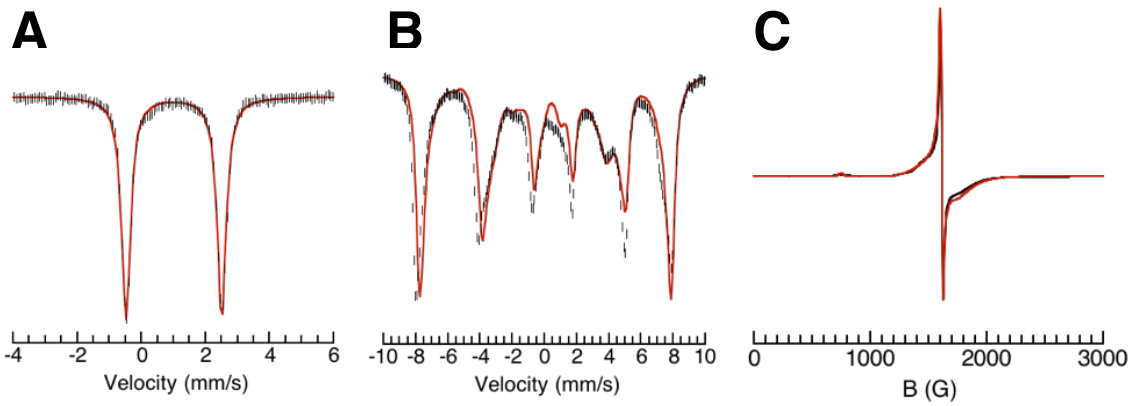

Figure 6.5 Mössbauer spectra of 18c6-**7** (**A**) and 2.2.2.crypt-**8** (**B**) at – 80 °C in a DMF:THF mixture. EPR spectrum of 2.2.2.crypt-**8** (**C**). Recorded at 4 K and 10 K in a DMF:THF, respectively. Red lines are simulations of the experimental data.

Oxidation beyond $[Fe^{III}poat(OH)]^-$ at Low Temperatures. To evaluate if an oxidation can be accessed at low temperatures the following studies were performed. The starting complex for these studies was either the $[Fe^{II}poat(OH)]^{2-}$ (**7**) or $[Fe^{III}poat(OH)]^-$ (**8**), in the presence

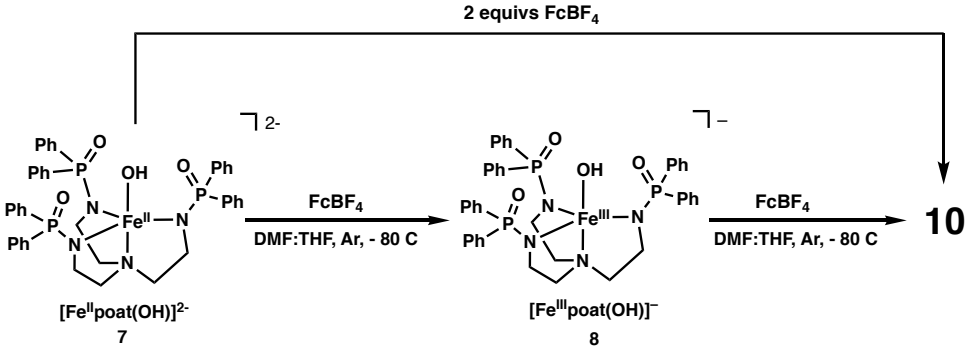

Scheme 6.3 Oxidation of Fe–OH complexes.

of 18c6 to increase solubility. Treatment of 18c6-**7** with two equivalents or 18c6-**8** with one equivalent of ferrocenium tetrafluoroborate ($FcBF_4$), in a mixture of DMF:THF at low temperatures generates the same oxidized species, **10**, (Scheme 6.3). Monitoring of the reaction spectrophotometrically showed growth of a new species with peaks at λ_{max} = 350,

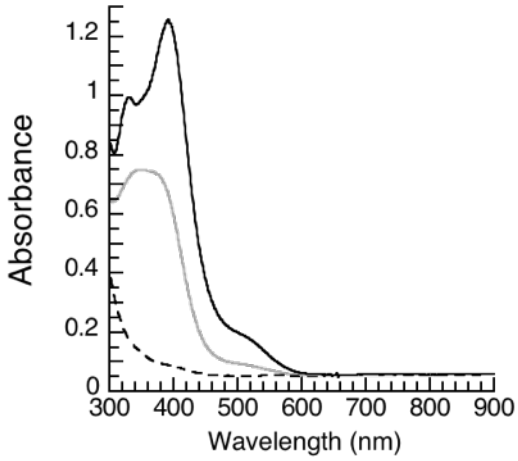

Figure 6.6 UV-vis spectra of **7** (black dashed), **7 + Fc**$^+$ (gray solid), and **7 + 2Fc**$^+$ (black solid). Recorded at – 80 °C in a DMF:THF.

385 and 520 nm (Figure 6.6), (**10**). Examining this reaction using EPR spectroscopy showed growth of a new strong derivative signal in the ||–mode spectrum at g = 10.6 (Figure 6.7A). The shape and g-value of this signal were unprecedented, but found to be consistent with an S = 2 system. The curious nature the EPR spectrum initially led to

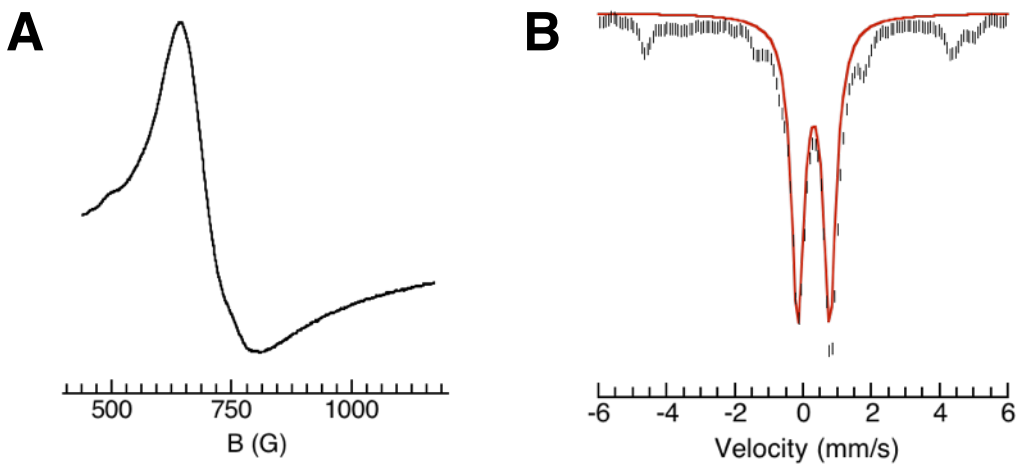

Figure 6.7 EPR (**A**) and Mössbauer (**B**) spectra of **10**. Recorded at 10 K and 4 K, respectively, in a DMF:THF. Red lines are the least-squares fits of the experimental data

suggest that **10** could be an Fe^{IV}-OH species; however, unexpected results for the Mössbauer parameters of **10** were obtained of $\delta = 0.332$ mm/s and $\Delta E_Q = 0.989$ mm/s, which are consistent with an Fe^{III} center, not an Fe^{IV} center (Figure 6.7B). The presence of an Fe^{III} center, but an EPR signal for an S=2 species suggested a spin coupled system. In addition to **10**, the Mössbauer spectrum revealed the presences of two other ferric species. At this time, data suggests one to be the empty cavity Fe^{III} complex and the other to be residual Fe^{III}–OH.

These results prompted more EPR studies including temperature dependent experiments that showed two signals, which were from the ground state (S = 2) and excited state (S = 3) of the same species with a J value of 2 cm^{-1}. These data supported an antiferromagnetically coupled system between an Fe^{III} center, S = 5/2, and a ligand radical, S = ½ (Figure 6.8). Additionally, the EPR data revealed a zero-field splitting term of a negative value, D = - 3 cm^{-1}. The negative D value for **10** is consistent with previously reported Fe^{III}–OH species, however the magnitude of D is much larger than that for the

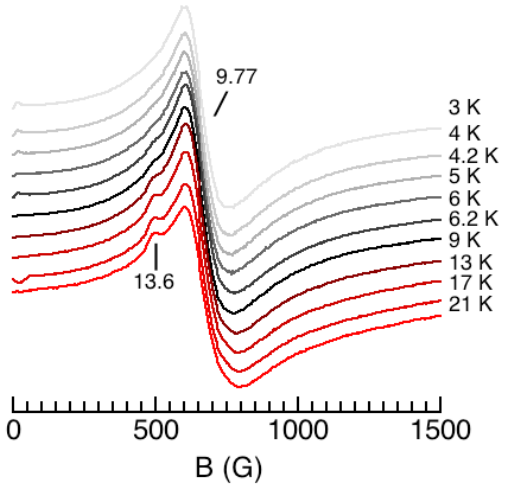

Figure 6.8 Variable temperature EPR spectra of 10 collected from 3 K to 21 K.

characterized $[Fe^{III}poat(OH)]^-$. Additionally, the Mössbauer spectra of **8** and **10** are different, with **8** having a magnetic spectrum.

Vibrational Properties. Analysis of vibrational properties using FTIR spectroscopy showed bands attributed to the ν(FeO–H) at 3631 and 3560 cm^{-1} for **7** and **8**, which are within agreement with FeO–H vibrations of previously characterized Fe–OH species.[124] Due to the arrangement of the potassium ions with the complexes (Figure 6.3D and 6.3E) it is not possible to directly compare the interactions in the secondary coordination sphere of the compounds with other Fe–OH species.

To further evaluate the nature of **10**, we employed nuclear resonance vibration spectroscopy (NRVS) to interrogate the Fe–O vibration. The NRVS spectrum of **10** revealed one higher energy peak at 612 cm^{-1} (Figure 6.9A). A vibration at 612 cm^{-1} is significantly lower than vibrations attributed to Fe^{III}–oxido stretch of $[Fe^{III}H_3buea(O)]^{2-}$, which is assigned at 663 cm^{-1},[198] but is also higher in energy than the two observed vibrations for **8** (Figure 6.9B). Examining Fe–O vibrations previously characterized for high spin Fe^{III}

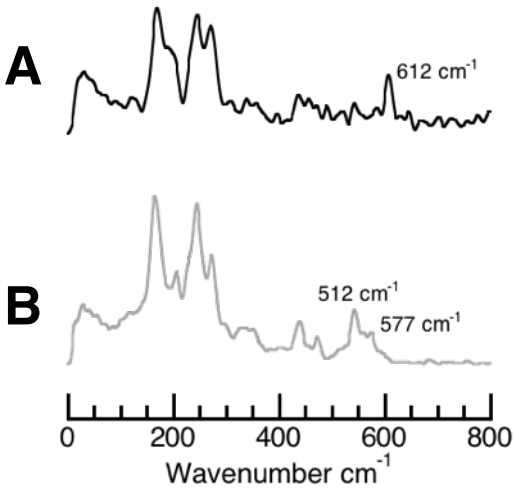

Figure 6.9 NRVS spectra for **10** (A), and **7** (B). Samples were ~25 mM in a DMF:THF mixture. The peaks for the Fe–O vibrations are labelled with their corresponding energies.

species, the vibration of **10** falls within range of Fe–OO(X) species. For example, Que and coworkers reported a ν(Fe–O) for their high spin non-heme Fe^{III}–alkylperoxo complexes approximately 620 cm^{-1}.[214] How an O–O adduct may be formed in **10** is discussed below. It also must be made evident that key to proving or disproving the presence of an O–O bond would be further evaluation of vibrational properties of the complex by resonance Raman (rR) spectroscopy.

*Proposals for the Identity of **10***

Given the current observations, several proposals are possible for the identity of **10**. Perhaps the least provocative assessment would be that the system is simply an Fe^{III}–OH complex with a ligand radical, possibly delocalized amongst the O=P–N unit (Figure 6.10); however, the cyclic voltammetry data does not support that oxidation of the ligand would occur with such a mild oxidant such as ferrocenium. Additionally, the NRVS data shows an Fe–O vibration that is higher in energy than any of our characterized Fe^{III}–OH species.[198] It is also worth noting that both the EPR and vibrational data do not support the formation of

an Fe^{III}–oxido complex. For example, $[Fe^{III}H_3buea(O)]^{2-}$ has a D value of – 0.7 cm^{-1},[180] while **10** has a D value of – 3 cm^{-1} as noted above.

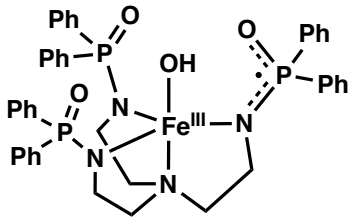

Figure 6.10 Chemdraw depiction of **10** as an Fe^{III}–OH ligand radical species.

Another intriguing hypothesis is that **10** could be an Fe^{III}–OO(H) species. Details for this proposed chemistry are illustrated in Figure 6.11. After oxidation of the Fe^{III}–OH, forming a transient Fe^{IV}–OH species, an intramolecular proton transfer could occur to one of the oxygen atoms of the P=O units of $[poat]^{3-}$ due to its relatively high basicity (Scheme 5.6, Compound **B**). Support for this possible proton transfer step comes from work done on the oxidation of n-butane by vanadium phosphorus oxides.[215,216] The basicity of the P=O unit has been suggested as a critical component in this process. In a theoretical study,

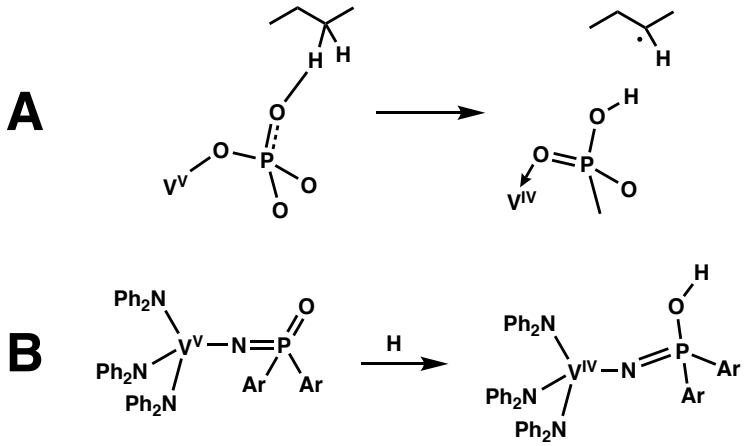

Scheme 6.4 Proposed mechanism for C–H bond activation of butane from theoretical studies by Goddard (**A**). Proposed mechanism for molecular model used by Menard (**B**).

Goddard and coworkers studied the mechanism of n-butane oxidation and reported that the strong basicity of the P=O unit coupled with the reduction potentials of the V^V ion were

responsible for the initial C–H bond cleavage (Scheme 6.5A).[215] In recent reports, Ménard and coworkers provide experimental evidence that supported Goddard's claims of the phosphate oxide is critical in initiating the C–H bond activation in butane (Scheme 6.5B).[216]

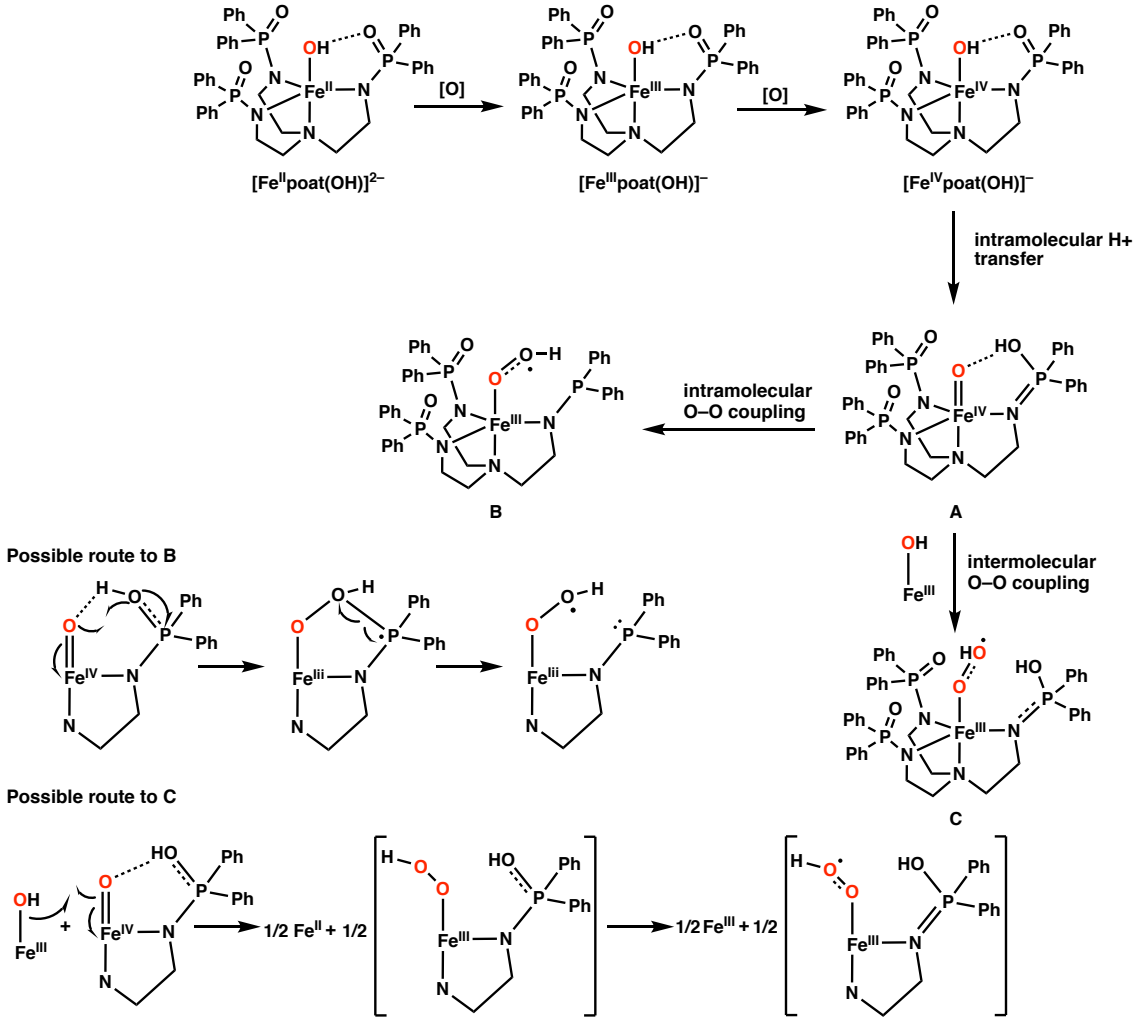

Figure 6.11 Proposed reaction sequences to form an Fe^{III}–OO(H) species.

After proton transfer, O–O coupling could presumably happen either intra- or inter-molecularly. Product **B** would occur from an intramolecular processes. Compound **B** could result from reactivity of the Fe^{IV}–oxdio unit and the protonated P=O unit (Figure 6.11, Route to B). The other possibility is for similar chemistry to occur between two separate complexes. The evidence for reactivity between the tentative Fe^{IV}–oxido complex and

another [Fe^{III}poat(OH)]$^-$ (**8**) complex is suggested from the apparently instability of **8** in solution and the presence of empty cavity [Fe^{III}poat] in the Mössbauer spectrum of **10** (Figure 6.11, Route to C).

Table 6.3 Summary of EPR and Mössbauer parameters of [Fe^{n+}poat(OH_x)]^m complexes

Compound	*S*	*D*[a]	*E/D*	g	δ [b] ΔE_Q[b]
1	2	--	--	9.44	1.02, 2.66
6	2	--	--	11.05	1.05, 3.15
7	2	--	--	-	1.04, 3.07
8	5/2	– 1.27	0.232	9.57, 4.30	0.334, 0.897
9	5/2	– 1.78	0.31	7.01, 5.52, 3.27	0.339, 1.098
10	2	– 3	--	13.6, 10	0.332, 0.989

[a]cm^{-1}; [b]mm/s

Summary

The beginning of this chapter discussed the preparation and characterization of low valent Fe–aqua/hydroxido complexes within $[poat]^{3-}$ scaffold. The $Fe^{II/III}$–OH complexes have similar properties as both the $[H_3buea]^{3-}$ and $[H_2pout]^{3-}$ frameworks; however, once oxidized beyond Fe^{III}–OH, the reactivity is different. The formed compound (**10**) exhibits magnetic properties that are unprecedented to anything we have seen before and has been assigned as an S = 2 system containing a high spin Fe^{III} center antiferromagnetically coupled to a ligand radical. Additional work is needed in order to understand the identity of **10**, and how it is formed. This chapter begins to develop a foundation for further investigation of the coupled system.

Experimental

X-ray Crystallographic Methods. A Bruker SMART APEX II diffractometer was used to collect all data. The APEX2[148] program package was used to determine the unit-cell parameters and for data collections. The raw frame data was processed using SAINT[149] and SADABS[150] to yield the reflection data files. Subsequent calculations were carried out using the SHELXTL[217] program. The structures were solved by direct methods and refined on F2 by full-matrix least-squares techniques. The analytical scattering factors7 for neutral atoms were used throughout the analysis.

Hydrogen atoms H(1) and H(2) for 222,cryptK[Fe^{II}poat(OH_2)] were located from a difference-Fourier map and refined (x,y,z and U_{iso}). The remaining hydrogen atoms were included using a riding model.

Hydrogen atom H(1) for $K_4[Fe^{II}poat(OH)]_2$ was located from a difference-Fourier map and refined (x,y,z and U_{iso}). The remaining hydrogen atoms were included using a riding model. The molecule was located about an inversion center.

Hydrogen atom H(1) for $K_2[Fe^{III}poat(OH)]_2$ was located from a difference-Fourier map and refined (x,y,z and U_{iso}) with d(O-H) = 0.85Å. The remaining hydrogen atoms were included using a riding model. The molecule was located about an inversion center. There were several high residuals present in the final difference-Fourier map. It was not possible to determine the nature of the residuals although it was probable that diethylether solvent was present. The SQUEEZE[218] routine in the PLATON[218] program package was used to account for the electrons in the solvent accessible voids.

Hydrogen atoms for $[Fe^{III}POAT]_2$•KBF4 were included using a riding model. Several

atoms were disordered and included using multiple components with partial site-occupancy factors. There were several high residuals present in the final difference-Fourier map. It was not possible to determine the nature of the residuals although it was probable that acetonitrile solvent was present. The SQUEEZE[218] routine in the PLATON[218] program package was used to account for the electrons in the solvent accessible voids.

Synthesis of Metal Complexes

$K_2[Fe^{II}poat(OH)]$ A solution of H_3poat (0.200 g, 0.268 mmol) in 5 mL THF was treated with solid KH (0.033 g, 0.82 mmol) and stirred until all H_2 evolved (30 min). $Fe(OAc)_2$ (0.048 g, 0.28 mmol) was subsequently added to the yellow solution and stirred for 25 minutes to produce a bright yellow mixture. Water (5 μL, 0.3 mmol) was added via syringe that was stirred for 5 minutes and then filtered through a medium porous-glass frit. KH (0.011 g, 0.27 mmol) was added and allowed to stir until bubbling ceased giving an orange mixture. The mixture was filtered to give an orange filtrate. Et_2O was allowed to diffuse resulting in light orange crystals (86 %) suitable for XRD studies. FTIR (ATR, cm^{-1}) 3631, 3049, 2944, 2821, 1481, 1433, 1277, 1243, 1176, 1168, 1155, 1146, 1114, 1046, 1027, 961, 925, 746, 696, 620, 608, 583, 579, 575, 568, 561, 558, 554. EPR (X-band Parallel, DMF:THF, 10 K, silent) Mossbauer (DMF:THF, 4K, δ = 0.334 mm/s; ΔE_Q = 0.897 mm/s).

$K[Fe^{III}poat(OH)]$ A solution of H_3poat (0.200 g, 0.268 mmol) in 5 mL THF or DMA was treated with solid KH (0.033 g, 0.82 mmol) and stirred until all H_2 evolved (30 min). $Fe(OAc)_2$ (0.048 g, 0.28 mmol) was subsequently added to the yellow solution and stirred for 25 minutes to produce a bright yellow mixture and then filtered through a medium porous-glass frit to give a white precipitate (KOAc) and a yellow filtrate. Water (5 μL, 0.3 mmol) was added via syringe that was stirred for 5 minutes. KH (0.011 g, 0.27 mmol) was

added and allowed to stir until bubbling ceased giving an orange mixture. The mixture was filtered to give an orange filtrate. Half an equivalent of I_2 was added (0.034 g, 0.13 mmol) and the solution turned yellow brown and stirred for 30 minutes. (The reaction mixture is darker in DMA). The reaction mixture was then reduced to dryness and triturated with Et_2O until the residue was a free flowing powder. The powder was re-dissolved in MeCN (4 mL) and filtered to remove KI. Et_2O was allowed to diffuse into the MeCN solution resulting in yellow crystals (20 %) suitable for XRD studies. FTIR (ATR, cm^{-1}) 3561, 3050, 2929, 2890, 2848, 2312, 2270, 1677, 1481, 1434, 1381, 1347 1278, 1234, 1187, 1176, 1062, 1027, 957, 923, 851, 787, 750, 699, 695, 577. UV-vis (DMF:THF, λmax nm, (ε_{max}, M^{-1} cm^{-1}) 370 (3750) . EPR (X-band Parallel, DMF:THF, 10 K, g = 9.57, 5.30) Mossbauer (DMF:THF, 4K, δ = 0.334 mm/s; ΔE_Q = 0.897 mm/s).

[Fe^{III}POAT]•KBF_4 A suspension of K[Fe^{II}POAT] (115 mg, 0.137 mmol) in THF (3 mL) was treated with [$FeCp_2$][BF_4] (36 mg, 0.13 mmol) and stirred for two hours. The solution was filtered to remove orange solids. The orange solid was re-dissolved in MeCN and layered under Et_2O to yield orange crystals suitable for XRD studies (15%). UV-vis (MeCN, λmax nm, (ε_{max}, M^{-1} cm^{-1})) 385, 335. EPR (X-band Parallel, MeCN, 10 K, g = 7.01, 5.52, 3.27) Mossbauer (DMF:THF, 4K, δ = 0.339 mm/s; ΔE_Q = 1.098 mm/s)

Preparation of Low-Temperature EPR Samples. A solution of [Fe^{II}poat(OH)]$^{2-}$ (0.020 g, 0.022 mmol) in a DMF:THF mixture (22 mM, 150 μL) was transferred to an EPR tube and sealed with a rubber septum. The tube was brought out of the dry box and placed in a − 60 °C acetone/dry ice bath and allowed to equilibrate for fifteen minutes. A 100 mM stock solution of $FcBF_4$ was prepared in a DMF:THF mixture and kept at – 35 °C for the duration of the experiments. Two equiv of oxidant (65 μL) was added via a 12” needle syringe. After

mixing by careful pumping the syringe up and down, the EPR tube was quickly removed from the cold bath, wiped clean of acetone, and frozen in liquid nitrogen before analysis. *Preparation of solution NRVS Samples for **8** and **10**.* Samples were prepared as previously described in chapter 5. Solution NRVS sample holders were prepared from Mössbauer sample holders by cutting a 2 x 6 mm slot out of the bottom and covering the hole with kapton tape. A 33 mM solution of 96% ^{57}Fe-enriched **8** (0.026 mg, 0.030 mmol) was prepared in DMF:THF (750 μL) with 18c6 (0.007 mg, 0.027 mmol) added to increase solubility. A NRVS sample holder was cooled in the cold well of a drybox to -196 °C. To the pre-cooled NRVS sample holder, a sample of $[Fe^{II}pout(OH)]^-$ (500 μL of the XX mM solution) was added via syringe and allowed to freeze completely. The sample was then transferred from the dry box and quickly placed in a storage container pre-cooled to 77 K. Samples were analyzed for purity using Mössbauer spectroscopy prior to, and after NRVS data collection. In the case of **10**, analogous prep was followed in a DMF:THF mixture with the following modifications: A 33 mM solution of 96% ^{57}Fe-enriched $[Fe^{II}poat(OH)]^{2-}$ (0.015 mg, 0.017 mmol) was prepared in DMF:THF (500 μL) with 18c6 (0.020 mg, 0.076 mmol) added to increase solubility. A 240 M (0.033 g, 0.121 mmol) stock solution of $FcBF_4$ was prepared in a DMF:THF mixture (500 μL) and kept at – 35 °C for the duration of the experiments. Two equivs of oxidant (140 μL) was added. After mixing, an aliquot of the sample was transferred to the NRVS cup and allowed to completely freeze followed by transferred from the dry box and quickly placed in a storage container pre-cooled to 77 K.

Appendix A

Generation and Characterization of Fe and Mn Heterobimetallic Complexes

Introduction

As described throughout the literature and our group's previous work, $[MST]^{3-}$ strongly stabilizes structures with M^{II}–(μ–OH)–TM^{III} (M^{II} = Ca^{II}, Sr^{II}, or Ba^{II} and TM^{III} = Mn^{III} or Fe^{III}) cores;[68,69] however, studies have shown that the $[MST]^{3-}$ ligand is unable to form complexes with transition metal oxidation states above +3, which is postulated to be caused by the relatively weak electronic donating ability of the sulfonamides. To address these limitations, the following appendix describes the development and investigation of structurally characterized Mn and Fe systems within the symmetrical ligands (*N,N',N"*–(nitrilotris(ethane-2,1-diyl)tris(*P,P*-diphenylphosphonic amidate) $[poat]^{3-}$ (Figure A.1A) and (*N,N',N"*–(nitrilotris(ethane-2,1-diyl)tris(*P,P*-diphenylphosphoryl amidate) $[pop]^{3-}$ (Figure A.1B) and their interactions with Ca^{2+} ions. The ligand precursors possess an apical nitrogen and phosphinic or phosphonic amide moieties that when deprotonated coordinate to a transition metal ion. As previously described, the phosphinic/phosphonic amide moieties provide two advantages over the sulfonamide unit: (1) the nitrogen atoms are more electron–rich, allowing access to higher oxidation states of the corresponding metal

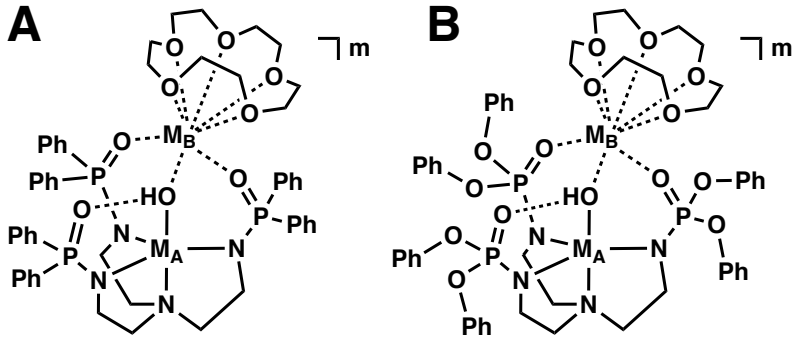

Figure A.1 Heterobimetallic structures of phosphorus containing tripodal ligands: $[poat]^{3-}$ (**A**) and $[pop]^{3-}$ (**B**).

complexes, and (2) the oxygen atoms are also more electron rich, which will make them both better H-bond acceptors as well as better ligands to support binding of an additional metal ion. Thus, the more electron-rich phosphorus–containing scaffold should support higher valent heterobimetallic complexes with oxido, hydroxido, and aqua ligands than those previously observed with $[MST]^{3-}$.

Results and Discussion

Preparation of Ligands. The preparation of the ligand precursor H_3poat was described in chapter 5. H_3pop was prepared from an analogous reaction between tren and diphenyl phosphoryl chloride in a comparable yield (80%).

Preparation of Mn Heterobimetallic Complexes: $N^nBu_4[Mn^{II}poat]$ and $N^nBu_4[Mn^{II}pop]$ were obtained via deprotonation of the respective ligand precursor with three equivalents of NaH in anhydrous tetrhydrofuran (THF) (8 mL) followed by metalation with $Mn^{II}(OAc)_2$ (Scheme 5.2). Treatment with an tetrabutyl-ammonium acetate gave the following metathesized products $N^nBu_4[Mn^{II}L]$ (L= poat or pop). The mixture was filtered to remove insoluble species, and then the solution was concentrated to dryness under vacuum to give $N^nBu_4[Mn^{II}L]$ as white powders. Treatment of a THF or dichloromethane (DCM) solution of $N^nBu_4[Mn^{II}L]$ and $[Ca^{II}\subset(15c5)]OTf_2$ with excess dioxygen afforded the heterobimetallic complexes of the form $[(15c5)\supset Ca^{II}–(\mu\text{-}OH)–Mn^{III}L]^+$. Oxidation yielded discrete heterobimetallic complexes in which a hydroxido ligand bridged between a Mn^{III} ion and a

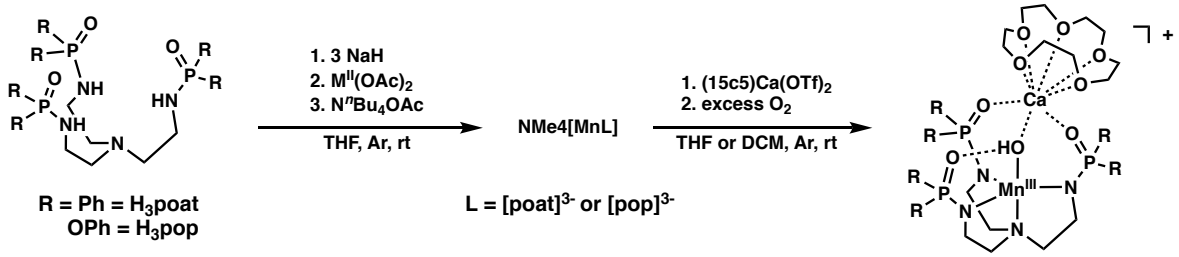

Scheme A.1 Preparation route of heterobimetallic complexes.

Ca^{II} ion (Scheme A.1).

The molecular structures of the heterobimetallic complexes were determined by X–ray diffraction (XRD) methods (Figure A.2 and Table A.1) and were found to be structurally similar to the previously characterized [(15c5)⊃Ca^{II}–(μ-OH)–Mn^{III}MST]$^+$ system (Table A.2).[69] The Mn^{III} centers in all three structures have an N_4O primary coordination sphere with trigonal bipyramidal geometry, and the S–O or P–O units produce a cavity that is capable of both forming an intramolecular H-bond between the Mn^{III}–OH unit and binding a second metal ion. The average Mn^{III}–N_{eq} distances in [(15c5)⊃Ca^{II}–(μ-OH)–Mn^{III}poat]$^+$ and [(15c5)⊃Ca^{II}–(μ-OH)–Mn^{III}MST]$^+$ are statistically the same at 2.058(3) and 2.052(2) Å, respectively, but this distance is slightly shorter in the $[pop]^{3-}$ complex with a value of 2.042(2) Å. The Ca1–O1 and Ca1–O2 distances of [(15c5)⊃Ca^{II}–(μ-OH)–Mn^{III}poat]$^+$ are significantly shorter than those of [(15c5)⊃Ca^{II}–(μ-OH)–Mn^{III}pop]$^+$ or [(15c5)⊃Ca^{II}–(μ-OH)–Mn^{III}MST]$^+$ (Table A.2), suggesting that the P–O bonds are better donors to the Ca^{II} ion in the [(15c5)⊃Ca^{II}–(μ-OH)–Mn^{III}poat]$^+$ complex.

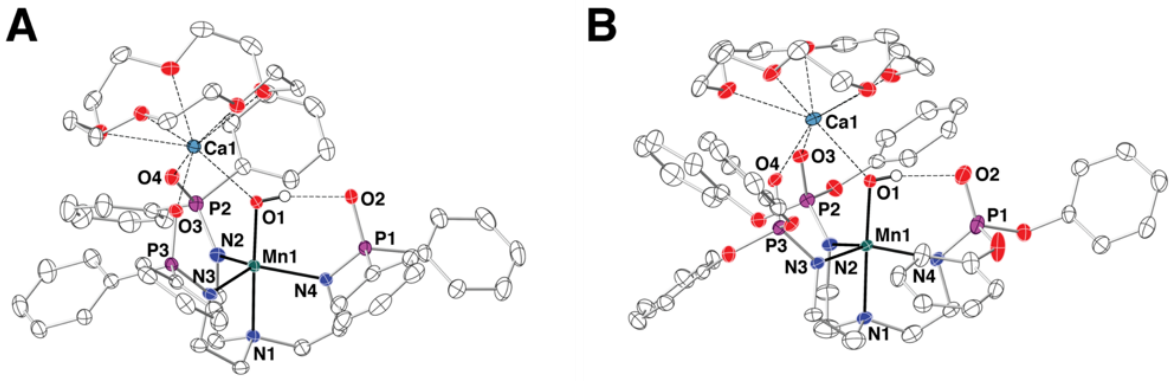

Figure A.2 The molecular structures of [15C5⊂Ca^{II}(μ–OH)Mn^{III}poat]$^+$ (A), [15C5⊂Ca^{II}(μ–OH)Mn^{III}pop] (B). The thermal ellipsoid plot is shown at the 50% probability level. Only hydroxido hydrogen atoms are shown and counter ions were removed for clarity.

Table A.1 Crystallographic Data and Structure Refinement Parameters for the $[(15c5)\supset Ca^{II}–(\mu\text{-}OH)–Mn^{III}L]^+$

Complex	$[(15c5)\supset Ca^{II}–(\mu\text{-}OH)–Mn^{III}poat]^+$	$[(15c5)\supset Ca^{II}–(\mu\text{-}OH)–Mn^{III}pop]^+$
Empirical Formula	$C_{56}H_{69}CaCl_6F_3MnN_4O_{12}P_3S$	$C_{53}H_{63}CaF_3MnN_4O_{18}P_3S$
Formula weight	1479.84	1321.06
Crystal system	triclinic	monoclinic
Space group	$P\bar{1}$	P 1 21/n 1
a (Å)	12.4948(15)	15.4435(9)
b (Å)	17.045(2)	17.0906(10)
c (Å)	19.008(2)	22.1845(13)
α (°)	115.6947(14)	90
β (°)	93.6464(15)	90.8545(8)
χ (°)	107.2098(14)	90
Volume (Å^3)	3396.8(7)	5854.7(6)
Z	2	4
δcalc (Mg/m3)	1.447	1.499
GOF	1.030	1.012
R1	0.0616	0.0530
wR2	0.1632	0.1175

Characterization of $[15C5\subset Ca^{II}–(\mu–OH)–Mn^{III}poat]^+$ by UV–vis spectroscopy gave two features in the visible region at λ_{max}/nm (ε_M) = 440 (sh) and 720 (207) (Figure A.3A) whose energies and relative intensities are similar to previously reported trigonal Mn^{III}–hydroxido complexes from our group.[68,183,219] The UV–vis spectrum of $[15C5\subset Ca^{II}(\mu–OH)Mn^{III}pop]^+$ displays three bands in the visible range at λ_{max}/nm (ε_M) = 440 (125), 620 (225), and 800 (sh) (Figure A.3B). The spectrum of $[15C5\subset Ca^{II}(\mu–OH)Mn^{III}pop]^+$ more closely resembles the $[15C5\subset Ca^{II}(\mu–OH)Mn^{III}MST]^+$ complex, which has also has broad absorbances at λ_{max} = 450 (340), 640 (600), and 800 (sh) nm.[68]

Table A.2 Selected Bond Distances and Angles for $[(15c5)\supset Ca^{II}–(\mu\text{-}OH)–Mn^{III}L]^{+}$

Bond Distances (Å) or Angles (°)	$[poat]^{3-}$	$[pop]^{3-}$	$[MST]^{3-}$
Mn1–O1	1.848(3)	1.835(2)	1.829(2)
Mn1–N1	2.073(3)	2.051(2)	2.075(2)
Mn1–N2	2.051(3)	2.053(2)	2.019(18)
Mn1–N3	2.083(3)	2.053(2)	2.107(2)
Mn1–N4	2.040(3)	2.019(2)	2.029(2)
$Mn1–N_{avg}$	2.058(3)	2.042(2)	2.052(2)
Mn1–Ca1	3.855(3)	3.845(2)	3.748(2)
O1…O2	2.717(*)	2.689(*)	2.693(2)
Ca1…O4	2.387(3)	2.349(2)	2.342(2)
Ca1…O1	2.285(3)	2.307(2)	2.333(2)
Ca1…O3	2.270(3)	2.332(2)	2.370(2)
$Ca1…O_{Pavg}$	2.314	2.329	2.347
$Ca1…O_{15c5avg}$	2.596	2.569	2.480
O1–Mn1–N2	97.08(12)	98.16(9)	96.95(8)
O1–Mn1–N4	96.32(12)	96.64(10)	96.58(8)
O1–Mn1–N1	176.68(12)	177.46(10)	176.94(9)
O1–Mn1–N3	101.36(12)	99.78(9)	101.09(8)
N2–Mn1–N4	124.77(13)	122.99(10)	131.81(10)
N2–Mn1–N1	81.80(12)	81.24(9)	81.83(9)
N4–Mn1–N1	81.84(12)	81.68(10)	82.25(9)
N2–Mn1–N3	117.74(13)	106.30(9)	109.38(9)
N4–Mn1–N3	111.51(13)	122.99(10)	112.93(9)
N1–Mn1–N3	81.92(12)	82.75(9)	81.97(9)
Mn1–O1–Ca1	130.64(13)	133.21(11)	127.49(9)

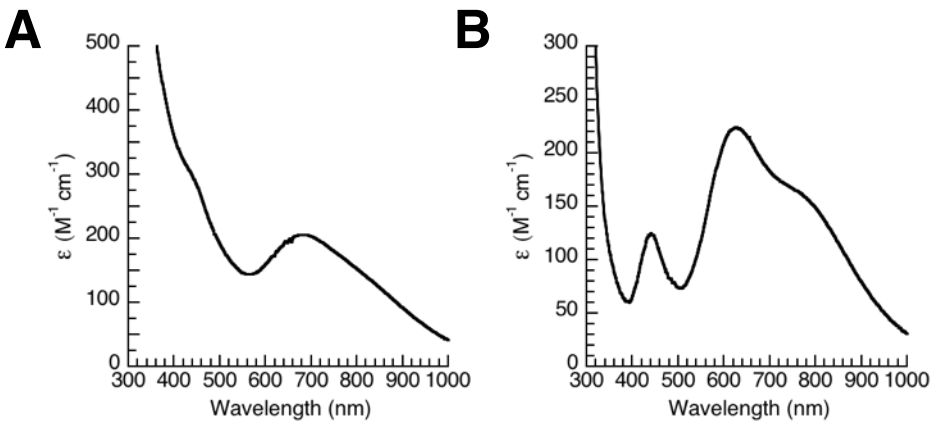

Figure A.3 UV-vis spectra of: [15C5⊂Ca^{II}–(μ–OH)–Mn^{III}poat]$^+$ (A) and [15C5⊂Ca^{II}–(μ–OH)–Mn^{III}pop]$^+$ (B). Spectra were collected in DCM at 25 °C.

Oxidation Experiments. Electrochemical analysis of the [15C5⊂Ca^{II}–(μ–OH)–Mn^{III}poat]$^+$ complex exhibited a quasi-reversible one-electron redox process at 360 mV vs $FeCp_2^{+/0}$ that is assigned to the Mn^{III}/Mn^{IV} couple (Figure A.4A). In the case of [15C5⊂Ca^{II}–(μ–OH)–Mn^{III}pop]$^+$, an initial irreversible redox event occurred at a more positive potential of approximately 660 mV vs $FeCp_2^{+/0}$. There is an additional irreversible event beyond 660 mV at approximately 980 mV vs $FeCp_2^{+/0}$. It is possible the event is due to ligand oxidation by cleavage of the P–N bond.[220] Further experiments are necessary to confirm this

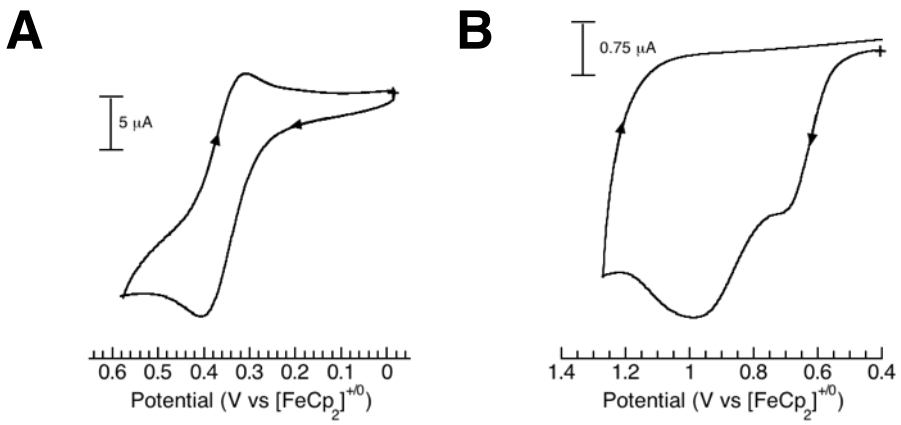

Figure A.4 Cyclic voltammogram of [(15c5)⊃Ca^{II}–(μ-OH)–Mn^{III}poat]$^+$ (A) and [(15c5)⊃Ca^{II}–(μ-OH)–Mn^{III}pop]$^+$. Data was collected in DCM with 0.1 M TBAP, 10 mV/s, and ferrocene as an internal standard.

hypothesis. The electrochemical data suggests that the phosphine oxide containing ligand scaffold ([poat]$^{3-}$, Figure A.1A) is more electron donating than the analogous phosphonate containing ligand ([pop]$^{3-}$, Figure A.1B). Comparison to work done by Tolman determining the electron donating nature of various phosphine ligands, the trend seen between [poat]$^{3-}$ and [pop]$^{3-}$ is reasonable. Tolman analyzed $Ni(CO)_3L$ complexes, where L is the phosphorus-containing ligand, and was able to determine the electron donor-acceptor properties of over 70 phosphorus ligands by monitoring how each affected the CO stretching frequency (ν_{CO}). The most appropriate comparisons to [poat]$^{3-}$ and [pop]$^{3-}$ are the ligands PPh_3 and $P(OPh)_3$, respectively. It was observed that the Ni complex containing a PPh_3 ligand had a ν_{CO} = 2068.9 cm^{-1}, while the analogous complex with $P(OPh)_3$ gave a ν_{CO} = 2085.3 cm^{-1}.[221] This data suggests that the PPh_3 group donates more electron density to the metal center, allowing it to participate in more π-back bonding with the carbonyl ligands. More π-back bonding results in a weakened CO bond, which is reflected in a lower stretching frequency. It is reasonable that the same electronic trend would be seen between phosphinic ($P(O)R_2$) and phosphonic ($P(O)(OR)_2$) moieties, which is supported by the electrochemical data collected for [15C5⊂Ca^{II}–(μ–OH)–Mn^{III}poat]$^+$ and [15C5⊂Ca^{II}–(μ–OH)–Mn^{III}pop]$^+$. These potentials support the hypothesis that the phosphorus ligand scaffold could afford access to higher valent Mn compounds than seen with the sulfonamides. There is no reported Mn^{III}/Mn^{IV} couple reported for [15C5⊂Ca^{II}–(μ–OH)–Mn^{III}MST]$^+$.

Studies were conducted to determine the feasibility of oxidizing the [15C5⊂Ca^{II}–(μ–OH)–Mn^{III}poat]$^+$ complex to give Ca^{II}–(μ–OH)–Mn^{IV} or Ca^{II}–(μ–OH)–Mn^{V} cores. Oxidation reactions of [15C5⊂Ca^{II}–(μ–OH)–Mn^{III}poat]$^+$ were monitored optically at multiple

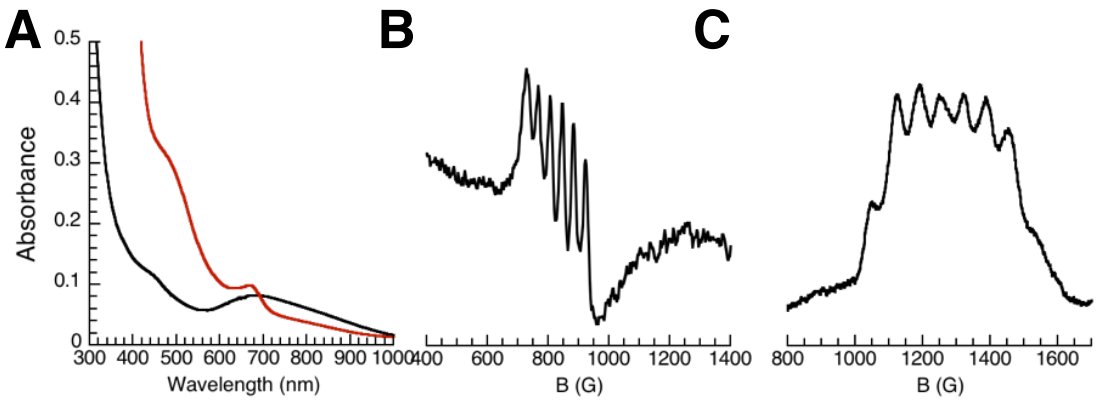

Figure A.5 UV–vis spectra monitoring the conversation (initial black; final red) (A). ||–EPR spectrum of the starting synthon [15C5⊂Ca^{II}(μ–OH)Mn^{III}poat]$^{+}$ (B). and ⊥–mode EPR spectrum after addition of 1 equiv [N(*p*-tol)$_3$]$^{+\bullet}$ (C). UV-vis and EPR spectra were collected at – 30 °C and 10 K, respectively, asterisk indicates excess [N(*p*-tol)$_3$]$^{+\bullet}$.

temperatures below 0 °C. Addition of one equivalent of the oxidant tris-*para*-tolylamminium radical ([N(*p*–tol)$_3$]$^{+\bullet}$, 0.4 V vs $FeCp_2^{+/0}$) resulted in the loss of the two bands attributed to the Mn^{III}–hydoxido species and subsequent growth of a shoulder at λ_{max} = 460 nm (Figure A.5C). The feature at 460 nm is at a similar energy as the band observed for the previously reported [$Mn^{IV}H_3$buea(OH)] complex,[80] while the 670 nm band is likely due to excess oxidant. EPR experiments corroborate the one–electron oxidation of [15C5⊂Ca^{II}–(μ–OH)–Mn^{III}poat]$^{+}$ to the proposed [15C5⊂Ca^{II}–(μ–OH)–Mn^{IV}poat]$^{2+}$ complex upon addition of one equivalent of [N(*p*–tol)$_3$]$^{+\bullet}$ (Figure A.5C). [15C5⊂Ca^{II}–(μ–OH)–Mn^{III}poat]$^{+}$ was first analyzed by parallel–mode EPR spectroscopy (||–mode EPR), giving a signal with six–line hyperfine (A= 97.6 G) centered at g = 8 that is consistent with a Mn^{III} ion in trigonal symmetry with an S = 2 spin ground state (Figure A.5B). Upon addition of oxidant, there is growth of a new signal in the ⊥–mode spectrum centered at g = 5 as well as several features at higher field, which are not shown due to an intense S = ½ signal that is attributed to unreacted oxidant. The low field values are consistent with the expected S = 3/2 spin-state for a high spin Mn^{IV} ion. The signal at g = 5 contains a hyperfine splitting

pattern composed of two sets of six lines. The overlapping six line features (Figure A.5C) are likely caused by contributions from both the ground m_S = ½ and excited m_S = 3/2 doublets of a single Mn^{IV} center, as has been previously found for the $[Mn^{IV}H_3buea(O/OH)]^{-/0}$ complexes.[80,222]

Iron Heterobimetallic Systems. As referenced in chapter 5, the development of high valent iron compounds containing a redox inactive metal ion is of particular interest due to recent conflicting reports by Nam and Que.[174,223] To date the work done with $[poat]^{3-}$ has not yielded any structural confirmation of how the Ca ion interacts with the Fe complexes. Preliminary work with $[pop]^{3-}$ has allowed for the isolation of the analogous Fe^{III} heterobimetallic system to the Mn^{III} complex discussed above. $[15C5{\subset}Ca^{II}{-}(\mu{-}OH){-}Fe^{III}pop]^{+}$ was prepared in a similar fashion as the previously discussed for the manganese heterobimetallic complex, $[15C5{\subset}Ca^{II}{-}(\mu{-}OH){-}Mn^{III}pop]^{+}$, with a minor modification to the employed metathesis salt (NMe_4OAc). The molecular structure determined by XRD methods confirmed the predicted $Ca^{II}{-}(\mu{-}OH){-}Fe^{III}$ core structure (Figure A.5 and Table A.3). The Fe^{III} center has an N_4O primary coordination sphere that adopts a trigonal bipyramidal geometry. The Fe1–N1 bond length of 2.216(2) Å and an average $Fe1{-}N_{eq}$

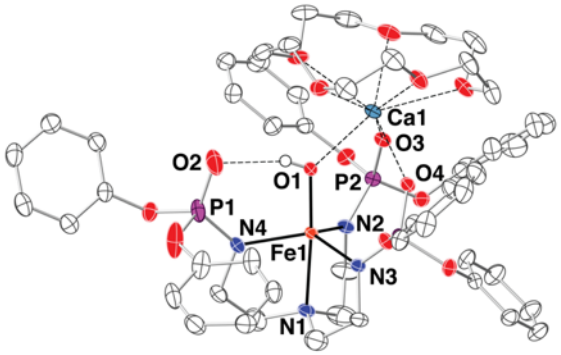

Figure A.6 Thermal ellipsoid diagram depicting the molecular structure $[15C5{\subset}Ca^{II}{-}(\mu{-}OH){-}Fe^{III}pop]^{+}$. Only hydroxido hydrogen atoms are shown and counter ions were removed for clarity. The thermal ellipsoid plot is shown at the 50% probability level.

bond distance of 2.018(2) Å (Table A.4). The primary coordination sphere of the iron center is completed by a hydroxido ligand having an Fe1–O4 bond distance of 1.872(2) Å and an N1–Fe1–O4 bond angle of 174.53(8)°. The distance between the Fe^{III}–OH unit and O3 of the $[15C5{\subset}Ca^{II}–(\mu–OH)–Fe^{III}pop]^+$ is 2.652(6) Å, well within the range of an H-bond interaction. The Ca^{II} ion is coordinated to O1 and O2 of $[15C5{\subset}Ca^{II}–(\mu–OH)–Fe^{III}pop]^+$ with

Table A.3 Crystallographic Data and Structure Refinement Parameters for the $[(15c5){\supset}Ca^{II}–(\mu\text{-}OH)–Fe^{III}pop]^+$

Empirical Formula	$C_{53}H_{63}CaF_3FeN_4O_{18}P_3S$
Formula weight	1321.97
Crystal system	monoclinic
Space group	$P2_1/n$
a (Å)	15.5704(17)
b (Å)	17.0485(18)
c (Å)	22.134(2)
α (°)	90
β (°)	91.2601(14)
χ (°)	90
Volume (Å^3)	5874.1(11)
Z	4
δcalc (Mg/m3)	1.495
GOF	1.033
R1	0.0583
wR2	0.1364

bond distances of 2.321(2) and 2.356(2) Å, and to the hydroxido oxygen atom with a Ca1–O4 bond length of 2.314(2) Å. Compared to the analogous $[15C5{\subset}Ca^{II}–(\mu–OH)–Fe^{III}MST]^+$ complex, there is a similar trend that was seen with the manganese complexes. For $[15C5{\subset}Ca^{II}–(\mu–OH)–Fe^{III}pop]^+$, the Fe1–$N_{eq}$ bond distance is shorter than what is found for $[15C5{\subset}Ca^{II}–(\mu–OH)–Fe^{III}MST]^+$.[69] Also there appears to be a stronger H-bonding interaction in $[15C5{\subset}Ca^{II}–(\mu–OH)\ Fe^{III}pop]^+$ than $[15C5{\subset}Ca^{II}–(\mu–OH)–Fe^{III}MST]^+$ based on

the shortened O3···O4 distance of 2.652(6) Å from 2.700(6) Å. The Fe^{III}–hydroxido species has a single broad absorbance band at λ_{max}/nm ($\varepsilon_M/M^{-1}\ cm^{-1}$) = 340 (2480), which is similar to the band observed for the HS $[Fe^{III}H_3buea(OH)]^-$.[36] The perpendicular mode (⊥–)EPR spectrum of $[15C5{\subset}Ca^{II}–(\mu–OH)–Fe^{III}pop]^+$ displayed a rhombic signal with g = 8.9, 4.8, 3.9, and 2.0 (Figure A.6A). The anisotropy of the spectrum can be attributed to the distortions of the ligand field about the Fe center.

Table A.4 Selected Bond Distances and Angles for $[(15c5){\supset}Ca^{II}–(\mu\text{-}OH)–Mn^{III}L]^+$

Bond Distances (Å) or Angles (°)	$[pop]^{3-}$	$[MST]^{3-}$
Fe1–N1	2.216(2)	2.230(2)
Fe1–N2	2.034(2)	2.0236(2)
Fe1–N3	2.016(2)	2.0163(2)
Fe1–N4	2.004(2)	2.0464(2)
Fe1–O4	1.872(2)	1.865(2)
O3···O4	2.652(6)	2.700(6)
Fe1···Ca1	3.802(3)	3.709(2)
Ca1···O4	2.314(2)	2.316(2)
Ca1···O1	2.321(2)	2.344(2)
Ca1···O2	2.356(2)	2.370(2)
$Ca1\cdots O_{15c5avg}$	2.567(2)	2.508(2)
O4–Fe1–N1	174.53(8)	173.57(7)
Fe1–O4–Ca1	130.02(6)	125.27(7)

To investigate the possibility of accessing an Fe^{IV} species, the yellow solution of $[15C5{\subset}Ca^{II}–(\mu–OH)–Fe^{III}pop]^+$ was treated with one equivalent of thianthrene radical ($Th^{+\bullet}$) (0.8 V vs $FeCp_2^{+/0}$) at – 80 °C, which produced an unstable species corresponding to an absorbance spectrum with bands at λ_{max}/nm = 450, 605 and a broad absorbance at 975 (Figure A.6B). The new spectrum does not resemble that of our published high spin $[Fe^{IV}H_3buea(O)]^-$ or $[Fe^{IV}TST(O)]^-$ complexes previously prepared in our group, which have,

although weak, a distinct transition around 800 nm.[39] ([TST]$^{3-}$ is the analogous ligand scaffold to [MST]$^{3-}$ with tolyl groups in place of the mesityl substituents.) A similar low energy band would be expected for the oxidized heterobimetallic complex because all reported synthetic, non-heme Fe^{IV}–(O) systems display this optical feature regardless of the local geometry about the iron center.[40-42] The oxidation of [15C5⊂Ca^{II}(μ–OH)Fe^{III}pop]$^{+}$ was monitored by EPR spectroscopy and showed a loss of the Fe^{III} signal to a silent spectrum in ⊥–mode. The loss of the ⊥–mode EPR signal supports the production of Fe^{IV} by the one electron oxidation of the Fe^{III} complex. Generation of an Fe^{IV} species needs to be corroborated by Mössbauer and ||-mode EPR spectroscopies.

Experimental.

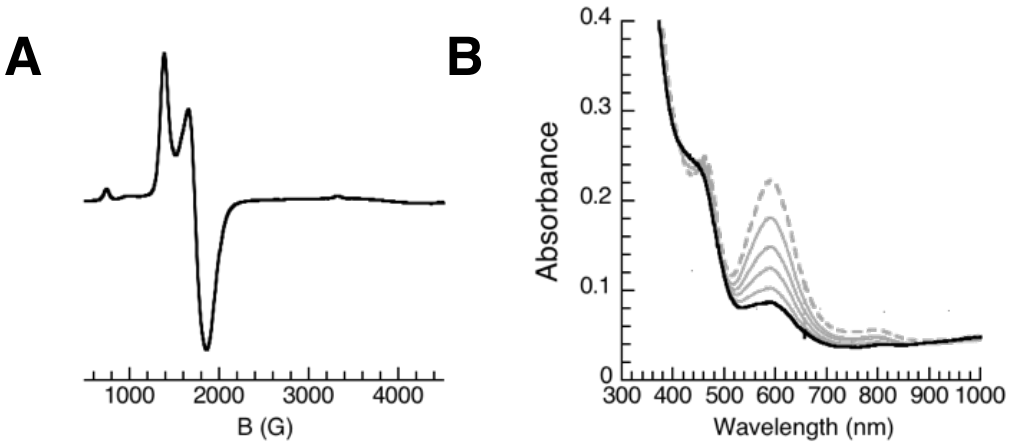

Figure A.6 ⊥–EPR spectrum of [15C5⊂Ca^{II}–(μ–OH)–Fe^{III}pop]$^{+}$ (A). UV-vis spectrum after addition of 1 equiv $Th^{+\bullet}$ (Initial spectrum in gray dash of thianthrene radical; final (black solid).UV–vis and EPR spectra collected in EtCN at –80 °C and 77 K, respectively.

General Procedures. All reactions, unless otherwise noted, were performed under a nitrogen atmosphere in a dry box. All chemicals were purchased from commercial sources and used as received unless otherwise stated. Solvents were sparged with argon and dried over columns containing Q-5 and molecular sieves. Sodium hydride as a 30% suspension in

mineral oil was filtered and washed with 10 mL diethyl ether and 10 mL pentane five times each. $Ca(OTf)_2$/15-crown-5, tris-*para*-tolylamminium radical, and thianthrene radical were prepared according to literature protocol.[68,145,224]

Preparation of Ligands.

H_3poat and H_3pop. Prepared as described in Chapter 2.

Complex Syntheses

[15-crown-5⊃Ca^{II}–(μ–OH)–Mn^{III}poat]OTf. A solution of H_3poat (0.20 g, 0.27 mmol) dissolved in 8 mL of anhydrous THF was treated with solid NaH (21 mg, 0.88 mmol). The mixture was stirred until gas evolution ceased. $Mn(OAc)_2$ (45 mg, 0.26 mmol) and NBu_4OAc (84 mg, 0.28 mmol) were added to the colorless solution after which the mixture was stirred for 2 h. The cloudy, pale yellow solution was filtered into a schlenk flask to remove insoluble NaOAc. Ca(OTf2)(15-crown-5)ether (0.15 g, 0.27 mmol) was added to the flask, which was then sealed with a rubber septum and brought out from the dry box. An equivalent of O_2 (6 mL, T = 298 K, P = 1 atm, 0.12 mmol) was injected to the headspace via syringe and the mixture was stirred for 1 h at room temperature. After one hour, all volatiles were removed under vacuum and the reaction flask was brought into the box. The dark green residue was redissolved in DCM (5 mL) and filtered to remove any insoluble materials. The filtrate was layered under pentane and stored at -35 °C. After 48 hours long fluffy colorless needle-like crystals grew. The dark green filtrate was decanted and concentrated to a green solid. The solid was dissolved in DCM, layered under pentane and stored at -35 °C. After a week, dichroic dark green/brown-yellow crystals formed. The resulting crystals were collected on a glass frit and dried under vacuum, affording the product in yields that ranged between 75 - 80%. FTIR (KBr disc, cm-1, selected bands): 3270, 3160, 1590, 1377, 1223, 804, 722,

637.

[15-crown-5Ca^{II}–(μ–OH)–Mn^{III}pop]OTf. Preparation of the phosphononic amide Mn/Ca system followed the above procedure with H_3pop (0.20 g, 0.20 mmol). After 4 days dark blue/green crystals formed. The resulting crystals were collected on a glass frit and dried under vacuum, affording the desired salt in yields that ranged from 75 - 80%. FTIR (KBr disc, cm-1, selected bands): 3319, 3180, 1591, 1461, 1377, 1271, 1136, 1093, 1029, 951, 668, 639.

[15-crown-5Ca^{II}–(μ–OH)–Fe^{III}pop]OTf. A solution of H_3pop (0.20 g, 0.24 mmol) dissolved in 5 mL of anhydrous THF was treated with solid NaH (18 mg, 0.75 mmol). The mixture was stirred until gas evolution ceased. $Fe(OAc)_2$ (43 mg, 0.25 mmol) and NMe_4OAc (34 mg, 0.18 mmol) were added to the colorless solution after which the mixture was stirred for 1 h. The cloudy, pale yellow solution was filtered into a schlenk flask to remove insoluble NaOAc. Ca(OTf2)(15-crown-five)ether (0.13 g, 0.24 mmol) was added to the flask. The flask was sealed with a rubber septum and brought out from the dry box after which an equivalent of O_2 (6 mL, T = 298 K, P = 1 atm, 0.12 mmol) was injected to the headspace via syringe and the mixture was stirred for 1 h at room temperature. After one hour, all volatiles were removed under vacuum and the reaction flask was brought into the box. The dark orange residue was redissolved in DCM (5 mL) and filtered to remove any insoluble materials. The filtrate was layered with pentane and stored at -35 °C. After 4 days, dark yellow crystals formed. The resulting dark yellow crystals were collected on a glass frit and dried under vacuum, affording the product in yields that ranged between 80 - 85%. FTIR (KBr disc, cm-1, selected bands): 3325, 2727, 26704, 1590, 1462, 1377, 1290, 1029, 818, 638.

Physical Methods.

Electronic absorption spectra were collected on a Cary 50 spectrometer or an Agilent UV-vis spectrophotometer equipped with a Unisoku Unispeks cryostat in either a 1 cm cuvette or a 1 mm thin cell cuvette. X-band EPR spectra were collected as frozen solutions using a Bruker EMX spectrometer equipped with an ER041XG microwave bridge and the data analyzed using SpinCount.[146] IR spectra were recorded on a Varian 800 Scimitar Series FTIR spectrometer in a nujol mull on KBr salt plates.

Cyclic Voltammetry

Experiments were conducted using a CHI600C electrochemical analyzer under an N_2 atmosphere with 0.1 M tetrabutylammonium hexafluorophosphate as the supporting electrolyte. A glassy carbon electrode was used for the working electrode with a silver wire reference electrode and a platinum wire counter electrode. A ferrocenium/ferrocene couple ($[FeCp_2]^{+/0}$) was used as an internal standard.

X-Ray Crystallographic Methods.

A Bruker SMART APEX II diffractometer was used to collect all data. The APEX2[148] program package was used to determine the unit-cell parameters and for data collection (60 sec/frame scan time for a sphere of diffraction data). The raw frame data was processed using SAINT[149] and SADABS[150] to yield the reflection data file. Subsequent calculations were carried out using the SHELXTL[217] program. The structures were solved by direct methods and refined on F^2 by full-matrix least-squares techniques. The analytical scattering factors for neutral atoms were used throughout the analysis. Hydrogen atoms were included using a riding model. A triflate was disordered about an inversion center and was modeled to account for the amount of electrons in a $(CF_3SO_3)^-$ fragment.

References

(1) Dawson, J. H. Probing Structure-Function Relations in Heme-Containing Oxygenases and Peroxidases. *Science.* **1988**, *240* (4851), 433–439.

(2) Holm, R. H.; Kennepohl, P.; Solomon, E. I. Structural and Functional Aspects of Metal Sites in Biology. *Chem. Rev.* **1996**, *96* (7), 2239–2314.

(3) Liu, J.; Chakraborty, S.; Hosseinzadeh, P.; Yu, Y.; Tian, S.; Petrik, I.; Bhagi, A.; Lu, Y. Metalloproteins Containing Cytochrome, Iron–Sulfur, or Copper Redox Centers. *Chem. Rev.* **2014**, *114* (8), 4366–4469.

(4) Borovik, A. S. Bioinspired Hydrogen Bond Motifs in Ligand Design: The Role of Noncovalent Interactions in Metal Ion Mediated Activation of Dioxygen. *Acc. Chem. Res.* **2005**, *38* (1), 54–61.

(5) Werner, A. Über Die Raumisomeren Kobaltverbindunge. *Ann. Chem.* **1912**, *386*, 1–272.

(6) Shook, R. L.; Borovik, A. S. The Effects of Hydrogen Bonds on Metal-Mediated O2 activation and Related Processes. *Chem. Commun.* **2008**, 46, 6095–6107.

(7) Shook, R. L.; Borovik, A. S. Role of the Secondary Coordination Sphere in Metal-Mediated Dioxygen Activation. *Inorg. Chem.* **2010**, *49* (8), 3646–3660.

(8) Solomon, E. I.; Brunold, T. C.; Davis, M. I.; Kemsley, J. N.; Lee, S.-K.; Lehnert, N.; Neese, F.; Skulan, A. J.; Yang, Y.-S.; Zhou, J. Geometric and Electronic Structure/Function Correlations in Non-Heme Iron Enzymes. *Chem. Rev.* **2000**, *100* (1), 235–350.

(9) Que, L.; Ho, R. Y. N. Dioxygen Activation by Enzymes with Mononuclear Non-Heme Iron Active Sites. *Chem. Rev.* **1996**, *96* (7), 2607–2624.

(10) Meunier, B.; De Visser, S. P. S. P.; Shaik, S. Mechanism of Oxidation Reactions Catalyzed by Cytochrome P450 Enzymes. *Chem. Rev.* **2004**, *104* (9), 3947–3980.

(11) Costas, M.; Mehn, M. P.; Jensen, M. P.; Que, L. J. Dioxygen Activation at Mononuclear Nonheme Iron Active Sites: Enzymes, Models, and Intermediates. *Chem. Rev.* **2004**, *104* (2), 939–986.

(12) Decker, A.; Solomon, E. I. Dioxygen Activation by Copper, Heme and Non-Heme Iron Enzymes: Comparison of Electronic Structures and Reactivities. *Curr. Opin. Chem. Biol.* **2005**, *9* (2), 152–163.

(13) Cady, C. W.; Crabtree, R. H.; Brudvig, G. W. Functional Models for the Oxygen-Evolving Complex of Photosystem II. *Coord. Chem. Rev.* **2008**, *252* (3–4), 444–455.

(14) Poulos, T. L. Heme Enzyme Structure and Function. *Chem. Rev.* **2014**, *114* (7), 3919–3962.

(15) Krest, C. M.; Onderko, E. L.; Yosca, T. H.; Calixto, J. C.; Karp, R. F.; Livada, J.; Rittle, J.; Green, M. T. Reactive Intermediates in Cytochrome P450 Catalysis. *J. Biol. Chem.* **2013**, *288* (24), 17074–17081.

(16) Denisov, I. G.; Makris, T. M.; Sligar, S. G.; Schlichting, I. Structure and Chemistry of Cytochrome P450. *Chem. Rev.* **2005**, *105* (6), 2253–2278.

(17) Rittle, J.; Green, M. T. Cytochrome P450 Compound I: Capture, Characterization, and C-H Bond Activation Kinetics. *Science.* **2010**, *330* (6006), 933–937.

(18) Mas-Balleste, R.; Que, L. J. Chemistry: Targeting Specific C-H Bonds for Oxidation. *Science.* **2006**, *312* (5782), 1885–1886.

(19) Price, J. C.; Barr, E. W.; Tirupati, B.; Bollinger, J. M.; Krebs, C. The First Direct

Characterization of a High-Valent Iron Intermediate in the Reaction of an Alpha-Ketoglutarate-Dependent Dioxygenase: A High-Spin FeIV Complex in Taurine/Alpha-Ketoglutarate Dioxygenase (TauD) from Escherichia Coli. *Biochemistry* **2003**, *42* (24), 7497–7508.

(20) Umena, Y.; Kawakami, K.; Shen, J.-R.; Kamiya, N. Crystal Structure of Oxygen-Evolving Photosystem II at a Resolution of 1.9 Å. *Nature* **2011**, *473* (7345), 55–60.

(21) Ono, T.; Inoue, Y. Discrete Extraction of the Ca Atom Functional for O2 Evolution in Higher Plant Photosystem II by a Simple Low PH Treatment. *FEBS Lett.* **1988**, *227* (2), 147–152.

(22) Yocum, C. The Calcium and Chloride Requirements of the O2 Evolving Complex. *Coord. Chem. Rev.* **2008**, *252* (3–4), 296–305.

(23) Boussac, A.; Zimmermann, J.-L.; Rutherford, A. W. EPR Signals from Modified Charge Accumulation States of the Oxygen-Evolving Enzyme in Calcium-Deficient Photosystem II. *Biochemistry* **1989**, *28* (23), 8984–8989.

(24) Boussac, A.; Zimmermann, J.-L.; Rutherford, A. W. Factors Influencing the Formation of Modified S2 EPR Signal and the S3 EPR Signal in Ca2+-Depleted Photosystem II. *FEBS Lett.* **1990**, *277* (1–2), 69–74.

(25) Ghanotakis, D. F.; Babcock, G. T.; Yocum, C. F. Calcium Reconstitutes High Rates of Oxygen Evolution in Polypeptide Depleted Photosystem II Preparations. *FEBS Lett.* **1984**, *167* (1), 127–130.

(26) McEvoy, J. P.; Brudvig, G. W. Water-Splitting Chemistry of Photosystem II. *Chem. Rev.* **2006**, *106* (11), 4455–4483.

(27) Mullins, C.; Pecoraro, V. Reflections on Small Molecule Manganese Models That Seek to Mimic Photosynthetic Water Oxidation Chemistry. *Coord. Chem. Rev.* **2008**, *252* (3–4), 416–443.

(28) Pecoraro, V. L.; Baldwin, M. J.; Caudle, M. T.; Hsieh, W.-Y.; Law, N. A. A Proposal for Water Oxidation in Photosystem II. *Pure Appl. Chem.* **1998**, *70* (4), 925–929.

(29) Sproviero, E. M.; Shinopoulos, K.; Gascon, J. A.; McEvoy, J. P.; Brudvig, G. W.; Batista, V. S. QM/MM Computational Studies of Substrate Water Binding to the Oxygen-Evolving Center of Photosystem II. *Philos. Trans. R. Soc. B Biol. Science.* **2008**, *363* (1494), 1149–1156.

(30) Kern, J.; Chatterjee, R.; Young, I. D.; Fuller, F. D.; Lassalle, L.; Ibrahim, M.; Gul, S.; Fransson, T.; Brewster, A. S.; Alonso-Mori, R.; et al. Structures of the Intermediates of Kok's Photosynthetic Water Oxidation Clock. *Nature* **2018**, 1.

(31) Cox, N.; Retegan, M.; Neese, F.; Pantazis, D. A.; Boussac, A.; Lubitz, W. Electronic Structure of the Oxygen-Evolving Complex in Photosystem II Prior to O-O Bond Formation. *Science.* **2014**, *345* (6198), 804–808.

(32) Cox, N.; Pantazis, D. A.; Neese, F.; Lubitz, W. Biological Water Oxidation. *Acc. Chem. Res.* **2013**, *46* (7), 1588–1596.

(33) Siegbahn, P. E. M. Structures and Energetics for O_2 Formation in Photosystem II. *Acc. Chem. Res.* **2009**, *42* (12), 1871–1880.

(34) Siegbahn, P. E. M.; Blomberg, M. R. A. A Combined Picture from Theory and Experiments on Water Oxidation, Oxygen Reduction and Proton Pumping. *Dalt. Trans.* **2009**, 30, 5832–5840.

(35) Bell, S. R.; Groves, J. T. A Highly Reactive P450 Model Compound I. *J. Am. Chem. Soc.* **2009**, *131* (28), 9640–9641.

(36) Groves, J. T.; Haushalter, R. C.; Nakamura, M.; Nemo, T. E.; Evans, B. J. High-Valent Iron-Porphyrin Complexes Related to Peroxidase and Cytochrome P-450. *J. Am. Chem. Soc.* **1981**, *103* (10), 2884–2886.
(37) Seo, M. S.; Kim, N. H.; Cho, K.-B.; So, J. E.; Park, S. K.; Clémancey, M.; Garcia-Serres, R.; Latour, J.-M.; Shaik, S.; Nam, W. A Mononuclear Nonheme Iron(Iv)-Oxo Complex Which Is More Reactive than Cytochrome P450 Model Compound I. *Chem. Science.* **2011**, *2* (6), 1039.
(38) Rohde, J.-U.; In, J.-H.; Lim, M. H.; Brennessel, W. W.; Bukowski, M. R.; Stubna, A.; Muenck, E.; Nam, W.; Que, L. J. Crystallographic and Spectroscopic Characterization of a Nonheme Fe(IV)=O Complex. *Science.* **2003**, *299* (5609), 1037–1039.
(39) Klinker, E. J.; Kaizer, J.; Brennessel, W. W.; Woodrum, N. L.; Cramer, C. J.; Que, L. J. Structures of Nonheme Oxoiron(IV) Complexes from X-Ray Crystallography, NMR Spectroscopy, and DFT Calculations. **2005**, *44* (24), 3690–3694.
(40) England, J.; Martinho, M.; Farquhar, E. R.; Frisch Jonathan, R.; Bominaar, E. L.; Munck, E.; Que, L. J. A Synthetic High-Spin Oxoiron(IV) Complex: Generation, Spectroscopic Characterization, and Reactivity. *Angew. Chem., Int. Ed. Engl.* **2009**, *48* (20), 3622–3626.
(41) England, J.; Guo, Y.; Farquhar, E. R.; Young, V. G. J.; Munck, E.; Que, L. J. The Crystal Structure of a High-Spin Oxoiron(IV) Complex and Characterization of Its Self-Decay Pathway. *J. Am. Chem. Soc.* **2010**, *132* (25), 8635–8644.
(42) Lacy, D. C.; Gupta, R.; Stone, K. L.; Greaves, J.; Ziller, J. W.; Hendrich, M. P.; Borovik, A. S. Formation, Structure, and EPR Detection of a High Spin FeIV—Oxo Species Derived from Either an FeIII—Oxo or FeIII—OH Complex. *J. Am. Chem. Soc.* **2010**, *132* (35), 12188–12190.
(43) Costas, M.; Mehn, M. P.; Jensen, M. P.; Que, L. Dioxygen Activation at Mononuclear Nonheme Iron Active Sites: Enzymes, Models, and Intermediates. *Chem. Rev.* **2004**, *104* (2), 939–986.
(44) Krebs, C.; Bollinger, J. M. Non-Heme Fe (IV)– Oxo Intermediates. *Acc. Chem. Res.* **2007**, *40* (7), 484–492.
(45) Nam, W. Dioxygen Activation by Metalloenzymes and Models. *Acc. Chem. Res.* **2007**, *40* (7), 465.
(46) Que, L. The Road to Non-Heme Oxoferryls and Beyond. *Acc. Chem. Res.* **2007**, *40* (7), 493–500.
(47) Collman James, P.; Reed, C. A.; Collman, J. P.; Reed, C. A.; Coliman, J. P.; Reed, C. A. Syntheses of Ferrous-Porphyrin Complexes. Hypothetical Model for Deoxymyoglobin. *J. Am. Chem. Soc.* **1973**, *95* (6), 2048–2049.
(48) Fleischer, E. B.; Srivastava, T. S. Structure and Properties of μ-Oxobis(Tetraphenylporphineiron(III)). *J. Am. Chem. Soc.* **1969**, *91* (9), 2403–2405.
(49) Collman, J. P.; Gagne, R. T.; Reed, C. A.; Collman James, P.; Gagne, R. T.; Reed, C. A. Paramagnetic Dioxygen Complex of Iron(II) Derived from a Picket Fence Porphyrin. Further Models for Hemoproteins. *J. Am. Chem. Soc.* **1974**, *96* (8), 2629–2631.
(50) Collman, J. P.; Gagne, R. R.; Reed, C. A.; Robinson, W. T.; Rodley, G. A. Structure of an Iron(II) Dioxygen Complex; a Model for Oxygen Carrying Hemeproteins. *Proc. Natl. Acad. Science. U. S. A.* **1974**, *71* (4), 1326–1329.
(51) Wuenschell, G. E.; Tetreau, C.; Lavalette, D.; Reed, C. A. H-Bonded Oxyhemoglobin Models with Substituted Picket-Fence Porphyrins - the Model-Compound Equivalent

of Site-Directed Mutagenesis. *J. Am. Chem. Soc.* **1992**, *114* (9), 3346–3355.
(52) Helm, M. L.; Stewart, M. P.; Bullock, R. M.; DuBois, M. R.; DuBois, D. L. A Synthetic Nickel Electrocatalyst with a Turnover Frequency above 100,000 S^{-1} for H_2 Production. *Science.* **2011**, *333* (6044), 863–866.
(53) Wilson, A. D.; Newell, R. H.; McNevin, M. J.; Muckerman, J. T.; Rakowski DuBois, M.; DuBois, D. L. Hydrogen Oxidation and Production Using Nickel-Based Molecular Catalysts with Positioned Proton Relays. *J. Am. Chem. Soc.* **2006**, *128* (1), 358–366.
(54) Dahl, E. W.; Kiernicki, J. J.; Zeller, M.; Szymczak, N. K. Hydrogen Bonds Dictate O_2 Capture and Release within a Zinc Tripod. *J. Am. Chem. Soc.* **2018**, *140* (32), 10075–10079.
(55) Gordon, Z.; Drummond, M. J.; Matson, E. M.; Bogart, J. A.; Schelter, E. J.; Lord, R. L.; Fout, A. R. Tuning the Fe(II/III) Redox Potential in Nonheme Fe(II)-Hydroxo Complexes through Primary and Secondary Coordination Sphere Modifications. *Inorg. Chem.* **2017**, *56* (9), 4852–4863.
(56) Kanady, J. S.; Tsui, E. Y.; Day, M. W.; Agapie, T. A Synthetic Model of the Mn3Ca Subsite of the Oxygen-Evolving Complex in Photosystem II. *Science.* **2011**, *333* (6043), 733–736.
(57) Tsui, E. Y.; Kanady, J. S.; Agapie, T. Synthetic Cluster Models of Biological and Heterogeneous Manganese Catalysts for O_2 evolution. *Inorg. Chem.* **2013**, *52* (24), 13833–13848.
(58) Yiu, S.-M.; Man, W.-L.; Lau, T.-C. Efficient Catalytic Oxidation of Alkanes by Lewis Acid/[Os VI(N)Cl 4] −Using Peroxides as Terminal Oxidants. Evidence for a Metal-Based Active Intermediate. **2008**, *130* (32), 10821–10827.
(59) Fukuzumi, S.; Morimoto, Y.; Kotani, H.; Naumov, P.; Lee, Y.-M.; Nam, W. Crystal Structure of a Metal Ion-Bound Oxoiron(IV) Complex and Implications for Biological Electron Transfer. *Nat. Chem.* **2010**, *2* (9), 756–759.
(60) Baglia, R. A.; Dürr, M.; Ivanović-Burmazović, I.; Goldberg, D. P. Activation of a High-Valent Manganese–Oxo Complex by a Nonmetallic Lewis Acid. *Inorg. Chem.* **2014**, *53* (12), 5893–5895.
(61) Leeladee, P.; Baglia, R. A.; Prokop, K. A.; Latifi, R.; de Visser Sam, P.; Goldberg, D. P. Valence Tautomerism in a High-Valent Manganese–Oxo Porphyrinoid Complex Induced by a Lewis Acid. *J. Am. Chem. Soc.* **2012**, *134* (25), 10397–10400.
(62) Blake, M. P.; Kaltsoyannis, N.; Mountford, P. Heterobimetallic Complexes Containing Ca–Fe or Yb–Fe Bonds: Synthesis and Molecular and Electronic Structures of [M{CpFe(CO) 2 } 2 (THF) 3] 2 (M = Ca or Yb). *J. Am. Chem. Soc.* **2011**, *133* (39), 15358–15361.
(63) Sarish, S.; Nembenna, S.; Nagendran, S.; Roesky, H. W.; Pal, A.; Herbst-Irmer, R.; Ringe, A.; Magull, J. A Reactivity Change of a Strontium Monohydroxide by Umpolung to an Acid. *Inorg. Chem.* **2008**, *47* (13), 5971–5977.
(64) Nayak, S.; Nayek, H. P.; Dehnen, S.; Powell, A. K.; Reedijk, J. Trigonal Propeller-Shaped [MnIII3MIINa] Complexes (M = Mn, Ca): Structural and Functional Models for the Dioxygen Evolving Centre of PSII. *Dalt. Trans.* **2011**, *40* (12), 2699.
(65) Hewitt, I. J.; Tang, J.-K.; Madhu, N. T.; Cl rac, R.; Buth, G.; Anson, C. E.; Powell, A. K. A Series of New Structural Models for the OEC in Photosystem II. *Chem. Commun.* **2006**, 25, 2650.
(66) Mishra, A.; Wernsdorfer, W.; Abboud, K. A.; Christou, G. The First High Oxidation

State Manganese Calcium Cluster: Relevance to the Water Oxidizing Complex of Photosynthesis. *Chem. Commun.* **2005**, 1, 54.
(67) Lacy, D. C.; Park, Y. J.; Ziller, J. W.; Yano, J.; Borovik, A. S. Assembly and Properties of Heterobimetallic Co(II/III)/Ca(II) Complexes with Aquo and Hydroxo Ligands. *J. Am. Chem. Soc.* **2012**, *134* (42), 17526–17535.
(68) Park, Y. J.; Ziller, J. W.; Borovik, A. S. The Effects of Redox-Inactive Metal Ions on the Activation of Dioxygen: Isolation and Characterization of a Heterobimetallic Complex Containing a MnIII–(μ-OH)–CaII Core. *J. Am. Chem. Soc.* **2011**, *133* (24), 9258–9261.
(69) Park, Y. J.; Cook, S. A.; Sickerman, N. S.; Sano, Y.; Ziller, J. W.; Borovik, A. S. Heterobimetallic Complexes with M^{III}-(μ-OH)-M^{II} Cores (M^{III} = Fe, Mn, Ga; M^{II} = Ca, Sr, and Ba): Structural, Kinetic, and Redox Properties. *Chem. Science.* **2013**, *4* (2), 717–726.
(70) Delgado, M.; Ziegler, J. M.; Seda, T.; Zakharov, L. N.; Gilbertson, J. D. Pyridinediimine Iron Complexes with Pendant Redox-Inactive Metals Located in the Secondary Coordination Sphere. *Inorg. Chem.* **2016**, *55* (2), 555–557.
(71) Chantarojsiri, T.; Reath, A. H.; Yang, J. Cationic Charges Lead to Inverse Free Energy Relationship for N-N Bond Formation by Mn(VI) Nitrides. *Angew. Chemie Int. Ed.* **2018**, 1–7.
(72) Shook, R. L.; Borovik, A. S. The Effects of Hydrogen Bonds on Metal-Mediated O_2 Activation and Related Processes. *Chem. Commun.* **2008**, 46, 6095.
(73) Cook, S. A.; Borovik, A. S. Molecular Designs for Controlling the Local Environments around Metal Ions. *Acc. Chem. Res.* **2015**, *48* (8), 2407–2414.
(74) MacBeth, C. E.; Golombek, A. P.; Young Jr., V. G.; Yang, C.; Kuczera, K.; Hendrich, M. P.; Borovik, A. S. O_2 Activation by Nonheme Iron Complexes: A Monomeric Fe(III)-Oxo Complex Derived from O_2. *Science.* **2000**, *289* (5481), 938–941.
(75) Gupta, R.; Taguchi, T.; Lassalle-Kaiser, B.; Bominaar, E. L.; Yano, J.; Hendrich, M. P.; Borovik, A. S. High-Spin Mn–Oxo Complexes and Their Relevance to the Oxygen-Evolving Complex within Photosystem II. *Proc. Natl. Acad. Science.* **2015**, 201422800.
(76) Hill, E. A.; Weitz, A. C.; Onderko, E.; Romero-Rivera, A.; Guo, Y.; Swart, M.; Bominaar, E. L.; Green, M. T.; Hendrich, M. P.; Lacy, D. C.; et al. Reactivity of an Fe IV -Oxo Complex with Protons and Oxidants. *J. Am. Chem. Soc.* **2016**, *138* (40), 13143–13146.
(77) Park, Y. J.; Cook, S. A.; Sickerman, N. S.; Sano, Y.; Ziller, J. W.; Borovik, A. S. Heterobimetallic Complexes with M(III)-(μ-OH)-M(II) Cores (M(III) = Fe, Mn, Ga; M(II) = Ca, Sr, and Ba): Structural, Kinetic, and Redox Properties. *Chem. Science.* **2013**, *4* (2), 717–726.
(78) Ray, M.; Hammes, B. S.; Yap, G. P. A.; Rheingold, A. L.; Borovik, A. S. Structure and Physical Properties of Trigonal Monopyramidal Iron(II), Cobalt(II), Nickel(II), and Zinc(II) Complexes. *Inorg. Chem.* **1998**, *37* (7), 1527–1532.
(79) Taguchi, T.; Gupta, R.; Lassalle-Kaiser, B.; Boyce, D. W.; Yachandra, V. K.; Tolman, W. B.; Yano, J.; Hendrich, M. P.; Borovik, A. S. Preparation and Properties of a Monomeric High-Spin Mn(V)-Oxo Complex. *J. Am. Chem. Soc.* **2012**, *134* (4), 1996–1999.
(80) Taguchi, T.; Stone, K. L.; Gupta, R.; Kaiser-Lassalle, B.; Yano, J.; Hendrich, M. P.; Borovik, A. S. Preparation and Properties of an MnIV–Hydroxide Complex: Proton and Electron Transfer at a Mononuclear Manganese Site and Its Relationship to the Oxygen Evolving Complex within Photosystem II. *Chem. Science.* **2014**, *5* (8), 3064.
(81) Parsell, T. H.; Behan, R. K.; Green, M. T.; Hendrich, M. P.; Borovik, A. S. Preparation

and Properties of a Monomeric MnIV-Oxo Complex. *J. Am. Chem. Soc.* **2006**, *128* (27), 8728–8729.
(82) Gupta, R.; MacBeth, C. E.; Young, V. G. J.; Borovik, A. S. Isolation of Monomeric MnIII/II-OH and MnIII-O Complexes from Water: Evaluation of O-H Bond Dissociation Energies. *J. Am. Chem. Soc.* **2002**, *124* (7), 1136–1137.
(83) Lacy, D. C.; Park, Y. J.; Ziller, J. W.; Yano, J.; Borovik, A. S. Assembly and Properties of Heterobimetallic CoII/III/Ca II Complexes with Aquo and Hydroxo Ligands. *J. Am. Chem. Soc.* **2012**, *134* (42), 17526–17535.
(84) Sano, Y.; Weitz, A. C.; Ziller, J. W.; Hendrich, M. P.; Borovik, A. S. Unsymmetrical Bimetallic Complexes with MII–(μ-OH)–MIII Cores (MIIMIII = FeIIFeIII, MnIIFeIII, MnIIMnIII): Structural, Magnetic, and Redox Properties. *Inorg. Chem.* **2013**, *52* (18), 10229–10231.
(85) Sano, Y.; Lau, N.; Weitz, A. C.; Ziller, J. W.; Hendrich, M. P.; Borovik, A. S. Models for Unsymmetrical Active Sites in Metalloproteins: Structural, Redox, and Magnetic Properties of Bimetallic Complexes with MII-(μ-OH)-FeIIICores. *Inorg. Chem.* **2017**, *56* (22), 14118–14128.
(86) Sgro, M. J.; Stephan, D. W. Frustrated Lewis Pair Inspired Carbon Dioxide Reduction by a Ruthenium Tris(Aminophosphine) Complex. *Angew. Chemie. Int. Ed.* **2012**, *51* (45), 11343–11345.
(87) Lucas, R. L.; Zart, M. K.; Murkerjee, J.; Sorrell, T. N.; Powell, D. R.; Borovik, A. S. A Modular Approach toward Regulating the Secondary Coordination Sphere of Metal Ions: Differential Dioxygen Activation Assisted by Intramolecular Hydrogen Bonds. *J. Am. Chem. Soc.* **2006**, *128* (48), 15476–15489.
(88) Jones, J. R.; Ziller, J. W.; Borovik, A. S. Modulating the Primary and Secondary Coordination Spheres within a Series of CoII-OH Complexes. *Inorg. Chem.* **2017**, *56* (3), 1112–1120.
(89) Jitsukawa, K.; Oka, Y.; Yamaguchi, S.; Masuda, H. Preparation, Structure Characterization, and Oxidation Activity of Ruthenium Complexes with Tripodal Ligands Bearing Noncovalent Interaction Sites. *Inorg. Chem.* **2004**, *43* (25), 8119–8129.
(90) Shook, R. L.; Gunderson, W. A.; Greaves, J.; Ziller, J. W.; Hendrich, M. P.; Borovik, A. S. A Monomeric MnIII−Peroxo Complex Derived Directly from Dioxygen. *J. Am. Chem. Soc.* **2008**, *130* (28), 8888–8889.
(91) Shook, R. L.; Peterson, S. M.; Greaves, J.; Moore, C.; Rheingold, A. L.; Borovik, A. S. Catalytic Reduction of Dioxygen to Water with a Monomeric Manganese Complex at Room Temperature. *J. Am. Chem. Soc.* **2011**, *133* (15), 5810–5817.
(92) Gunanathan, C.; Milstein, D. Metal-Ligand Cooperation by Aromatization-Dearomatization: A New Paradigm in Bond Activation and "Green" Catalysis. *Acc. Chem. Res.* **2011**, *44* (8), 588–602.
(93) Trincado, M.; Grützmacher, H. Cooperating Ligands in Catalysis. *Coop. Catal. Des. Effic. Catal. Synth.* **2015**, *2*, 67–110.
(94) Adams, G. M.; Weller, A. S. POP-Type Ligands: Variable Coordination and Hemilabile Behaviour. *Coord. Chem. Rev.* **2018**, *355*, 150–172.
(95) Russell, S. K.; Milsmann, C.; Lobkovsky, E.; Weyhermüller, T.; Chirik, P. J. Synthesis, Electronic Structure, and Catalytic Activity of Reduced Bis(Aldimino)Pyridine Iron Compounds: Experimental Evidence for Ligand Participation. *Inorg. Chem.* **2011**, *50*

(7), 3159–3169.
(96) Hesp, K. D.; McDonald, R.; Ferguson, M. J.; Stradiotto, M. New Cationic and Zwitterionic Cp*M(K2-P,S) Complexes (M = Rh, Ir): Divergent Reactivity Pathways Arising from Alternative Modes of Ancillary Ligand Participation in Substrate Activation. *J. Am. Chem. Soc.* **2008**, *130* (48), 16394–16406.
(97) Khaskin, E.; Iron, M. A.; Shimon, L. J. W.; Zhang, J.; Milstein, D. N-H Activation of Amines and Ammonia by Ru via Metal-Ligand Cooperation. *J. Am. Chem. Soc.* **2010**, *132* (25), 8542–8543.
(98) MacBeth, C. E.; Hammes, B. S.; Young, V. G.; Borovik, A. S.; Young, V. G.; Borovik, A. S. Hydrogen-Bonding Cavities about Metal Ions: Synthesis, Structure, and Physical Properties for a Series of Monomeric M–OH Complexes Derived from Water. *Inorg. Chem.* **2001**, *40* (18), 4733–4741.
(99) Cook, S. A.; Hill, E. A.; Borovik, A. S. Lessons from Nature: A Bio-Inspired Approach to Molecular Design. *Biochemistry* **2015**, *54* (27), 4167–4180.
(100) Cook, S. A.; Borovik, A. S. Molecular Designs for Controlling the Local Environments around Metal Ions. *Acc. Chem. Res.* **2015**, *48* (8), 2407–2414.
(101) Hartle, M. D.; Delgado, M.; Gilbertson, J. D.; Pluth, M. D. Stabilization of a Zn(II) Hydrosulfido Complex Utilizing a Hydrogen-Bond Accepting Ligand. *Chem. Commun.* **2016**, *52* (49), 7680–7682.
(102) Dahl, E. W.; Dong, H. T.; Szymczak, N. K. Phenylamino Derivatives of Tris(2-Pyridylmethyl)Amine: Hydrogen-Bonded Peroxodicopper Complexes. *Chem. Commun.* **2018**, *54*, 892–895.
(103) Szymczak, N. K.; Oelkers, A. B.; Tyler, D. R. Detection of Hydrogen Bonding in Solution: A 2H Nuclear Magnetic Resonance Method Based on Rotational Motion of a Donor/Acceptor Complex. *Phys. Chem. Chem. Phys.* **2006**, *8* (34), 4002–4008.
(104) Kendall, A. J.; Zakharov, L. N.; Gilbertson, J. D. Synthesis and Stabilization of a Monomeric Iron(II) Hydroxo Complex via Intra Molecular Hydrogen Bonding in the Secondary Coordination Sphere. *Inorg. Chem.* **2010**, *49* (19), 8656–8658.
(105) Dauth, A.; Love, J. A. Synthesis and Reactivity of 2-Azametallacyclobutanes. *Dalt. Trans.* **2012**, *41* (26), 7782.
(106) Lacy, D. C.; Mukherjee, J.; Lucas, R. L.; Day, V. W.; Borovik, A. S. Metal Complexes with Varying Intramolecular Hydrogen Bonding Networks. *Polyhedron* **2013**, *52*, 261–267.
(107) Moore, C. M.; Szymczak, N. K. 6,6′-Dihydroxy Terpyridine: A Proton-Responsive Bifunctional Ligand and Its Application in Catalytic Transfer Hydrogenation of Ketones. *Chem. Commun.* **2013**, *49* (4), 400–402.
(108) Matson, E. M.; Bertke, J. A.; Fout, A. R. Isolation of Iron(II) Aqua and Hydroxyl Complexes Featuring a Tripodal H-Bond Donor and Acceptor Ligand. *Inorg. Chem.* **2014**, *53* (9), 4450–4458.
(109) Matson, E. M.; Park, Y. J.; Fout, A. R. Facile Nitrite Reduction in a Non-Heme Iron System: Formation of an Iron(III)-Oxo. *J. Am. Chem. Soc.* **2014**, *136* (50), 17398–17401.
(110) Li, X.; Siegbahn, P. E. M. Alternative Mechanisms for O_2 Release and O–O Bond Formation in the Oxygen Evolving Complex of Photosystem II. *Phys. Chem. Chem. Phys.* **2015**, *17* (18), 12168–12174.
(111) Matson, E. M.; Bertke, J. A.; Fout, A. R. Isolation of Iron(II) Aqua and Hydroxyl Complexes Featuring a Tripodal H-Bond Donor and Acceptor Ligand. *Inorg. Chem.*

2014, *53* (9), 4450–4458.
(112) Park, Y. J.; Matson, E. M.; Nilges, M. J.; Fout, A. R. Exploring Mn-O Bonding in the Context of an Electronically Flexible Secondary Coordination Sphere: Synthesis of a Mn(III)-Oxo. *Chem. Commun..* **2015**, *51* (25), 5310–5313.
(113) Matson, E. M.; Park, Y. J.; Fout, A. R. Facile Nitrite Reduction in a Non-Heme Iron System: Formation of an Iron(III)-Oxo. *J. Am. Chem. Soc.* **2014**, *136* (50), 17398–17401.
(114) Ray, M.; Golombek, A. P.; Hendrich, M. P.; Young, V. G.; Borovik, A. S. Synthesis and Structure of a Trigonal Monopyramidal Fe(II) Complex and Its Paramagnetic Carbon Monoxide Derivative. *J. Am. Chem. Soc.* **1996**, *118* (25), 6084–6085.
(115) Hammes, B. S.; Ramos-Maldonado, D.; Yap, G. P. A.; Liable-Sands, L.; Rheingold, A. L.; Young, V. G.; Borovik, A. S. C3-Symmetric Chiral Amidate Complexes: Effects of Ligand Binding on Cavity Structure. *Inorg. Chem.* **1997**, *36* (15), 3210–3211.
(116) Hammes, B. S.; Young, Jr., V. G.; Borovik, A. S. Hydrogen-Bonding Cavities about Metal Ions: A Redox Pair of Coordinatively Unsaturated Paramagnetic Co-OH Complexes. *Angew. Chemie Int. Ed.* **1999**, *38* (5), 666–669.
(117) Shirin, Z.; Hammes, B. S.; Young, V. G.; Borovik, A. S. Hydrogen Bonding in Metal Oxo Complexes: Synthesis and Structure of a Monomeric Manganese(III)−Oxo Complex and Its Hydroxo Analogue. *J. Am. Chem. Soc.* **2000**, *122* (8), 1836–1837.
(118) Gupta, R.; Borovik, A. S. Monomeric Mn III/II and Fe III/II Complexes with Terminal Hydroxo and Oxo Ligands: Probing Reactivity via O–H Bond Dissociation Energies. *J. Am. Chem. Soc.* **2003**, *125* (43), 13234–13242.
(119) Taguchi, T.; Gupta, R.; Lassalle-Kaiser, B.; Boyce, D. W.; Yachandra, V. K.; Tolman, W. B.; Yano, J.; Hendrich, M. P.; Borovik, A. S. Preparation and Properties of a Monomeric High-Spin Mn V –Oxo Complex. *J. Am. Chem. Soc.* **2012**, *134* (4), 1996–1999.
(120) Taguchi, T.; Stone, K. L.; Gupta, R.; Kaiser-Lassalle, B.; Yano, J.; Hendrich, M. P.; Borovik, A. S. Preparation and Properties of an Mn^{IV} –Hydroxide Complex: Proton and Electron Transfer at a Mononuclear Manganese Site and Its Relationship to the Oxygen Evolving Complex within Photosystem II. *Chem. Science.* **2014**, *5* (8), 3064–3071.
(121) Lacy, D. C.; Park, Y. J.; Ziller, J. W.; Yano, J.; Borovik, A. S. Assembly and Properties of Heterobimetallic CoII/III/CaII complexes with Aquo and Hydroxo Ligands. *J. Am. Chem. Soc.* **2012**, *134* (42), 17526–17535.
(122) Sickerman, N. S.; Peterson, S. M.; Ziller, J. W.; Borovik, A. S. Synthesis, Structure and Reactivity of $Fe^{II/III}$ –NH_3 Complexes Bearing a Tripodal Sulfonamido Ligand. *Chem. Commun.* **2014**, *50* (19), 2515–2517.
(123) Gupta, R.; MacBeth, C. E.; Young, V. G.; Borovik, A. S. Isolation of Monomeric MnIII/II−OH and MnIII−O Complexes from Water: Evaluation of O−H Bond Dissociation Energies. *J. Am. Chem. Soc.* **2002**, *124* (7), 1136–1137.
(124) MacBeth, C. E.; Gupta, R.; Mitchell-Koch, K. R.; Young, V. G.; Lushington, G. H.; Thompson, W. H.; Hendrich, M. P.; Borovik, A. S. Utilization of Hydrogen Bonds To Stabilize M−O(H) Units: Synthesis and Properties of Monomeric Iron and Manganese Complexes with Terminal Oxo and Hydroxo Ligands. *J. Am. Chem. Soc.* **2004**, *126* (8), 2556–2567.
(125) Shirin, Z.; Young, V. G.; Borovik, A. S. Synthesis and Structure of a Mn III (OH) Complex Generated from Dioxygen Dioxygen Activation at Room Temperature by a

New Mn II Complex Having a Cavity Motif Yields a Monomeric Mn III Complex with a Terminally Bonded Hydroxo Ligand Whose Oxygen Atom Is . **1997**, *036* (1), 1967–1968.
(126) Gupta, R.; Borovik, A. S. Monomeric MnIII/II and FeIII/II Complexes with Terminal Hydroxo and Oxo Ligands: Probing Reactivity via O−H Bond Dissociation Energies. *J. Am. Chem. Soc.* **2003**, *125* (43), 13234–13242.
(127) Gupta, R.; Taguchi, T.; Borovik, A. S.; Hendrich, M. P. Characterization of Monomeric Mn(II/III/IV)-Hydroxo Complexes from X- and Q-Band Dual Mode Electron Paramagnetic Resonance (EPR) Spectroscopy. *Inorg. Chem.* **2013**, *52* (21), 12568–12575.
(128) Halbach, R. L.; Gygi, D.; Bloch, E. D.; Anderson, B. L.; Nocera, D. G. Structurally Characterized Terminal Manganese(Iv) Oxo Tris(Alkoxide) Complex. *Chem. Science.* **2018**, *9* (19), 4524–4528.
(129) Leto, D. F.; Jackson, T. A. Mn K-Edge X-Ray Absorption Studies of Oxo- and Hydroxo-Manganese(IV) Complexes: Experimental and Theoretical Insights into Pre-Edge Properties. *Inorg. Chem.* **2014**, *53* (12), 6179–6194.
(130) Leto, D. F.; Massie, A. A.; Colmer, H. E.; Jackson, T. A. X-Band Electron Paramagnetic Resonance Comparison of Mononuclear Mn IV -Oxo and Mn IV -Hydroxo Complexes and Quantum Chemical Investigation of Mn IV Zero-Field Splitting. *Inorg. Chem.* **2016**, *55* (7), 2309.
(131) Rice, D. B.; Massie, A. A.; Jackson, T. A. Manganese-Oxygen Intermediates in O-O Bond Activation and Hydrogen-Atom Transfer Reactions. *Acc. Chem. Res.* **2017**, *50* (11), 2706–2717.
(132) Wijeratne, G. B.; Corzine, B.; Day, V. W.; Jackson, T. A. Saturation Kinetics in Phenolic O-H Bond Oxidation by a Mononuclear Mn(III)-OH Complex Derived from Dioxygen. *Inorg. Chem.* **2014**, *53* (14), 7622–7634.
(133) Coggins, M. K.; Brines, L. M.; Kovacs, J. A. Synthesis and Structural Characterization of a Series of MnIIIOR Complexes, Including a Water-Soluble MnIIIOH That Promotes Aerobic Hydrogen-Atom Transfer. *Inorg. Chem.* **2013**, *52* (21), 12383–12393.
(134) Pal, S.; Armstrong, W. H. Products from Reactions of Manganese Oxo Complex $[Mn_2O_2(O_2CCH_3)(Tpen)]^{2+}$ in Acidic and Neutral Aqueous Media: $[Mn_2(\mu\text{-}O)_2(\mu\text{-}O_2CCH_3)(Tpen)]^{3+}$ and $[\{Mn_3(\mu.\text{-}O)4(OH)(Tpen)\}_2(\mu\text{-}Tpen)]^{6+}$. *Inorg. Chem.* **1992**, *31* (26), 5417–5423.
(135) Goldsmith, C. R.; Cole, A. P.; Stack, T. D. P. C-H Activation by a Mononuclear Manganese(III) Hydroxide Complex: Synthesis and Characterization of a Manganese-Lipoxygenase Mimic *J. Am. Chem. Soc.* **2005**, *127* (27), 9904–9912.
(136) SPROVIERO, E. M.; Gascon, J. A.; McEvoy, J. P.; BRUDVIG, G. W.; Batista, V. S. Computational Studies of the O_2-Evolving Complex of Photosystem II and Biomimetic Oxomanganese Complexes. *Coord. Chem. Rev.* **2008**, *252* (3–4), 395–415.
(137) Siegbahn, P. E. M. Mechanisms for Proton Release during Water Oxidation in the S2 to S3 and S3 to S4 Transitions in Photosystem II. *Phys. Chem. Chem. Phys.* **2012**, *14* (14), 4849.
(138) Siegbahn, P. E. M. A Structure-Consistent Mechanism for Dioxygen Formation in Photosystem II. *Chem. A Eur. J.* **2008**, *14* (27), 8290–8302.
(139) Rapatskiy, L.; Cox, N.; Savitsky, A.; Ames, W. M.; Sander, J.; Nowaczyk, M. M.; Rögner,

M.; Boussac, A.; Neese, F.; Messinger, J.; et al. Detection of the Water-Binding Sites of the Oxygen-Evolving Complex of Photosystem II Using W-Band17O Electron-Electron Double Resonance-Detected NMR Spectroscopy. *J. Am. Chem. Soc.* **2012**, *134* (40), 16619–16634.
(140) Meyer, T. J.; Huynh, M. H. V.; Thorp, H. H. The Possible Role of Proton-Coupled Electron Transfer (PCET) in Water Oxidation by Photosystem II. *Angew. Chemie. Int. Ed.* **2007**, *46* (28), 5284–5304.
(141) Suga, M.; Akita, F.; Hirata, K.; Ueno, G.; Murakami, H.; Nakajima, Y.; Shimizu, T.; Yamashita, K.; Yamamoto, M.; Ago, H.; et al. Native Structure of Photosystem II at 1.95 Å Resolution Viewed by Femtosecond X-Ray Pulses. *Nature* **2014**, *517* (7532), 1–17.
(142) Pantazis, D. A.; Ames, W.; Cox, N.; Lubitz, W.; Neese, F. Two Interconvertible Structures That Explain the Spectroscopic Properties of the Oxygen-Evolving Complex of Photosystem II in the S2 State. *Angew. Chem., Int. Ed. Engl.* **2012**, *51* (39), 9935–9940.
(143) Siegbahn, P. E. M. Structures and Energetics for O 2Formation in Photosystem II. *Acc. Chem. Res.* **2009**, *42* (12), 1871–1880.
(144) Shoji, M.; Isobe, H.; Nakajima, T.; Shigeta, Y.; Suga, M.; Akita, F.; Shen, J.-R.; Yamaguchi, K. Large-Scale QM/MM Calculations of the $CaMn_4O_5$ Cluster in the S_3 State of the Oxygen Evolving Complex of Photosystem II. Comparison between Water-Inserted and No Water-Inserted Structures. *Faraday Discuss.* **2017**, *198*, 83–106.
(145) Connelly, N. G.; Geiger, W. E. Chemical Redox Agents for Organometallic Chemistry. *Chem. Rev.* **1996**, *96* (2), 877–910.
(146) Petasis, D. T.; Hendrich, M. P. Quantitative Interpretation of Multifrequency Multimode EPR Spectra of Metal Containing Proteins, Enzymes, and Biomimetic Complexes. *Methods Enzymol.* **2015**, *563*, 171–208.
(147) Revision A.02, Frisch, M. J.; Trucks, G. W.; Schlegel, H. B.; Scuseria, G. E.; Robb, M. A.; Cheeseman, J. R.; Scalmani, G.; Barone, V.; Mennucci, B.; Petersson, G. A.; Nakatsuji, H.; Caricato, M.; Li, X.; Hratchian, H. P.; Izmaylov, A. F.; Bloino, J.; Zheng, G.; Sonnenberg, J. L.; Hada, M.; Ehara, M.; Toyota, K.; Fukuda, R.; Hasegawa, J.; Ishida, M.; Nakajima, T.; Honda, Y.; Kitao, O.; Nakai, H.; Vreven, T; Montgomery, J. A., Jr.; Peralta, J. E.; Ogliaro, F.; Bearpark, M.; Heyd, J. J.; Brothers, E.; Kudin, K. N.; Staroverov, V. N.; Kobayashi, R.; Normand, J.; Raghavachari, K.; Rendell, A.; Burant, J. C.; Iyengar, S. S.; Tomasi, J.; Cossi, M.; Rega, N.; Millam, J. M.; Klene, M.; Knox, J. E.; Cross, J. B.; Bakken, V.; Adamo, C.; Jaramillo, J.; Gomperts, R.; Stratmann, R. E.; Yazyev, O.; Austin, A. J.; Cammi, R; Pomelli, C.; Ochterski, J. W.; Martin, R. L.; Morokuma, K.; Zakrzewski, V. G.; Voth, G. A.; Salvador, P.; Dannenberg, J. J.; Dapprich, S.; Daniels, A. D.; Farkas, O.; Foresman, J. B.; Ortiz, J. V.; Cioslowski, J.; Fox, D. J. Gaussian, Inc., Wallingford CT, 2009.
(148) Bruker AXS Inc, APEX2 Version 2014.11-0. Madison, WI 2014.
(149) Bruker AXS Inc, SAINT Version 8.34a. Madison, WI 2013.
(150) Sheldrick, G. M. SADABS. Bruker AXS, Inc: Madison 2014.
(151) Rittle, J.; Younker, J. M.; Green, M. T. Cytochrome P450: The Active Oxidant and Its Spectrum. *Inorg. Chem.* **2010**, *49* (8), 3610–3617.
(152) Panay, A. J.; Lee, M.; Krebs, C.; Bollinger, J. M. J.; Fitzpatrick, P. F. Evidence for a High-Spin Fe(IV) Species in the Catalytic Cycle of a Bacterial Phenylalanine Hydroxylase. *Biochemistry* **2011**, *50* (11), 1928–1933.

(153) Galonić Fujimori, D.; Barr, E. W.; Matthews, M. L.; Koch, G. M.; Yonce, J. R.; Walsh, C. T.; Bollinger, J. M.; Krebs, C.; Riggs-Gelasco, P. J. Spectroscopic Evidence for a High-Spin Br-Fe(IV)-Oxo Intermediate in the α-Ketoglutarate-Dependent Halogenase CytC3 from Streptomyces. *J. Am. Chem. Soc.* **2007**, *129* (44), 13408–13409.
(154) Sinnecker, S.; Svensen, N.; Barr, E. W.; Ye, S.; Bollinger, J. M.; Neese, F.; Krebs, C. Spectroscopic and Computational Evaluation of the Structure of the High-Spin Fe(IV)-Oxo Intermediates in Taurine: α-Ketoglutarate Dioxygenase from Escherichia Coli and Its His99Ala Ligand Variant. *J. Am. Chem. Soc.* **2007**, *129* (19), 6168–6179.
(155) Eser, B. E.; Barr, E. W.; Frantom, P. A.; Saleh, L.; Bollinger, J. M.; Krebs, C.; Fitzpatrick, P. F. Direct Spectroscopic Evidence for a High-Spin Fe(IV) Intermediate in Tyrosine Hydroxylase. *J. Am. Chem. Soc.* **2007**, *129* (37), 11334–11335.
(156) Krebs, C.; Galonić Fujimori, D.; Walsh, C. T.; Bollinger, J. M. Non-Heme Fe(IV)–Oxo Intermediates. *Acc. Chem. Res.* **2007**, *40* (7), 484–492.
(157) Krebs, C.; Price, J. C.; Baldwin, J.; Saleh, L.; Green, M. T.; Bollinger, J. M. J. Rapid Freeze-Quench 57Fe Moessbauer Spectroscopy: Monitoring Changes of an Iron-Containing Active Site during a Biochemical Reaction. *Inorg. Chem.* **2005**, *44* (4), 742–757.
(158) Proshlyakov, D. A.; Henshaw, T. F.; Monterosso, G. R.; Ryle, M. J.; Hausinger, R. P. Direct Detection of Oxygen Intermediates in the Non-Heme Fe Enzyme Taurine/α-Ketoglutarate Dioxygenase. *J. Am. Chem. Soc.* **2004**, *126* (4), 1022–1023.
(159) Hausinger, R. P. Fe(II)/α-Ketoglutarate-Dependent Hydroxylases and Related Enzymes. *Crit. Rev. Biochem. Mol. Biol.* **2004**, *39* (1), 21–68.
(160) Wang, Y.; Li, J.; Liu, A. Oxygen Activation by Mononuclear Nonheme Iron Dioxygenases Involved in the Degradation of Aromatics. *J. Biol. Inorg. Chem.* **2017**, *22* (2–3), 395–405.
(161) Barry, S. M.; Challis, G. L. Mechanism and Catalytic Diversity of Rieske Non-Heme Iron-Dependent Oxygenases. *ACS Catal.* **2013**, *3* (10), 2362–2370.
(162) Hohenberger, J.; Ray, K.; Meyer, K. The Biology and Chemistry of High-Valent Iron-Oxo and Iron-Nitrido Complexes. *Nat. Commun.* **2012**, *3*, 720.
(163) Cho, K.; Leeladee, P.; McGown, A. J.; DeBeer, S.; Goldberg, D. P. A High-Valent Iron–Oxo Corrolazine Activates C–H Bonds via Hydrogen-Atom Transfer. *J. Am. Chem. Soc.* **2012**, *134* (17), 7392–7399.
(164) Meyer, S.; Klawitter, I.; Demeshko, S.; Bill, E.; Meyer, F. A Tetracarbene-Oxoiron(IV) Complex. *Angew. Chem., Int. Ed. Engl.* **2013**, *52* (3), 901–905.
(165) Sahu, S.; Quesne, M. G.; Davies, C. G.; Dürr, M.; Ivanović-Burmazović, I.; Siegler, M. A.; Jameson, G. N. L.; de Visser Sam, P.; Goldberg, D. P. Direct Observation of a Nonheme Iron(IV)–Oxo Complex That Mediates Aromatic C–F Hydroxylation. *J. Am. Chem. Soc.* **2014**, *136* (39), 13542–13545.
(166) Mitra, M.; Nimir, H.; Demeshko, S.; Bhat, S. S.; Malinkin, S. O.; Haukka, M.; Lloret-Fillol, J.; Lisensky, G. C.; Meyer, F.; Shteinman, A. A.; et al. Nonheme Fe(IV) Oxo Complexes of Two New Pentadentate Ligands and Their Hydrogen-Atom and Oxygen-Atom Transfer Reactions. *Inorg. Chem.* **2015**, *54* (15), 7152–7164.
(167) Mitra, M.; Nimir, H.; Demeshko, S.; Bhat, S. S.; Malinkin, S. O.; Haukka, M.; Lloret-Fillol, J.; Lisensky, G. C.; Meyer, F.; Shteinman, A. A.; et al. Nonheme Fe(IV) Oxo Complexes of Two New Pentadentate Ligands and Their Hydrogen-Atom and Oxygen-Atom Transfer Reactions. *Inorg. Chem.* **2015**, *54* (15), 7152–7164.
(168) Du, J.; Zhang, J.; Zhu, J.; Xia, C.; Sun, W. Synthesis, Characterization, and Reactivity of a

Chiral Fe(IV)-Oxo Complex Bearing an l-Proline-Derived Aminopyridine Ligand. *New J. Chem.* **2018**, *42* (11), 8315–8319.
(169) Ghosh, A.; Tiago de Oliveira, F.; Yano, T.; Nishioka, T.; Beach, E. S.; Kinoshita, I.; Muenck, E.; Ryabov, A. D.; Horwitz, C. P.; Collins, T. J. Catalytically Active Micro - Oxodiiron(IV) Oxidants from Iron(III) and Dioxygen. *J. Am. Chem. Soc.* **2005**, *127* (8), 2505–2513.
(170) Rohde, J.-U.; Que, L. J. Axial Coordination of Carboxylate Activates the Non-Heme FeIV=O Unit. *Angew. Chem., Int. Ed. Engl.* **2005**, *44* (15), 2255–2258.
(171) Nam, W. High-Valent Iron(IV)–Oxo Complexes of Heme and Non-Heme Ligands in Oxygenation Reactions. *Acc. Chem. Res.* **2007**, *40* (7), 522–531.
(172) Wang, D.; Ray, K.; Collins, M. J.; Farquhar, E. R.; Frisch Jonathan, R.; Gomez, L.; Jackson, T. A.; Kerscher, M.; Waleska, A.; Comba, P.; et al. Nonheme Oxoiron(IV) Complexes of Pentadentate N5 Ligands: Spectroscopy, Electrochemistry, and Oxidative Reactivity. *Chem. Science.* **2012**, *4* (1), 282–291.
(173) Usharani, D.; Lacy, D. C.; Borovik, A. S.; Shaik, S. Dichotomous Hydrogen Atom Transfer vs Proton-Coupled Electron Transfer During Activation of X–H Bonds (X = C, N, O) by Nonheme Iron–Oxo Complexes of Variable Basicity. *J. Am. Chem. Soc.* **2013**, *135* (45), 17090–17104.
(174) Prakash, J.; Rohde, G. T.; Meier, K. K.; Jasniewski, A. J.; Van Heuvelen, K. M.; Münck, E.; Que, L. Spectroscopic Identification of an FeIII Center, Not FeIV, in the Crystalline Sc-O-Fe Adduct Derived from [FeIV(O)(TMC)]2+. *J. Am. Chem. Soc.* **2015**, *137* (10), 3478–3481.
(175) Lim, M. H.; Rohde, J.-U.; Stubna, A.; Bukowski, M. R.; Costas, M.; Ho, R. Y. N.; Munck, E.; Nam, W.; Que, L. J. An FeIV=O Complex of a Tetradentate Tripodal Nonheme Ligand. *Proc. Natl. Acad. Science.* **2003**, *100* (7), 3665–3670.
(176) Pestovsky, O.; Stoian, S.; Bominaar, E. L.; Shan, X.; Munck, E.; Que, L. J.; Bakac, A. Aqueous FeIV=O: Spectroscopic Identification and Oxo-Group Exchange. *Angew. Chem., Int. Ed. Engl.* **2005**, *44* (42), 6871–6874.
(177) Chanda, A.; Shan, X.; Chakrabarti, M.; Ellis, W. C.; Popescu, D. L.; de Oliveira, F. T.; Wang, D.; Lawrence Que, J.; Collins, T. J.; Munck, E.; et al. (TAML)FeIV═O Complex in Aqueous Solution: Synthesis and Spectroscopic and Computational Characterization. *Inorg. Chem.* **2008**, *47* (9), 3669–3678.
(178) Jackson, T. A.; Rohde, J.-U.; Seo, M. S.; Sastri, C. V; DeHont, R.; Stubna, A.; Ohta, T.; Kitagawa, T.; Munck, E.; Nam, W.; et al. Axial Ligand Effects on the Geometric and Electronic Structures of Nonheme Oxoiron(IV) Complexes. *J. Am. Chem. Soc.* **2008**, *130* (37), 12394–12407.
(179) England, J.; Guo, Y.; Van, H. K. M.; Cranswick, M. A.; Rohde, G. T.; Bominaar, E. L.; Munck, E.; Que, L. J. A More Reactive Trigonal-Bipyramidal High-Spin Oxoiron(IV) Complex with a Cis-Labile Site. *J. Am. Chem. Soc.* **2011**, *133* (31), 11880–11883.
(180) Gupta, R.; Lacy, D. C.; Bominaar, E. L.; Borovik, A. S.; Hendrich, M. P. Electron Paramagnetic Resonance and Mössbauer Spectroscopy and Density Functional Theory Analysis of a High-Spin FeIV–Oxo Complex. *J. Am. Chem. Soc.* **2012**, *134* (23), 9775–9784.
(181) Bigi, J. P.; Harman, W. H.; Lassalle-Kaiser, B.; Robles, D. M.; Stich, T. A.; Yano, J.; Britt, R. D.; Chang, C. J. A High-Spin Iron(IV)–Oxo Complex Supported by a Trigonal Nonheme Pyrrolide Platform. *J. Am. Chem. Soc.* **2012**, *134* (3), 1536–1542.

(182) Zaragoza, J. P. T.; Yosca, T. H.; Siegler, M. A.; Moënne-Loccoz, P.; Green, M. T.; Goldberg, D. P. Direct Observation of Oxygen Rebound with an Iron-Hydroxide Complex. *J. Am. Chem. Soc.* **2017**, *139* (39), 13640–13643.
(183) Oswald, V. F.; Weitz, A. C.; Biswas, S.; Ziller, J. W.; Hendrich, M. P.; Borovik, A. S. Manganese–Hydroxido Complexes Supported by a Urea/Phosphinic Amide Tripodal Ligand. **2018**, *20*, 54.
(184) Lacy, D. C.; Gupta, R.; Stone, K. L.; Greaves, J.; Ziller, J. W.; Hendrich, M. P.; Borovik, A. S. Formation, Structure, and EPR Detection of a High Spin Fe IV —Oxo Species Derived from Either an FeIII—Oxo or FeIII—OH Complex. *J. Am. Chem. Soc.* **2010**, *132* (35), 12188–12190.
(185) Zhdankin, V. V; Litvinov, D. N.; Koposov, A. Y.; Luu, T.; Ferguson, M. J.; McDonald, R.; Tykwinski, R. R. Preparation and Structure of 2-Iodoxybenzoate Esters: Soluble and Stable Periodinane Oxidizing Reagents. *Chem. Commum.* **2004**, *263* (1), 106–107.
(186) Hong, S.; Lee, Y. M.; Sankaralingam, M.; Vardhaman, A. K.; Park, Y. J.; Cho, K. Bin; Ogura, T.; Sarangi, R.; Fukuzumi, S.; Nam, W. A Manganese(V)-Oxo Complex: Synthesis by Dioxygen Activation and Enhancement of Its Oxidizing Power by Binding Scandium Ion. *J. Am. Chem. Soc.* **2016**, *138* (27), 8523–8532.
(187) Codolà, Z.; Gómez, L.; Kleespies, S. T.; Que, L.; Costas, M.; Lloret-Fillol, J. Evidence for an Oxygen Evolving Iron-Oxo-Cerium Intermediate in Iron-Catalysed Water Oxidation. *Nat. Commun.* **2015**, *6*.
(188) Leeladee, P.; Baglia, R. A.; Prokop, K. A.; Latifi, R.; De Visser, S. P.; Goldberg, D. P. Valence Tautomerism in a High-Valent Manganese-Oxo Porphyrinoid Complex Induced by a Lewis Acid. *J. Am. Chem. Soc.* **2012**, *134* (25), 10397–10400.
(189) Baglia, R. A.; Dürr, M.; Ivanović-Burmazović, I.; Goldberg, D. P. Activation of a High-Valent Manganese-Oxo Complex by a Nonmetallic Lewis Acid. *Inorg. Chem.* **2014**, *53* (12), 5893–5895.
(190) Zaragoza, J. P. T.; Baglia, R. A.; Siegler, M. A.; Goldberg, D. P. Strong Inhibition of O-Atom Transfer Reactivity for MnIV(O)(π-Radical-Cation)(Lewis Acid) versus MnV(O) Porphyrinoid Complexes. *J. Am. Chem. Soc.* **2015**, *137* (20), 6531–6540.
(191) Baglia, R. A.; Krest, C. M.; Yang, T.; Leeladee, P.; Goldberg, D. P. High-Valent Manganese-Oxo Valence Tautomers and the Influence of Lewis/Brönsted Acids on C-H Bond Cleavage. *Inorg. Chem.* **2016**, *55* (20), 10800–10809.
(192) Swart, M. A Change in the Oxidation State of Iron: Scandium Is Not Innocent. *Chem. Commun.* **2013**, *49* (59), 6650.
(193) Tsui, E. Y.; Agapie, T. Reduction Potentials of Heterometallic Manganese-Oxido Cubane Complexes Modulated by Redox-Inactive Metals. *Proc. Natl. Acad. Science. U. S. A.* **2013**, *110* (25), 10084–10088.
(194) Tsui, E. Y.; Tran, R.; Yano, J.; Agapie, T. Redox-Inactive Metals Modulate the Reduction Potential in Heterometallic Manganese–Oxido Clusters. *Nat. Chem.* **2013**, *5* (4), 293–299.
(195) Herbert, D. E.; Lionetti, D.; Rittle, J.; Agapie, T. Heterometallic Triiron-Oxo/Hydroxo Clusters: Effect of Redox-Inactive Metals. *J. Am. Chem. Soc.* **2013**, *135* (51), 19075–19078.
(196) Park, Y. J.; Cook, S. A.; Sickerman, N. S.; Sano, Y.; Ziller, J. W.; Borovik, A. S. Heterobimetallic Complexes with MIII-(OH)-MII Cores (M III = Fe, Mn, Ga; M II = Ca, Sr, and Ba): Structural, Kinetic, and Redox Properties. *Chem. Science.* **2013**, *4* (2),

717–726.
(197) Dalzell Perrin, D. *Dissociation Constant of Inorgani Acids and Bases in Aqueous Solution*; Oxford Oxfordshire: New York, NY, 1982.
(198) Weitz, A.; Hill, E. A.; Oswald, V. F.; Bominaar, E. L.; Borovik, A. S.; Hendrich, M. P.; Guo, Y. Probing Hydrogen Bonding Interactions to Iron-Oxido/Hydroxido Units via 57Fe Nuclear Resonance Vibrational Spectroscopy. *Angew. Chemie Int. Ed.* **2018**.
(199) England, J.; Martinho, M.; Farquhar, E. R.; Frisch, J. R.; Bominaar, E. L.; Münck, E.; Que, L. A Synthetic High-Spin Oxoiron(IV) Complex: Generation, Spectro-Scopic Characterization, and Reactivity. *Angew. Chemie. Int. Ed.* **2009**, *48* (20), 3622–3626.
(200) England, J.; Farquhar, E. R.; Guo, Y.; Cranswick, M. A.; Ray, K.; Munck, E.; Lawrence Que, J. Characterization of a Tricationic Trigonal Bipyramidal Iron(IV) Cyanide Complex, with a Very High Reduction Potential, and Its Iron(II) and Iron(III) Congeners. *Inorg. Chem.* **2011**, *50* (7), 2885–2896.
(201) Rohde, J.-U.; Torelli, S.; Shan, X.; Lim, M. H.; Klinker, E. J.; Kaizer, J.; Chen, K.; Nam, W.; Que, L. J. Structural Insights into Nonheme Alkylperoxoiron(III) and Oxoiron(IV) Intermediates by X-Ray Absorption Spectroscopy. *J. Am. Chem. Soc.* **2004**, *126* (51), 16750–16761.
(202) Martin-Diaconescu, V.; Gennari, M.; Gerey, B.; Tsui, E.; Kanady, J.; Tran, R.; Pécaut, J.; Maganas, D.; Krewald, V.; Gouré, E.; et al. Ca K-Edge XAS as a Probe of Calcium Centers in Complex Systems. *Inorg. Chem.* **2015**, *54* (4), 1283–1292.
(203) Chandrasekaran, P.; Stieber, S. C. E.; Collins, T. J.; Que, Jr., L.; Neese, F.; DeBeer, S. Prediction of High-Valent Iron K-Edge Absorption Spectra by Time-Dependent Density Functional Theory. *Dalt. Trans.* **2011**, *40* (42), 11070.
(204) Green, M. T. Application of Badger's Rule to Heme and Non-Heme Iron-Oxygen Bonds: An Examination of Ferryl Protonation States. *J. Am. Chem. Soc.* **2006**, *128* (6), 1902–1906.
(205) Zhdankin, V. V.; Koposov, A. Y.; Litvinov, D. N.; Ferguson, M. J.; McDonald, R.; Luu, T.; Tykwinski, R. R. Esters of 2-Iodoxybenzoic Acid: Hypervalent Iodine Oxidizing Reagents with a Pseudobenziodoxole Structure. *J. Org. Chem.* **2005**, *70* (16), 6484–6491.
(206) Sanchez, E. R.; Gessel, M. C.; Groy, T. L.; Caudle, M. T. Interaction of Biotin with Mg-O Bonds: Bifunctional Binding and Recognition of Biotin and Related Ligands by the $Mg(15\text{-Crown-}5)^{2+}$ Unit. *J. Am. Chem. Soc.* **2002**, *124* (9), 1933–1940.
(207) Kanamura, K.; Yonezawa, S.; Kawai, Y.; Takehara, Z.-I. J. No Title. *Electroanal. Chem. Interfacial Electrochem.* **1991**, *301*, 291–295.
(208) Sturhahn, W. J. *Phys. Condens. Matter* **2004**, *16*, S497–S530.
(209) Toellner, T. S. *Hyperfine Interact* **2000**, *125*, 3–28.
(210) Sturhahn, W. *Hyperfine Interact.* **2000**, *125*, 149–172.
(211) George, G. N. EXAFSPAK. 2000.
(212) Ankudinov, A. L.; Ravel, B.; Rehr, J. J.; Conradson, S. D. No Title. *Phys. Rev. B* **1998**, *58*, 7565–7567.
(213) Lau, N.; Ziller, J. W.; Borovik, A. S. Sulfonamido Tripods: Tuning Redox Potentials via Ligand Modifications. *Polyhedron* **2015**, *85*, 777–782.
(214) Shan, X.; Rohde, J.-U.; Koehntop, K. D.; Zhou, Y.; Bukowski, M. R.; Costas, M.; Fujisawa, K.; Que, L. J. X-Ray Absorption Spectroscopic Studies of High-Spin Nonheme (Alkylperoxo)Iron(III) Intermediates. *Inorg. Chem.* **2007**, *46* (20), 8410–8417.

(215) Cheng, M. J.; Goddard, W. A. The Critical Role of Phosphate in Vanadium Phosphate Oxide for the Catalytic Activation and Functionalization of N-Butane to Maleic Anhydride. *J. Am. Chem. Soc.* **2013**, *135* (12), 4600–4603.
(216) Chu, J.; Carroll, T. G.; Wu, G.; Telser, J.; Dobrovetsky, R.; Ménard, G. Probing Hydrogen Atom Transfer at a Phosphorus(V) Oxide Bond Using a "Bulky Hydrogen Atom" Surrogate: Analogies to PCET. *J. Am. Chem. Soc.* **2018**, V, jacs.8b09063.
(217) Sheldrick, G. M. SHELXTL. Bruker AXS, Inc: Madison 2014.
(218) Spek, A. L. PLATON SQUEEZE: A Tool for the Calculation of the Disordered Solvent Contribution to the Calculated Structure Factors. *Acta Crystallogr. Sect. C Struct. Chem.* **2015**, *71* (1), 9–18.
(219) Shirin, Z.; S. Borovik, A.; G. Young Jr., V. Synthesis and Structure of a MnIII(OH) Complex Generated from Dioxygen. *Chem. Commun.* **1997**, 20, 1967.
(220) Majoral, J. P. *New Aspects in Phosphorus Chemistry*, V.; Springer Science & Business Media: Netherland, 2005.
(221) Tolman, C. A. Electron Donor-Acceptor Properties of Phosphorus Ligands. Substituent Additivity. *J. Am. Chem. Soc.* **1970**, *92* (10), 2953–2956.
(222) Parsell, T. H.; Behan, R. K.; Green, M. T.; Hendrich, M. P.; Borovik, A. S. Preparation and Properties of a Monomeric Mn(IV)-Oxo Complex. *J. Am. Chem. Soc.* **2006**, *128* (27), 8728–8729.
(223) Fukuzumi, S.; Morimoto, Y.; Kotani, H.; Naumov, P.; Lee, Y. M.; Nam, W. Crystal Structure of a Metal Ion-Bound Oxoiron(IV) Complex and Implications for Biological Electron Transfer. *Nat. Chem.* **2010**, *2* (9), 756–759.
(224) Boduszek, B.; Shine, H. J. Preparation of Solid Thianthrene Cation Radical Tetrafluoroborate. *J. Org. Chem.* **1988**, *53* (21), 5142–5143.